Dissertation

submitted to the

Combined Faculties for Natural Sciences and for Mathematics

of the Ruperto-Carola University of Heidelberg, Germany

for the degree of

Doctor of Natural Sciences

presented by

Dipl.-Phys. Steffen Novotny

born in Schwetzingen

Oral examination: June 25th, 2008

Fragmentation of molecular ions in slow electron collisions

Kurzfassung

Fragmentation von Molekülionen in Kollisionen langsamer Elektronen

Die Fragmentation positiver Wasserstoff Molekülionen durch den Einfang langsamer Elektronen, die sogenannte Dissoziative Rekombination (DR), wurde in Speicherring-Experimenten am TSR, Heidelberg, durch gleichzeitige Überlagerung zweier unabhängiger Elektronenstrahlen und mit hochauflösenden Fragmentationsabbildungsdetektoren untersucht. Die Framentationskinematik konnte mit Hilfe kalter Elektronen bis in den Bereich einiger meV Kollisionsenergie bestimmt werden, wo ausgeprägte Rotations- und Vibrationsresonanzen im DR Wirkungsquerschnitt auftreten. Für thermisch angeregtes HD^+ wurden Fragmentationswinkel als auch die freiwerdende kinetisch Energie auf einem feinmaschigen Gitter zwischen ca. 10 und 80 meV präziser eingestellter Kollisionsenergie bestimmt. Die beobachtete Anisotropie, erstmals beschrieben durch Legendre-Polynome grösser zweiter Ordnung, als auch die Rotationsbeiträge variieren dabei vergleichbar mit dem rotations-gemittelten DR Ratenkoeffizienten. Rotations- und vibrationsaufgelöste DR Experimente an H_2^+ wurden durch eine neu entwickelte Ionenqelle ermöglicht. Sowohl der DR Ratenkoeffizient als auch die Fragmentationsdynamik bei ausgewählten Resonanzen niedriger Kollisionsenergie konnten selektiv in den untersten beiden Vibrations- und den ersten drei angeregten Rotationszuständen untersucht werden. Zustandsabhängige DR Raten und Winkelverteilungen werden vorgestellt.

Abstract

Fragmentation of molecular ions in slow electron collisions

The fragmentation of positively charged hydrogen molecular ions by the capture of slow electrons, the so called dissociative recombination (DR), has been investigated in storage ring experiments at the TSR, Heidelberg, where an unique twin-electron-beam arrangement was combined with high resolution fragment imaging detection. Provided with well directed cold electrons the fragmentation kinematics were measured down to meV collision energies where pronounced ro-vibrational Feshbach resonances appear in the DR cross section. For thermally excited HD^+ the fragmentation angle and the kinetic energy release were studied at variable precisely controlled electron collision energies on a dense energy grid from 10 to 80 meV. The anisotropy described for the first time by Legendre polynomials higher 2nd order and the extracted rotational state contributions were found to vary on a likewise narrow energy scale as the rotationally averaged DR rate coefficient. Ro-vibrationally resolved DR experiments were performed on H_2^+ produced in distinct internal excitations by a novel ion source. Both the low-energy DR rate as well as the fragmentation dynamics at selected resonances were measured individually in the lowest two vibrational and first three excited rotational states. State-specific DR rates and angular dependences are reported.

Contents

1

Introduction

Collisions of molecules are the starting point for chemical and physical changes of matter in a variety of environments ranging from low density plasmas in interstellar space to living tissue of a human body. They can be associated with a transfer of energy between the reactants, cause a rearrangement of the molecular geometry or simply give rise that the molecule falls apart thereafter. In fundamental processes the molecule interacts with a photon or an elementary particle, such as an electron or a proton, but the complexity of the collision is not limited and can comprise reactions with abundant molecular constituents as well. This rises large interest and opens up a wide range for molecular physics research. The largest effect on the environment and its subsequent development will result from a fragmentation of the molecule following the collision, that is breaking the chemical bonds. The basic phenomenon initiating the breakup of a molecule is the resonant creation of an excited, unstable state in the collision. The molecule, finding itself in this new state, will start separating and proceeds upon a potential energy surface from an initial bound system at short internuclear distances to fragments well separated on the macroscopic scale. The evolving fragments carry the information on the reaction pathway and hence their study provides direct access to the fundamental fragmentation mechanisms.

From the experimental side, the investigation of the kinetic energy distributed among the products yields a "rough" picture of the fragmentation process as the energy balance will allow to infer the final product states. Further insights, revealing the distinct reaction path, can be obtained by comprising in addition the study of directional properties. For instance, the dependence of the reaction cross section on the orientation of the molecule can be related to the electronic symmetry characterizing the participating potential energy surface. Consequently, the study of molecular fragmentation processes will require highest control on the reaction parameters and aims at a full energy and momentum resolved picture of the escaping fragments. Particularly sensitive experiments in this respect are

those utilizing the high energy resolution of photon induced interactions [1] or applying electrons to study the creation of charged fragments in resonant collisions with neutral molecules [2].

The present work focuses on the fragmentation dynamics in binary collisions of positively charged diatomic molecular ions with electrons. Caused by the capture of the electron, the molecular cation by resonant energy transfer forms an excited neutral compound state which is unstable against dissociation into neutral atomic fragments. The excess energy released in the destruction process is distributed over internal excitations of the fragments, as far as possible, and over the kinetic degrees of freedom of the final products. The initiated neutralization process, generally referred to as *dissociative recombination* (DR) [3] (Chapter 2.1.3), attracts strong interest in modeling low-density ionized media such as atmospheric layers [4] or astrophysical environments [5, 6], but presents also an important process in various laboratory plasmas [7].

In view of the importance of the DR process, both theoretical and experimental interest has continuously risen over the past decades addressing mainly the molecular fragmentation by electrons through rate measurements in event-by-event counting experiments. Recently, in particular the experimental studies have benefited greatly from the storage ring technique becoming available to the field of molecular physics [8]. Within this setup both electrons and molecular ions can be brought together at well defined kinematics down to small relative collision energies in the sub-eV range. Compared to the fast ion beam (reaching energies of up to a few MeV/nucleon) the kinetic energy released among the escaping fragments is small (in the range of eV) so that the trajectories of all neutral products are constraint to a narrow cone in forward direction. This greatly simplifies the detection setup which is required to efficiently collect the neutral recombination products. Taking advantage of these technical developments, experiments focusing on the DR-induced fragmentation dynamics are now becoming possible. They combine the storage ring setup with a fragment imaging detection system to perform measurements with unidirectional monochromatic electron impact under stable ion beam conditions. In the present experiments a multi-hit 2D and 3D imaging detector has been utilized to determine both the information on the kinetic energy release as well as the fragmentation direction from the simultaneous measurement of the relative fragment impact positions. The details on the fragment imaging technique are described in Chapter 3.

The hydrogen molecular ion H_2^+ and the deuterated relative HD^+ have found much attention in numerous experiments investigating the electron-ion interaction in merged beam setups at storage rings (e.g. [9, 10, 11, 12, 13]). Their simple structure favors the study also from the theoretical side [14, 15, 16] so that the molecular system has become a

benchmark system in DR research. At low electron collision energies the capture of the electron by an initial bound electronic state of the ion leads through resonant energy transfer to the formation of rotationally and vibrationally excited neutral Rydberg states. Their fragmentation by predissociation causes interference effects with the second, direct dissociation route, creating a rich resonant modulation in the DR cross section at low electron collision energies. For vibrationally cold HD^+ with only a few rotational levels populated these patterns have been observed in high resolution measurements of the DR rate coefficient [13, 17]. While the principal underlying mechanism is theoretically understood, the assignment of the observed patterns is still missing. This has motivated the experimental investigation of additional aspects of the DR process which become accessible through the fragmentation dynamics in slow electron collisions.

First, for vibrationally relaxed HD^+ ions the product kinematics were analyzed in the vicinity of low-energy DR resonances below about 100 meV. Both the kinetic energy distributed among the fragments as well as the fragmentation directions were obtained in these experiments. The sensitivity on the electron energy required highest energy resolution of well directed colliding electrons which was made possible by a newly introduced, unique twin-electron beam arrangement at the TSR storage ring. The results obtained on a dense measurement grid are presented in Chapter 4 [18, 19].

In a second experimental series the low energy range was revisited, now using H_2^+ ions in selected initial states. Applying the same experimental setup measurements on the DR rate coefficient and the fragmentation dynamics were now performed in combination with an ion source which allowed the production of H_2^+ ions in distinct vibrationally and rotationally excited states. The results of these experiments are discussed in Chapter 5. Finally, the thesis is concluded by a summary of the experimental findings and gives an outlook on remaining open questions and possible future studies.

2

Dynamics in molecular fragmentation

The molecular dynamics in fragmentation processes are often described in the picture of potential energy surfaces. This chapter will start with an overview of this general concept, before it will focus on the fragmentation reaction studied in this work, the *dissociative recombination* process.

Determined by the participating potential energy surfaces the emitted fragments reveal through their emission directions the properties of these states, which allows to uniquely select the dissociation pathway. In comparison to other molecular fragmentation processes, the study of angular dependences in dissociative recombination found less attention, both experimentally and theoretically. The hydrogen molecular cations, H_2^+ and HD^+, can serve as an ideal system to investigate detailed aspects of the dissociative recombination induced fragmentation dynamics at low electron collision energies, as will be discussed in the final section.

2.1 General concepts

2.1.1 Potential energy surfaces and molecular states

The structure and the dynamics involved in processes of molecular systems are commonly approached considering the large mass difference between the electrons and nuclei. This gives rise to the assumption that as a result of similar forces the nuclear motion is much slower so that electrons react instantaneously to their movement. Consequently the electronic motion can be treated separately from the nuclear motion which simplifies the problem of solving the Schrödinger equation characterized by the molecular system.

In this concept, known as the *Born-Oppenheimer (BO) approximation* [20], the electronic wave functions are determined for a potential with fixed positions of the nuclei, that

is the nuclear configurations enter the calculation only as a parameter. The resulting electronic eigenenergies define for each nuclear arrangement together with the mutual Coulomb interaction of the nuclei the total potential energy function acting on the nuclei. This potential energy function is also called *potential energy surface* (PES). It is included in the nuclear Schrödinger equation which is subsequently solved in order to describe the nuclear motion (see, e.g. [21]).

Hence, the nuclear dynamics are closely related to the PES. Due to the nuclear-nuclear electrostatic repulsion the PES goes to infinity the closer the nuclei approach each other. In contrast, at large internuclear separation the potential tends to an asymptotic value and the PES determines the fragmentation process as well as the evolving atomic and possible molecular species. At intermediate internuclear separations stable, bound molecular states exhibit a local minimum in the PES which corresponds to a configuration of an equilibrium nuclear arrangement. Thereby vibrations can cause an oscillatory motion of the nuclei around the equilibrium position.

The dimension of the coordinate space describing the nuclear configuration and thus the PES depends on the number of atoms involved in the molecular system. For instance, in case of diatomic molecules treated here, the system reduces to a description in one dimension and hence the potential energy surface is actually more accurately termed a potential energy curve which depends only on the internuclear distance.

Besides the energy dependence, the electronic states corresponding to the PES are characterized by molecular term symbols which reflect symmetry properties of the electronic wave function as well as the orbital angular momenta and spins of the electrons and their couplings [21, 22]. Thereby the symmetry properties are defined by operations, such as rotations or reflections, which leave the nuclear configuration unchanged. For example for a homonuclear[1] diatomic molecule the inversion in the center of charge presents a symmetry operation described by the parity of the electronic wave function.

For most calculations where the potential energy surfaces of electronic states are energetically well separated the BO approximation yields sufficient accuracy. However, in situations where two PES energetically approach each other at the same nuclear configuration, i.e. the energy eigenvalues of the electronic states become degenerate, couplings between the electronic and the nuclear motion start to play a role, which are not considered in the BO approximation. In fact, for states of the same symmetry this results in a breakdown of the BO approximation. At these nuclear configurations the degeneracy of the respective electronic states is lifted and *avoided crossings* will occur equivalent to

---

[1] *Homonuclear* is referred here to the nuclear charges, i.e. both atoms have the same charge but can be different isotopes, e.g. HD^+.

a nuclear motion not defined by the PES of a single electronic state only. On the other hand, electronic states of different symmetry can possess degenerate energy eigenvalues and hence the corresponding PES are allowed to cross each other.

2.1.2 Fragmentation processes of molecules

The fragmentation of molecules can be initiated by a variety of processes, mostly in collisions with electrons or atomic and molecular species but also by the absorption of photons. Commonly these reactions are associated with a change of the nuclear configuration from an at least temporarily bound molecular state to individual fragments exhibiting onto each other only a negligible force at sufficient internuclear separation.

For the description of these dynamical processes the picture of a system moving along a potential energy surface is particularly suited. In doing so, either only one PES is involved, that is the system stays in the same electronic eigenstate, but stabilizes into separate fragments at a large internuclear distance. On the other hand, the reaction may include a transition to a different PES and induce a change of the electronic state. Nevertheless, the products which evolve from fragmentation processes are determined by the PES and their asymptotic limit. Depending on the components of the fragmentation process they can consist of atomic or molecular species in different charge states and with possible internal excitations.

In Fig. 2.1 the initial bound state configuration of a diatomic molecule is found at the local minimum of a PES, corresponding for instance to the electronic ground state. Depending on the depth of the potential minimum, numerous vibrational and rotational states of the bound molecule give rise to a distinct level structure resulting from the eigenvalues of the nuclear Hamiltonian (only the vibrational states being indicated in the figure).

Starting from the vibrational ground state, which is indicated by the square of the nuclear wave function in Fig. 2.1, the molecule can in the current example leave the equilibrium arrangement only by gaining sufficient energy through a collision or the absorption of a photon. In the case that a transition to a vibrational continuum state (A), which is represented by the dashed line, becomes energetically possible, the molecule is no longer bound and the fragments can exhibit an arbitrary separation into the final channel α. Below the dissociation threshold, on the other hand, the absorbed energy dissipates into internal rotational and vibrational (ro-vibrational) excitations of the bound molecule which in turn has the possibility to subsequently cool down through radiative emission.

While in the above case the fragmentation involves only one PES, a breakup of the molecule can also be initiated by a change of the electronic state (B, C). The required
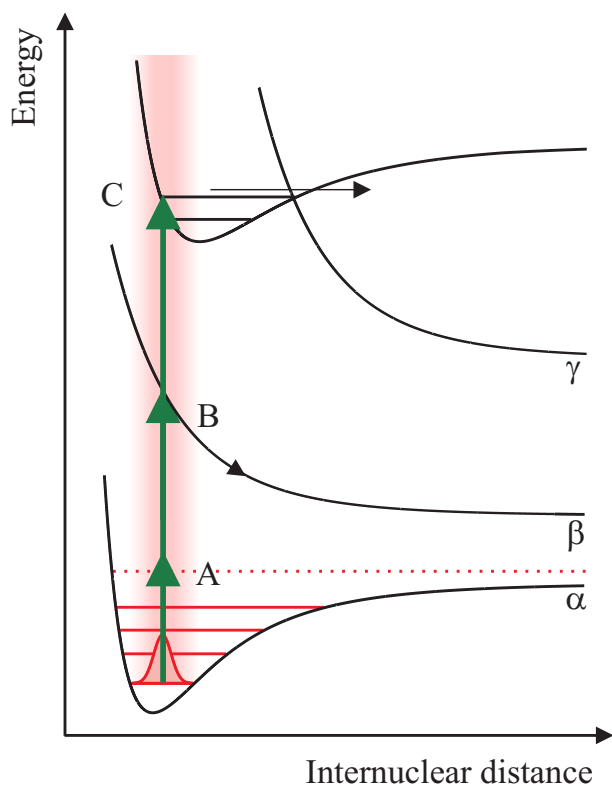
Figure 2.1: The schematic drawing of electronic PES as function of the internuclear distance illustrates possible fragmentation pathways for an initial bound diatomic molecule. Dissociation from a vibrational level (red lines) of the bound molecule can proceed through vibrational excitation into the continuum (A), electronic excitation (B) or via predissociation or tunneling out of an intermediate bound resonant state (C) leading to fragment channels α, β and γ, respectively. Thereby electronic transitions are limited to the Franck-Condon overlap (vertical shaded bar).

energy for the transition into a new electronic eigenstate has to be provided again by a collisional process or the absorption of a photon. With respect to the slow nuclear motion, this electronic transition occurs fast, that is the nuclei do not change their internuclear distance and hence are promoted vertically in the potential energy surface diagram which is also known as the *Franck-Condon principle*. In other words, the initial nuclear wave function $\Psi_v(R)$ is projected vertically into the vibrational eigenfunctions $\tilde{\Psi}_{v'}(R)$ of the new electronic state, a process which is particularly favored for a large overlap of the wave functions represented by the Franck-Condon factor (shaded bar in Fig. 2.1):

$$f(v, v') = \left| \int \Psi_v(R)\tilde{\Psi}_{v'}(R)dR \right|^2 . \tag{2.1}$$

Consequently, the movement of the nuclei is now governed by the new PES. For instance, nuclei which find themselves after electronic excitation on a repulsive PES (B) above the asymptotic energy level, proceed directly to large internuclear separations while dissociating into the corresponding fragments (channel β). Alternatively, the electronic transition can also first prepare the molecule in an intermediate quasi-bound state (C). From there the system can dissociate, non-radiatively, via predissociation or tunneling into the fragment channel γ. The two latter examples, as presented in Fig. 2.1, turn out to be particularly sensitive on the excitation energy which is added to the molecular system

during the transition, i.e. the fragmentation describes here a resonant process.

These processes are frequently realized in nature where they present an essential part in reaction chains. They can be induced by a variety of collisions, multiphoton absorption, high laser fields, short wave length photons (X-ray), etc. (see, e.g. [1, 2, 23]). Therefore they have initiated large interest in the study of their underlying mechanisms and to learn about their dynamics.

2.1.3 Fragmentation by dissociative recombination

Considering the specific case of electron induced fragmentation of a positively charged molecular ion, several dissociation processes can be initiated, differing in the charge state of the final products: *Dissociative excitation* describes the reaction where the electron escapes after the collision, leaving behind neutral and positively charged fragments of the molecule. In case the electron remains bound to the dissociating molecule the fragmentation process is called *dissociative recombination*. Moreover, *ion-pair formation* [24, 25] also becomes possible but which will not be followed further in this work.

Dissociative recombination (DR), producing only neutrals from a positively charged bound molecule after the capture of an electron, has first been suggested by Bates [3, 26] to explain an effective electron sink in the earth's ionosphere. Later the process was also recognized as a fast neutralization path for positively charged molecular ions in various plasmas, including for instance interstellar clouds [5, 6].

For diatomic molecular cations AB^+ provided in an initial vibrational v^+ and rotational J^+ state and electrons colliding with an energy E this fragmentation process can be summarized as follows

$$AB^+(v^+, J^+) + e^-(E) \rightarrow A(n, l) + B(n', l') + E_{KER}. \qquad (2.2)$$

where the final atomic products are distinguished by their principal and orbital angular momentum quantum numbers n (n') and l (l') and separate with kinetic energy E_{KER}. The explicit reaction path leading to the neutral atomic species is not specified in the above schematic equation. It depends sensitively both on the molecular system as well as the initial collision parameters. Describing the process in the picture of potential energy surfaces (see, e.g. Fig. 2.1), the capture of an electron promotes the molecular system onto a repulsive electronic state either directly or via an intermediate temporarily bound system, generally referred to as the *direct* and the *indirect* reaction path, respectively.

In the *direct DR process* the electron is captured into a doubly excited neutral state AB^{**} of the molecular system, that is the kinetic energy E of the incident electron is
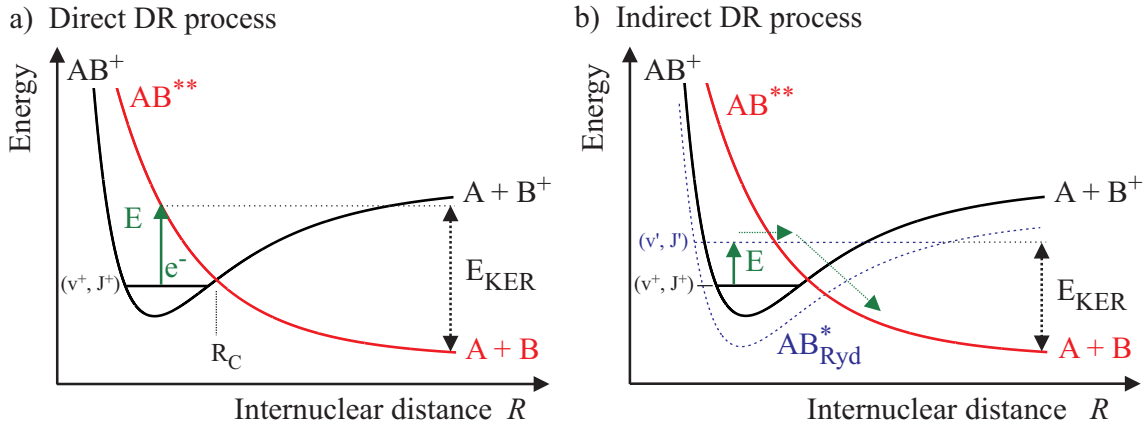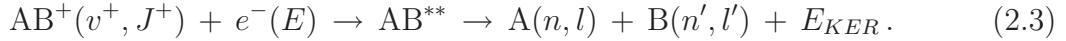
a) Direct DR process

b) Indirect DR process

Figure 2.2: Illustration of (a) the direct dissociative recombination (DR) and (b) the indirect DR process. The potential energy curve of a diatomic molecular cation AB^+ in the ro-vibrational state (v^+, J^+) is represented by the black line in each inlet. The electron with energy E is captured in (a) directly into the repulsive state AB^{**} (red line), whereas in (b) first the ro-vibrational level (v', J') of an excited Rydberg state (dashed blue line) is formed before dissociation of the molecular system continues upon AB^{**} (red line). The final atomic fragments A and B are emitted with a kinetic energy E_{KER}.

transformed through a rearrangement of the whole electronic cloud to an excitation of a second electron:

$$AB^+(v^+, J^+) + e^-(E) \rightarrow AB^{**} \rightarrow A(n, l) + B(n', l') + E_{KER}. \qquad (2.3)$$

Once the molecular system has reached the neutral, doubly excited state AB^{**}, the electron capture is stabilized by rapid dissociation into fragments. The direct DR process (Fig. 2.2(a)) is purely electronic and has a resonant character since it works most efficiently if the electron energy E matches the one of the transition from the ionic state AB^+ to the repulsive state AB^{**} at a given internuclear distance R within the Franck-Condon Region (also similar to process B in Fig. 2.1). Clearly, at low electron energies E a crossing of the bound ion and the repulsive neutral potential curves near the ro-vibrational level (v^+, J^+) will be required.

Formally, the transition in the direct DR pathway is described by the electronic coupling matrix element $V_{el}(R)$ in the total interaction matrix $V_{AB^+, AB^{**}} = \langle \Psi_{AB^{**}}(R) | V_{el}(R) | \Psi_{AB^+}(R) \rangle$ between the nuclear wave functions of the bound molecular ion Ψ_{AB^+} and the neutral dissociative state $\Psi_{AB^{**}}$. Therein $V_{el}(R)$ is given by
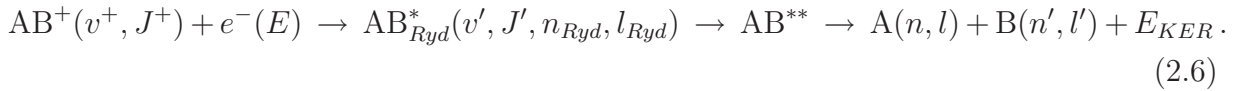
$$V_{el}(R) = \langle \Phi_d(q_e, R) | H_e(q_e, R) | \Phi_r(q_e, R) \rangle \qquad (2.4)$$

with the electronic Hamiltonian H_e and the electronic wave functions Φ_r and Φ_d of the reactants, including target ion and continuum electron, and the dissociative state AB** (q_e describe the electron coordinates). Assuming that the electronic coupling $V_{el}(R)$ varies only slowly in the overlap region, the direct DR cross section σ_{direct} for a single dissociative curve is governed by the Franck-Condon factor $|\langle\Psi_{AB^{**}}(R)|\Psi_{AB^+}(R)\rangle|^2$ (Eq.(2.1)) and is inverse proportional to the electron energy E [27]:

$$\sigma_{direct} \propto \frac{1}{E} \, |\langle\Psi_{AB^{**}}(R)|\Psi_{AB^+}(R)\rangle|^2 \cdot V_{el}^2 \cdot S \,. \qquad (2.5)$$

As long as the system has not reached a critical internuclear separation R_C, the excited compound state has sufficient energy to autoionize back to the reactants, i.e. the system emits an electron and returns to the bound ionic state. This possibility is included in the description of the direct DR cross section (Eq.(2.5)) by the survival factor S, the complement of the autoionization probability.

In contrast, in the *indirect DR process* [28] the kinetic energy of the incident electron is transformed into nuclear motion of the molecule. The capture of the electron proceeds through non-adiabatic couplings by the breakdown of the Born-Oppenheimer approximation and forms a rotationally and vibrationally (ro-vibrationally) excited molecular Rydberg state (Fig. 2.2(b)):

$$\text{AB}^+(v^+, J^+) + e^-(E) \rightarrow \text{AB}^*_{Ryd}(v', J', n_{Ryd}, l_{Ryd}) \rightarrow \text{AB}^{**} \rightarrow \text{A}(n,l) + \text{B}(n',l') + E_{KER} \,.$$

$$(2.6)$$

In these molecular Rydberg states the captured electron is orbiting far from the essentially undistorted ionic core in states labeled by the principal and orbital angular momentum quantum numbers n_{Ryd} and l_{Ryd}. Their vibrational v' and rotational J' excitation is defined by the ionic core.

This first step is followed by a second radiationless transition (predissociation) where the excited Rydberg state couples to the repulsive state AB** upon which the system then continues towards dissociation. Due to the discrete ro-vibrational energy levels of the neutral Rydberg states converging to the ionic limit, the indirect DR is regarded as a resonant process which is expected to sensitively depend on the ionic internal excitation at low electron collision energy. In addition, often the same doubly excited state is accessed by predissociation as by the direct DR mechanism, leading to interference between these dissociation routes of comparable strength. The hydrogen molecular cation presents an example which features at low electron energies both possible pathways, resulting in a rich structure of the DR cross section as will be discussed in Sec. 2.3.

In experiments various aspects of the DR process are typically addressed (e.g. [8]): The measurement of the DR rate coefficient as a function of the electron collision energy can be

related to the reaction cross section, whereas studies of the branching ratio into different final fragment states and species can yield information on the fragmentation pathways. In latter, the internal excitation of final atomic products is inferred using energy conservation from the measurement of the kinetic energy release E_{KER} by assuming a well known initial molecular ion state. However, in order to achieve a complete picture of the fragmentation dynamics which, for example, includes identifying the symmetry quantum numbers of the states AB^*_{Ryd} and AB^{**} participating in the fragmentation process, information on a possible dependence on the angle between the molecular orientation and the captured electron will be needed.

2.2 Fragment angular dependences

The dissociation properties of the evolving fragments carry information on the participating electronic states and their couplings in the process and thus on the molecular dynamics at short internuclear distances, which are governed by the potential energy surfaces. Numerous repulsive states of different electronic symmetry are often energetically accessible at short internuclear distances. While they can asymptotically lead through possible couplings to the same final product state configuration, their electronic symmetry properties do influence fragment properties such as their angular distribution. In particular the electronic symmetries influence the partial reaction cross section as a function of the molecular orientation at the time of the collision which enables to infer the state information from the fragmentation directions. Within the axial-recoil limit, which is introduced in the following section, the measurement of the angular distribution of fragments can thus be regarded as a sensitive probe of the electronic state symmetries and allows a distinct selection of the responsible PES.

For instance, thanks to the high control of the reaction conditions, molecular fragmentation induced by photon absorption has contributed detailed aspects of the inner molecular dynamics in recent decades (an overview is found e.g. in [1, 29]). The high energy resolution of photon beams in laser light sources as well as their large energy range meanwhile achievable, has enabled to scan various molecular systems, both neutral and ionic [23, 30], for the specific reaction pathways. Thereby through the angular distribution of photofragments [31, 32, 33], participating electronic states in the dissociation dynamics could be identified [23, 30] and pushed further ahead the theoretical understanding of these processes.

While photon induced fragmentation is limited by selection rules primarily determined by dipole interactions, electron-driven dissociation processes can access additional electronic

states in the wealth of PESs. As only a single additional, structureless particle of negative charge is involved in these reactions, they appeal particularly to both experimental and theoretical studies. However, simultaneously the number of pathways resulting in different final products rises and leads to a competition between the channels in the total collision process. A few examples of inelastic scattering processes with *neutral* diatomic molecules are listed here :

$$e^- + \text{AB} \rightleftharpoons (\text{AB}^-)^* \rightarrow \quad \begin{array}{lr} \text{A}^- + \text{B} & (2.7) \\ \text{A} + \text{B} + e^- & (2.8) \\ e^- + \text{AB}^* & (2.9) \\ ... & \end{array}$$

Similar reaction types also apply for positively charged diatomic molecules, for instance the process of dissociative recombination introduced in the previous section. In these processes the formation of molecular resonances (e.g. [34, 35]), i.e. intermediate compound states $(\text{AB}^-)^*$ (temporary negative ion (TNI) state) or AB^* (reaction 2.6) of the electron-molecule system, has been found to crucially influence the molecular dynamics, particularly in low-energy collisions ($\lesssim 10$ eV) (e.g. [2] and Sec. 2.3). Depending on the involved electronic states, resonance lifetimes are expected between 10^{-15} s to 10^{-10} s but can in principle also extend to the micro- and millisecond range as recently observed in studies on the H_2^- ion [36]. While the molecular system spends an extended time in the resonant state, possibly propagating upon a repulsive state towards large internuclear distances, different reaction channels can compete with each other. One possibility is the reverse process, autodetachment or autoionization of an electron, which returns the initial reactants often in ro-vibrationally excited states.

The importance of resonances reaches beyond the reaction dynamics of diatomic molecules and was also shown to cause profound effects in polyatomic molecules, clusters and even biomolecules as summarized for the process of *dissociative electron attachment* (DEA; reaction 2.7) in a recent review article [2]. For instance, in experiments exposing DNA in thin films to low-energy electrons (0 - 4 eV) the production of single strand breaks could be observed [37, 38]. Therein the authors suggested a destruction mechanism which is caused through DEA via the formation of intermediate resonant anion states by slow free-electron capture.

For a complete understanding of the fragmentation process the identification of the participating electronic states will be required. In the past, this has inspired in particular for DEA numerous experimental and theoretical studies of the fragment angular distributions
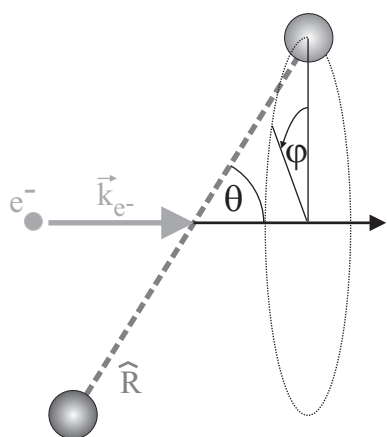
Figure 2.3: Schematic drawing of the electron induced fragmentation of a diatomic molecule. The molecular axis orientation $\hat{R}$ is directed under an angle $\Omega = (\theta, \phi)$ relative to the incident electron momentum vector $\vec{k}_e$.

(Sec. 2.2.2). Stimulated by these ideas together with the similarities to DEA shared by the DR process first theoretical calculations on the angular distribution were also performed for the latter process. The present work makes detailed comparisons of such theoretical predictions with experimental results possible for the first time.

2.2.1 Angular distributions in the axial-recoil limit

The *angular dependence* of a fragmentation process is defined as the functional relation of the differential reaction cross section $d\sigma(\Omega)/d\Omega$ to the orientation of the molecule and is thus linked to the involved electronic symmetries. The orientation of the molecule is typically denoted by an angle Ω (e.g. $=(\theta, \phi)$) with respect to a fixed direction, for instance the momentum of the incident electron $\vec{k}_e$. For electron induced fragmentation of diatomic molecules the orientation of the molecular axis with respect to the incident electron is described by the angles (θ, ϕ), which are schematically displayed in Fig. 2.3. Although the molecules are randomly oriented before the collision, the angular dependence of the reaction induces fragmentation only for those with a preferred orientation. Thus, the resulting *fragment angular distribution*, which describes the angular characteristics of the emitted fragments at the detector, reflects the angular dependence and can reveal an anisotropic electron capture probability. Note, that in most cases, that is for unpolarized electrons and random orientation of diatomic molecules, one can generally assume axial symmetry of the reaction cross section along $\vec{k}_e$, i.e. $d\sigma(\theta, \phi)/d\Omega = d\sigma(\theta)/d\Omega$.

However, the observed fragment positions reflect the initial orientation of the molecule only if the direction of the molecular axis does not change significantly during the fragmentation process. This implies that the molecular rotation is slow in comparison to the time required for dissociation, in particular compared to long-living resonances. In the picture of the potential energy surface diagram these conditions translate to a steep repulsive

dissociation curve as well as small rotational level spacings of the initial bound molecule. Under these assumptions the dissociating products will be traveling in the direction along the molecular axis and the non-rotational or *axial-recoil approximation* (e.g. [39, 40, 41]) is justified. In other words, the *angular dependence* of the initial collision probability is preserved in the *fragment angular distribution*. In particular heavy molecules can be expected to exhibit long rotational periods[2] due to their small rotational constant (see also Sec. 4.3.3).

On the other hand, if the molecule rotates significantly during the fragmentation and the subsequent dissociation process, the fragment angular distribution will be smeared with respect to the angular dependence of the reaction. In fact, the reduction of the fragmentation anisotropies will result in a more isotropic emission characteristic. The breakdown of the axial-recoil approximation has been addressed in numerous publications which were particularly driven by the possible loss of anisotropy influencing photodissociation experiments [43, 44, 45, 46, 47]. Therein the effect on the measurement is partly treated in a semiclassical model [43, 44] independent of the actual fragmentation process which makes an application to the current experiment possible (see Sec. 4.3.3).

2.2.2 Anisotropies in electron-neutral molecule fragmentation

Based on symmetry arguments and the axial-recoil approximation Dunn [39] has first shown that the differential cross section for the production of negative ions by dissociative electron attachment (DEA) (reaction 2.7) [48] should have an angular dependence which is determined by the symmetries of the initial (AB) and intermediate ((AB$^-$)*) molecular state. The derived selection rules consider the cases of parallel or perpendicular alignment of the molecule with respect to the incoming electron $\vec{k}_e$ (see Table I and II in [39]).

A more detailed relationship between the angular dependence of the DEA reaction cross section of diatomic molecules and the electronic symmetry of a resonant state has been suggested by O' Malley and Taylor [41]. They expand their earlier theoretical treatment of the DEA process [48] by the explicit angular dependence and employ the Born Oppenheimer approximation to separate the electronic (Φ) and nuclear (Ψ) parts of the total wave function. The coupling between the initial and final state is then treated in a pure electronic way, i.e. the electronic transition is described by the matrix element $V_{el} = \langle \Phi_d | H_e | \Phi_r \rangle$ of the electronic interaction V_{el}. While the electronic wave function Φ_d corresponds to the electronic state of the intermediate molecular complex formed,

---

[2]For molecules in the lowest excited rotational state ($J^+ = 1$) the classical rotational periods are found in the range of $\sim 10^{-11}$ s for O_2 and $\sim 10^{-13}$ s for H_2 (using the rotational constants from [42]).

the initial state wave function Φ_r contains a plane wave $e^{i\vec{k}_e \vec{r}_e}$ representing the incident electron.

The angular dependence of the fragmentation process essentially comes from the incident electron plane wave which is inserted in the electronic matrix element after an expansion in partial waves:

$$e^{i\vec{k}_e \vec{r}_e} = 4\pi \sum_{L=0}^{\infty} \sum_{m=-L}^{L} (i)^L \, j_L(k_e \, r_e) \, Y_{L,m}^*(\hat{k}_e) \, Y_{L,m}(\hat{r}_e) \tag{2.10}$$

where j_L and $Y_{L,m}$ are the Bessel function and spherical harmonic, respectively, while $\hat{k}_e$ is the unit vector in the incident direction and $\hat{r}_e$ describes the incident electron coordinates, both with respect to the molecular axis $\hat{R}$. After integration over the electron coordinates in the electronic matrix element, conservation of the axial orbital angular momentum between the target Λ_T and resonant Λ_r state restricts the summation over m and L to satisfy $m = \Lambda_r - \Lambda_T$ [41].

In the subsequent part of their calculations it is assumed that the rotation of the molecular axis is fixed during the propagation of the system upon the repulsive PES, i.e. applying the axial-recoil approximation, so that the angular dependence of the differential DEA cross section with respect to the direction of the incoming electron $\hat{k}_e$ follows from:

$$\frac{d\sigma_{DEA}(\theta, \phi)}{d\Omega} \propto \left| \sum_{L=|m|}^{\infty} a_{L,|m|} \, Y_{L,m}(\theta, \phi) \right|^2 \tag{2.11}$$

where $a_{L,|m|}$ are expansion coefficients defined in [41]. The initial $Y_{L,m}^*(\hat{k}_e)$ in Eq.(2.10) with polar axis $\hat{R}$ and coordinates (θ_R, ϕ_R) is expressed here in terms of $Y_{L,m}(\hat{R})$ with polar axis $\hat{k}_e$ and coordinates (θ, ϕ) [41] thus, the electron direction is chosen as reference and (θ, ϕ) describe the angle of the molecular axis. O'Malley and Taylor argue further that Eq.(2.11) can be simplified to only one term (L_0, m_0) for a dominating partial wave of the incident electron.

Under practical aspects these results emphasize that the measurement of angular distributions enables one to infer the participating partial waves of the captured electron. Subsequently, considering the symmetry conservation rules, this information allows one to determine the possible electronic symmetries of resonant states involved in the fragmentation process. The validity of the theory for DEA has been confirmed extensively by several experimental studies at higher electron impact energies mostly in the 1970s and 1980s, for instance on H_2 [49] scanning the resonant production of H^-. Measurements of the H^- angular emission were performed here between 4 eV and $\sim$12 eV, limited on

the low energy side by the small kinetic energy release of the H^- fragments. Later, the theoretical treatment was extended to the angular distribution of negative ions formed in the DEA induced two-body breakup of three-atomic molecular systems such as H_2O [50] and H_2S [51]. For latter cases recent studies have stressed the possible importance of the nuclear dynamics in the final products and obtained in fact a dependence of the angular distribution on the vibrational state of the fragment HS from DEA of H_2S [52].

Most of these experiments have suffered from the limited finite angular range of the detection devices, often consisting of turn-table arrangements which in particular do not cover the forward and backward directions. This has prompted the setup of a true 2π detector (in θ) utilizing the velocity map imaging technique in recent measurements on the DEA of O_2 [53]. The increased sensitivity in the forward and backward direction enabled the presence of the $^4\Sigma_u^-$ resonant state to be identified at electron energies above ~ 9 eV which has not been traced in previous experiments [54] and so far neglected in theoretical calculations.

2.2.3 Angular dependence in dissociative recombination

In contrast to photon induced molecular fragmentation or DEA, involving neutral parent molecules, studies on DR have addressed the role of the molecular orientation with respect to the incident electron in the dissociation process only in recent years. On the experimental side, this can mainly be attributed to the difficulty generally encountered in the efficient detection of all emitted neutral particles yielding the information on their relative positions. Significant progress could thus be achieved once ion storage rings were utilized in order to merge electrons and molecular ions in experiments studying the fragmentation dynamics. In this experimental arrangement, which will be introduced in detail in Ch. 3, the high velocity of the molecular ion is conserved in the subsequent center-of-mass movement of the emitted neutral products, so that they stay in a narrow cone around the initial ion's flight direction.

The angular distribution of the DR fragments is then obtained from their relative positions measured by imaging detectors (see Sec. 3.2). Previous results were mostly discussed on the basis of the symmetry selection rules proposed by Dunn [39] and allowed only a qualitative assignment of the electronic state symmetries involved in the dissociation process (e.g. [55, 56, 57, 58]).

A more detailed theoretical description has become available, which is based on a first explicit treatment of the angular dependence in DR reactions and was performed recently by Guberman [59, 60]. Therein, the differential DR cross section $d\sigma(\theta)/d\Omega$ reveals a

functional dependence on the orientation of the molecular axis, which is determined by the dominantly contributing partial wave of the incident electron. The main steps arriving at this dependence will be summarized here.

The derivation of the DR angular dependence closely follows the one for DEA [41] as well as the scattering theory treatments of DR by Bardsley [28] and Giusti-Suzor [14]. It relies on the axial-recoil approximation, i.e. assumes that only a slow rotation of the molecule during the fragmentation process is applicable so that the product angular distribution directly reflects the angular dependence of the reaction cross section. The process is described in a coordinate frame whose origin lies in the center of charge of the molecule and whose space fixed z-axis is directed parallel to the incident electron momentum vector $\vec{k}_e$ (as shown previously in Fig. 2.3 in Sec. 2.2.1).

The source of the angular dependence is identified in [59] as the electronic coupling matrix element $V_{el}(\vec{k}_e, R)$ which drives the DR process (both in the direct and indirect mechanism):

$$V_{el}(\vec{k}_e, R) = \langle \Phi_d(q_e, R) | H_{el}(q_e, R) | \Phi_r(q_e, \vec{k}_e, R) \rangle \tag{2.12}$$

(equivalent to Eq.(2.4) in Sec. 2.1.3). The initial electronic wave function $\Phi_r(q_e, \vec{k}_e, R)$ represents both the target ion Φ_{ion} as well as the continuum electron $\Phi_{\vec{k}_e}$ in the ion Coulomb field which allows to expand latter wave function into Coulomb partial waves (e.g. [61]):

$$\Phi_{\vec{k}_e}(\vec{r}_e) = 4\pi \sum_{l=0}^{\infty} \sum_{m=-l}^{l} (i)^l e^{i\sigma_l} \frac{1}{k_e \, r_e} F_l(k_e \, r_e) \, Y_{l,m}(\hat{r}_e) \, Y_{l,m}^*(\hat{k}_e) \tag{2.13}$$

where $\vec{r}_e$ denotes the incident electron position with respect to the center of charge of the diatomic ion, F_l is a confluent hypergeometric function, Y_l are spherical harmonics and σ_l is the Coulomb partial wave phase shift. Introduced into Eq.(2.12) this yields the electronic coupling matrix element after integration over all electron coordinates and transformation of $Y_{l,m}^*(\hat{k}_e)$ to spherical harmonics $Y_{l,m}(\hat{R})$ with $\vec{k}_e$ as the polar axis [41] (see previous Sec. 2.2.2):

$$V_{el}(k_e, \vec{R}) = \sum_{l=0}^{\infty} \sum_{m=-l}^{l} V_{l,m}(k_e, R) \, Y_{l,m}(\hat{R}) = \sum_{l=|m|}^{\infty} V_{l,|m|}(k_e, R) \, Y_{l,|m|}(\hat{R}) \,. \tag{2.14}$$

The last step in Eq.(2.14) simplifies the summation due to the restriction of m once the ion and dissociative states are specified by their axial orbital angular momentum Λ_{ion} and Λ_d, respectively, so that $\Lambda_d = \Lambda_{ion} + m$ and considers that $V_{l,m}$ and $V_{l,-m}$ are identical (factor of 2 is included in $V_{l,|m|}$). For a dominant partial wave of the incoming electron, the sum in Eq.(2.14) reduces to a single term only. The angular dependence of the DR

cross section, which is approximately proportional to the square of the transition matrix element, is then shown [59] to be expressed for both the direct and indirect DR mechanism by

$$\frac{d\sigma_{DR}(\hat{R})}{d\Omega} \propto \left\| Y_{l,|m|}(\hat{R}) \right\|^2 . \tag{2.15}$$

Consequently, similar to the expression derived for DEA (Eq.(2.11)) the angular dependence in DR is given by the square of the absolute value of the dominating partial wave spherical harmonic and mirrors the electronic symmetries of the participating states.

Considering this recent description of DR angular dependences, previous experimental studies can be re-interpreted. So far, mostly molecular systems have been studied, where a number of dissociation pathways are accessed at *high* impact energies ($\gtrsim$1 eV), measuring several superimposed final product channels [55, 56, 57]. An independent analysis of the individual fragment angular distributions is limited in those cases by the detection technique and hinders the detailed comparison to theoretical predictions. In turn only the appropriate angular distributions will allow to infer correctly the branching ratios between the different product channels from these measurements.

At *low* electron energies ($\sim$10 meV) the electrons mostly no longer approach the molecule from a single direction due to their finite velocity distribution. Consequently the superposition of incident electron directions has to be taken into account accordingly in the comparison of the measured fragment angular distributions to the predicted angular dependence calculated for a fixed electron impact direction. First studies on the DR fragment angular distributions of O_2^+ in slow electron collisions have been presented recently [62]. They observed at electron energies $E \lesssim 300$ meV up to four closely superimposed final product channels. Within the accuracy of the measurement they found each channel to be compatible with an isotropic angular distribution. This is in contradiction to theory [59] which has predicted for the O_2^+ system different anisotropies depending on the electronic symmetry of the dissociative state.

These previous experiments have shown that a detailed study of the DR angular dependence, in particular at low electron collision energies, will require (a) the use of *unidirectional* electrons and (b) a molecular system with only *one* final product channel such as the hydrogen molecular cation discussed in the subsequent section.

2.3 Dissociative recombination of the hydrogen cation

The hydrogen molecular cation, H_2^+, has been the object of numerous experimental and theoretical studies. Its simple structure allows accurate theoretical calculations so that it

has become a benchmark molecule for detailed comparisons between theory and experiments.

The H_2^+ ion shares the electronic structure with its deuterated relative HD^+, but is often favored in theoretical calculations due to its additional symmetry of equal masses. On the other hand, the masses of the nuclei not only affect the level spacing of the bound system but provide HD^+ with a permanent dipole moment, which enables radiative interaction. Many experiments aiming at defined initial conditions thus prefer the HD^+ ion as its vibrational excitations arrive within ~ 100 ms at an equilibrium level population with the ambient background radiation; mainly in the vibrational ground state with only a few rotational states excited[3] [63] (see also Sec. 4.1).

These considerations also hold for studies on dissociative recombination of this diatomic molecular system. In recent years, its reaction process was predominantly addressed by experiments at heavy-ion storage ring facilities. Thereby, comparisons of the HD^+ DR rate coefficient measured as a function of the electron collision energy in independent experiments performed at ASTRID in Aarhus, CRYRING in Stockholm and TSR in Heidelberg [13] have revealed an almost perfect agreement considering the various experimental electron energy spreads (see Fig. 2.4). Together with advancements in theoretical treatment the key processes are meanwhile identified, whereas detailed aspects still remain unsettled.

2.3.1   Low-energy DR resonances of the hydrogen cation

The dissociative recombination of the hydrogen cation from the ground electronic state of $(1s\sigma_g)^2\Sigma_g^+$ symmetry is driven by both the direct and the indirect mechanism (see Sec. 2.1.3), depending sensitively on the electron collision energy. Since the indirect pathway is limited by the availability of neutral bound Rydberg states to energies below the dissociation threshold of the ground ionic state[4], DR at higher electron energies relies on the existence of repulsive states which serve as the doubly excited states in the direct mechanism. Two series of anti-bonding Rydberg states converging to the first and second electronically excited ionic state of $(2p\sigma_u)^2\Sigma_u^+$ and $(2p\pi_u)^2\Pi_u$ symmetry, respectively, have been identified as possible dissociation pathways in the energy range up to $\sim$20 eV and are generally referred to as Q_1 and Q_2 series [66] (see Fig. 2.5). Their energetic ranges

---

[3]Assuming Boltzmann distributed rotational states of the ions at 300 K the largest J^+-state contribution is given by $J^+ = 2$ ($\sim$25%) , whereas $J^+ \geq 5$ are populated less than 10%.

[4]Dissociation energies differ between $E_{d,H_2^+} \approx 2.650$ eV [64] and $E_{d,HD+} \approx 2.669$ eV [65] of the H_2^+ and HD^+ ion, respectively.
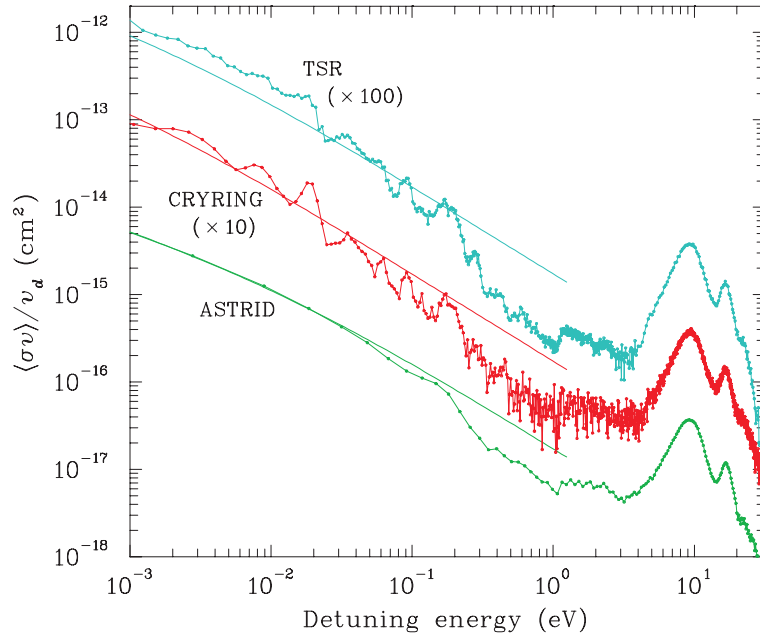
Figure 2.4: Comparison of the DR cross section of HD$^+$ measured at three different storage rings until 2001 (blue: TSR, red: CRYRING, green: ASTRID) [13] as a function of the electron energy. The cross sections of the TSR and CRYRING have been shifted by a factor of 10 or 100, respectively, for clarity. The smooth lines represent a model cross section $\sigma(E) = A/E$ which has been folded by the electron temperature of ASTRID and to the ASTRID data at low energy.

coincide with two broad resonant peaks observed above $E \approx 3$ eV already in first HD$^+$ DR rate measurements at the TSR [67].

At low collision energies the electrons can interact only with one doubly excited dissociative state, the PES of $(2p\sigma_u)^2$ $^1\Sigma_g^+$ symmetry, which crosses the electronic ground state of the hydrogen cation between the $v^+ = 0$ and $v^+ = 1$ vibrational levels.

Alternatively, the indirect DR process becomes possible, when the electron forms through non-adiabatic couplings a temporarily bound, ro-vibrationally excited neutral Rydberg state which predissociates upon the same doubly excited state $(2p\sigma_u)^2$ $^1\Sigma_g^+$. The formation of the intermediate Rydberg states sensitively depend on the electron energy as well as the initial ionic excitation and hence ro-vibrational Feshbach resonances appear in the electron-molecular ion scattering process. Both reactions, the direct and indirect, cannot be treated independently as they interfere at low electron collision energies as pathways of compatible strength and result in a complex structure of the DR cross section. The calculated interferences are mainly destructive compared to a pure direct dissociation,
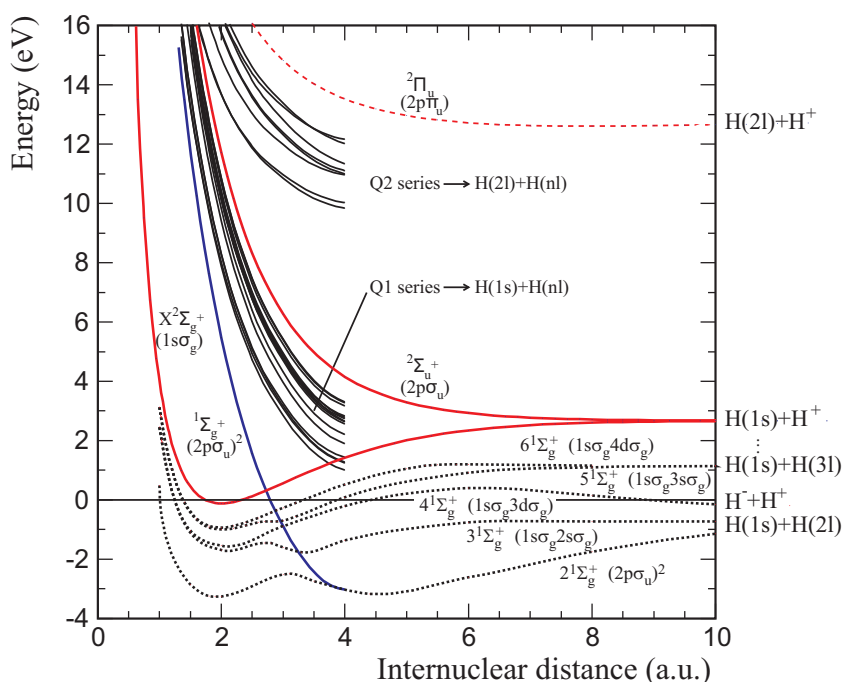
Figure 2.5: Potential energy curves of H_2^+ and H_2 [68]. Solid red curves: adiabatic curves of the lowest two ionic states. Dashed red curve: second excited ionic curve. Dashed black curves: adiabatic curves of the lowest excited bound Rydberg states of H_2, showing avoided crossing with the lowest Q_1 curve (solid blue curve). Solid black lines: Q_1 and Q_2 series of doubly excited states converging to the ionic limit. The final atomic fragment states are shown on the right.

leading to dips in the cross section beside small peaks. The form depends on the nature of the involved interactions and reflects the relative magnitude of the generally fast direct DR compared to the weak ro-vibrational coupling in the indirect mechanism [27, 69, 70]. Experimentally, rather large energy variations are found [13], with the cross section mostly (Fig. 2.4) remaining below the one calculated for the direct process.

Although in case of HD^+ only a few ionic rotational states in the vibrational ground state are typically populated in experiments, numerous intermediate Rydberg states remain energetically accessible. The nuclear rotational levels J^+, J' of the initial and the intermediate HD^+ ion core are only restricted through conservation of total angular momentum by $\Delta J = |J' - J^+| \leq 2l_{Ryd}$ [16] (for labels see also Eq.(2.6)). This still leaves a large number of reaction channels for the calculation of the indirect DR process which could later be accounted for in the ro-vibrational expansion of the Multichannel Quantum Defect Theory (MQDT) [15, 16].

In low-energy DR of the hydrogen molecular cation, where only the dissociative state of

$^1\Sigma_g^+$ symmetry is reached either directly or through predissociation, the angular momentum quantum number l of the incident electron partial wave is limited to even values only. Rydberg series $(1s\sigma_g)(nl_{Ryd}\sigma_g)^1\Sigma_g^+$ converging to the ionic state $(1s\sigma_g)^2\Sigma_g^+$ with odd angular momentum l_{Ryd} $(= l)$ of the outer electron will not be able to couple to the dissociative state $^1\Sigma_g^+$ due to symmetry reasons (parity conservation). Furthermore high-l partial waves are found with negligible reaction amplitudes only (e.g. [16, 71]) so that they are unlikely to provide an efficient reaction path. This leaves s and d partial-waves with symmetry σ_g. While latter is considered to be dominant in the DR process through the strongest electronic coupling [14], the s-wave has been found to play an important role in the resonant structure of the DR cross section, especially at low energies [72]. Latest MQDT calculations have thus taken into account both Rydberg series, $s\sigma$ and $d\sigma$, in a ro-vibrational approach [16] finding good agreement with high resolution HD$^+$ DR rate measurements [17].

Coming back to the angular dependence of the reaction, a dominant d partial-wave in the HD$^+$, or H$_2^+$, DR process will imply an anisotropic fragmentation described by the $Y_{2,0}$ spherical harmonic according to Eq.(2.15). The hydrogen molecular cation presents an ideal system to verify these theoretical predictions experimentally. In fact, with only one final atomic product configuration (e.g. HD$^+$: [H(n) + D(n')] or [H(n') + D(n)] with $n=$ 1 and $n'=$ 2 [55]), which is accessed at low electron impact and low internal ionic excitations ($E < 1.14$ eV and vibrational state $v^+ <$5) through dissociation upon $(2p\sigma_u)^2$ $^1\Sigma_g^+$ (Fig. 2.5), the observed fragment angular distributions can precisely be analyzed with respect to the role of molecular orientation in the electron capture. Furthermore, the defined final fragment states confine the kinetic energy release of the escaping fragments. Varying amounts of the kinetic energy distributed among the products will directly allow to infer the ro-vibrational ionic states contributing in the DR process.

Fast beam fragment imaging

Studying the dynamics in molecular fragmentation processes involves a good control both on the collision partners and products. In fast ion beam setups combined with heavy-ion storage rings molecular beams of high quality can be prepared in multi-turn circulation by merged collinear electrons. The fast ions thereby enable high resolution electron collision studies at low relative energy. In addition an effective 4π neutral fragment detection becomes possible for the complete reconstruction of the product kinematics

In the following sections both the general concept of storage ring experiments and the fragment velocity measurement will be introduced as a powerful tool for molecular physics. The realization of these general ideas at the facility of the Max-Planck-Institut für Kernphysik in Heidelberg, Germany, has opened up the feasibility of the experiments described here, so that the chapter concludes with the details of the heavy-ion Test Storage Ring (TSR) as well as the multi-hit fragment imaging detection system.

3.1 The ion storage ring technique

Heavy-ion storage rings have successfully been used for numerous experiments in molecular physics by now for almost 20 years [8, 73]. Produced by an ion source and accelerated to the desired energy of up to a few MeV per nucleon, the molecular ion beam is injected into the storage ring and stored by means of magnetic fields on a closed orbit.

From the high beam velocities the neutral fragment detection benefits particularly. As the kinetic energy released in the molecular fragmentation process is typically small with respect to the molecular ion momentum, all neutral fragments will stay within a narrow cone pointing in forward direction. This allows an effective 4π neutral fragment detection on a small detector surface downstream of the interaction region.

Besides the advantage of having fast molecular ion beams the experiments also profit from

storing them. Typical storage times of up to tens of seconds for molecular beams can be reached, only limited by the probability of destructive residual gas collisions which are generally mostly suppressed in the ambient ultra high vacuum of the storage ring. The hardly disturbed circulation thus gives superior advantages of the multi-pass arrangement over single-pass experiments.

For example, the long storage times allow to prepare the molecular ions both passively and actively. Coming from standard molecular ion sources the ions are usually internally excited when entering the storage ring. Those which are infrared active can then radiatively cool vibrations and rotations to the surrounding thermal equilibrium temperature levels (≈ 300 K). In most cases the vibrational ground state is reached within milliseconds, whereas the lowest rotational state equilibrium distribution is achieved on a timescale of seconds. Then again this cooling process can also be studied simultaneously by tracing the individual molecular state populations as functions of storage time.

In a dedicated section of the storage ring, the electron cooler, continuously regenerated electrons can be merged. They provide the possibility to manipulate actively the ion beam quality and countervail heating effects such as intra-beam scattering. Electrons of low energy spread and matched to the velocity of the ion beam interact over Coulomb forces with the molecular ions. Through this process of phase-space cooling the molecular ions' kinetic energy spread is rapidly reduced and approaches the thermal electron energy distribution within less than one second for certain light molecules. The molecular ions are then accumulated within a high density beam of small divergence and diameter. Subsequently, electron collision experiments, such as dissociative recombination, profit from the defined fast ion beam velocities as small relative electron collision energies can be realized with highest resolution for precise studies down to the meV range. On the other hand, in non-destructive inelastic electron scattering, the electrons can also absorb part of the internal energy, cooling actively the internal excitations of the molecular ions and leaving behind stored molecules in lower rotational and vibrational (ro-vibrational) states.

Beneficial for electron collision experiments, such as dissociative recombination, is also the possibility of continuously recycling the molecular ion beam through circulation on a closed orbit. Thereby the number of reactions for each injection and thus the efficiency of collision studies at low reaction rates or ion currents can be increased by a multiple.

Summarized, the fast ion storage ring technique brings together electrons and molecular ions at well defined conditions. This is a crucial requirement for controlled studies of the various aspects of the electron induced molecular fragmentation process addressed in this work.

3.2 Neutral fragment imaging

Combining the ion storage ring technique with fragment imaging detection creates a powerful tool aiming at the reconstruction of the molecular fragmentation kinematics through the determination of the relative fragment velocities [74]. For the dissociative recombination process studied here this opens up the possibility to focus on such aspects as the kinetic energy release, internal excitation and angular distribution of the escaping neutral fragments.

In the imaging technique the relative fragment velocities are reconstructed from the recorded particles' impact positions and arrival times at the detector. Simple imaging systems are usually restricted to the measurement of the fragment distances projected onto a surface perpendicular to the flight direction; i.e. only yield transverse velocities. Thus not the full reaction kinematics is observed and information on the kinetic energy release and the angular distribution have to be obtained indirectly. The imaging technique is then referred to as *2D-Imaging*. For a full kinematic picture the complete fragment distance is needed which has to be obtained for instance from both the relative positions transverse to the flight direction as well as the time differences of all fragments. The experimental technique which comprises a simultaneous measurement of these properties is called *3D-Imaging*. Both types of fragment imaging methods have found numerous applications in molecular physics research where fragmentation processes induced, for example, by photons or electrons [75, 76, 77] are studied.

For dissociative recombination the imaging technique yields the fragmentation kinematics directly from the complete measurement of the neutral fragment velocities. This requires the detection of all emitted neutral particles and is possible at fast ion beam storage rings where the fragment trajectories, due to the small kinetic energy release, describe a narrow cone in forward direction and are thus projected onto a small detector surface.

However, the deduction of the relative fragment velocities becomes complicated with an increasing number of emitted fragments. Since this work is focused on diatomic systems only, the following description of the fragment kinematics is restricted to the 2-body breakup. A detailed treatment of the polyatomic case can be found e.g. in [78].

3.2.1 2-body fragmentation kinematics

In Fig. 3.1 the principle of the imaging technique is illustrated for the fragment trajectories of a diatomic dissociative recombination event. Here, the diatomic molecular ion AB^+ dissociates after the capture of an electron into two neutral fragments A and B. At
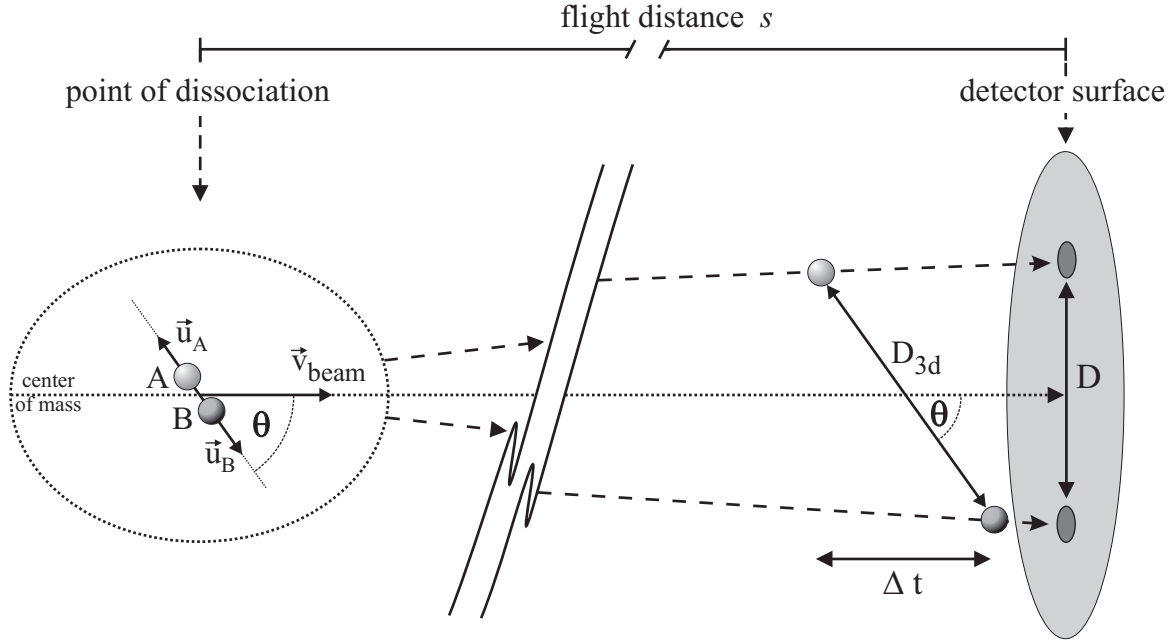
Figure 3.1: Trajectories of the neutral fragments A and B stemming from a 2-body breakup event at a distance s from the detector.

the point of dissociation, the temporarily formed neutral compound AB travels at the ion beam velocity $\vec{v}_{beam}$ and its molecular axis orientation is directed with an angle θ to the ion beam direction. The energy set free in the dissociation process is transferred to kinetic energy $E_{kin,i}$ $(i = A, B)$ and possible internal excitation of the fragments, resulting in asymptotic fragment velocities $\vec{u}_i$ in the co-moving center-of-mass (c.m.) frame of the molecule. The total kinetic energy release

$$E_{KER} = E_{kin,A} + E_{kin,B} = \frac{1}{2}\mu\, v_{rel}^2 \tag{3.1}$$

can then be expressed in terms of the relative velocity $\vec{v}_{rel} = \vec{u}_A - \vec{u}_B$ and the reduced mass $\mu = \frac{m_A m_B}{m_A + m_B}$ of the fragment masses m_i. Under conservation of the total momentum the directions of the velocity vectors $\vec{u}_i$ are determined from the initial orientation of the molecule and the dissociation dynamics.

In the laboratory frame the fragments move at the total velocity $\vec{v}_i = \vec{v}_{beam} + \vec{u}_i$ until they reach the detector after a flight distance s. At the point the first particle hits the detector the distance between the fragments has grown to a macroscopic value D_{3d}

$$D_{3d} = \frac{v_{rel}}{v_{beam}}\, s \tag{3.2}$$

depending through $\vec{v}_{rel}$ on the kinetic energy release and by assuming $v_{beam} \approx v_i$. The impact positions at the detector can then be described by the projected fragment dis-

tances D transverse to the beam direction as well as the time difference Δt between the fragment arrivals. For the current experiments the flight distances are much larger than the fragment distances ($s \gg D_{3d}$), which allows to relate both the transverse distance D and the time difference Δt through orthogonal projections to D_{3d} :

$$
\begin{aligned}
D &= D_{3d} \sin\theta & (3.3) \\
\Delta t &= D_{3d} \cos\theta / v_{beam}\,. & (3.4)
\end{aligned}
$$

This results for the molecular systems and experimental conditions discussed in this work in typical transverse distances of a few centimeters and time differences of few nanoseconds.

From the determination of both the impact positions and times of the fragments one can directly obtain the properties of the fragmentation kinematics such as the kinetic energy release. Here one should keep in mind that the fragmentation angle θ measured at the detector can reflect the initial molecular axis orientation at the start of the fragmentation process if the axial-recoil approximation (see Sec. 2.2.1) is valid for the specific case.

3.2.2 Transverse distance information

In *2D-Imaging* experiments only the transverse fragment distance D of a diatomic breakup is recorded, whereas the information on the relative fragment impact times is missing. Therefore it is impossible to reconstruct the kinetic energy release E_{KER} and the fragmentation geometry from the measured distance D on an event-by-event basis. Nevertheless, this information can still be extracted from *2D-Imaging* measurements by comparing an accumulated distribution of distances D to a transverse distance probability distribution $F(D)$ expected for specific fragmentation kinematics [56].

For a single event the transverse distance D between the two fragments of a diatomic breakup can be rewritten in terms of the flight distance s, the maximum fragment emission angle δ in the laboratory frame and the fragmentation angle θ in the co-moving reference frame:

$$
D = s\,\delta\,\sin\theta\,. \tag{3.5}
$$

The angle δ is proportional to the ratio of the kinetic energy release as well as the ion beam energy E_{beam} and follows from Eqs.(3.1, 3.2) :

$$
\delta = \frac{m_A + m_B}{\sqrt{m_A m_B}}\,\sqrt{\frac{E_{KER}}{E_{beam}}}\,. \tag{3.6}
$$

Collecting the transverse distances for a number of events dissociating at a defined distance s from the detector yields a probability distribution $F_s(D)$ which is directly related to the

angular distribution $W(\theta)$ of the emitted fragments [79]

$$F_s(D) = \frac{D}{\delta^2 s \sqrt{s^2 - (D/\delta)}} W(\theta) \ . \tag{3.7}$$

In the next step, this description has to be adopted to the non-point-like electron-ion interaction region of length L experienced in the electron target section during experiments (see Sec. 3.3). The transverse distance distribution $F_s(D)$ is thus integrated over all possible flight distances ($s_2 \geq s \geq s_1$ with $s_2 - s_1 = L$), assuming equal dissociation probability along the overlap with electrons, in order to yield the total expected distribution $F(D)$. Hence, the resulting functional dependence of $F(D)$ is influenced by two essential properties of the fragmentation process: the *kinetic energy release* and the *fragment angular distribution.*

Comparing the initial internal excitation of the molecular ion above ground state, which is given by vibrations v^+ and rotations J^+, to the excitations of the final fragment states (n_A, n_B), yields together with the electron collision energy the kinetic energy available to the emitted particles. In experiments usually a number of initial and final states can contribute, so that the measured transverse distance distribution $F(D)$ is described by a sum of expected distributions $F_{v^+, J^+, n_A, n_B}(D)$, each for a different kinetic energy E_{KER},

$$F(D) = \sum_{v^+, J^+, n_A, n_B} b_{v^+, J^+, n_A, n_B} F_{v^+, J^+, n_A, n_B}(D) \tag{3.8}$$

and with relative contributions b_{v^+, J^+, n_A, n_B} to the total recorded spectrum [80].

The general angular distribution $W(\theta)$ in the co-moving frame relative to the beam direction can be expressed thanks to the axial symmetry of the emitted particles with respect to the beam axis in terms of Legendre polynomials $P_l(\cos\theta)$

$$W(\theta) = \sum_l a_l P_l(\cos\theta) \tag{3.9}$$

with Legendre coefficients a_l of order l. Due to the properties of the Legendre polynomials, even order contributions are symmetric in θ and $\theta - \pi$ in contrast to the odd contributions. The latter type translates for a diatomic breakup to a difference of the angular distribution rotating any fragment direction by $\theta = \pi$, corresponding to a so called *forward-backward asymmetry.* In measurements of the transverse distance D alone, θ and $\theta - \pi$ are not distinguishable so that odd Legendre polynomials are not recognized. In fact, an odd-type contribution in $W(\theta)$ will be averaged out to an isotropic shape $F(D)$. Consequently, transverse distance distributions enable the determination of $W(\theta)$ represented by even Legendre polynomials only [56].

The total distribution $W(\theta)$ is normalized such that $a_0 = 1$. Each even order polynomial $P_l(\cos\theta)$ and initial-to-final-state channel (v^+, J^+, n_A, n_B) is then converted to a transverse distance distribution $F_{l;v^+,J^+,n_A,n_B}(D)$ so that one finally arrives after the summation over all contributions at the total function $F(D)$

$$F(D) = \sum_{v^+,J^+,n_A,n_B} \sum_l b_{v^+,J^+,n_A,n_B}\, a_{l;v^+,J^+,n_A,n_B}\, F_{l;v^+,J^+,n_A,n_B}(D)\,. \qquad (3.10)$$

Note that in this general form also the Legendre coefficients depend on the reaction channel, i.e. each initial-to-final-state channel can contribute to the total distribution with different weighting factors and angular dependences. The parameters b_{v^+,J^+,n_A,n_B} and $a_{l;v^+,J^+,n_A,n_B}$ are then extracted from a least-square fit to the measured transverse distance distribution.

Earlier fragment imaging experiments studying the DR initiated breakup of diatomic molecules have identified contributions of Legendre polynomials of $l \leq 2$ only (see e.g. [55, 56, 57]). In contrast, the experiments presented here are found to require angular distributions also of type $l = 4$ as will be discussed later (Sec. 4.2.2). Contributions from higher orders were found to be insignificant and therefore set to zero in the final analysis. The parameter range for the Legendre coefficients a_l ($l = 2, 4$) of the angular distribution $W(\theta)$ is thereby restricted through

$$W(\theta) = P_0(\cos\theta) + a_2 \cdot P_2(\cos\theta) + a_4 \cdot P_4(\cos\theta) \geq 0 \qquad (3.11)$$

requiring only non-negative values of $W(\theta)$ ($[0 \leq \cos\theta \leq 1]$) and is represented by the white area (including its surrounding black edge) in Fig. 3.2(a). The remaining insets (b,c,d) of Fig. 3.2 show sample line shapes of expected transverse distance functions $F(D)$ computed for selected (a_2, a_4)-coefficients (marked by color-coded dots in (a)) of a single reaction channel (v^+, J^+, n_A, n_B). The explicit functional dependences $F_l(D)$ associated with the 0th, 2nd and 4th order Legendre polynomials can be found in Appendix A. Window (b) also illustrates for an isotropic angular dependence the sensitivity of the distribution, in particular of its right edge, on the kinetic energy release. Here the single-channel $F_{l=0}(D)$ is compared to a sum of reaction channels differing by the kinetic energy release of Boltzmann distributed ionic rotational states (for the case of HD^+ ions at 300 K). This has been employed to trace rotational state contributions in the experiments as will be described in Sec. 4.2.1.
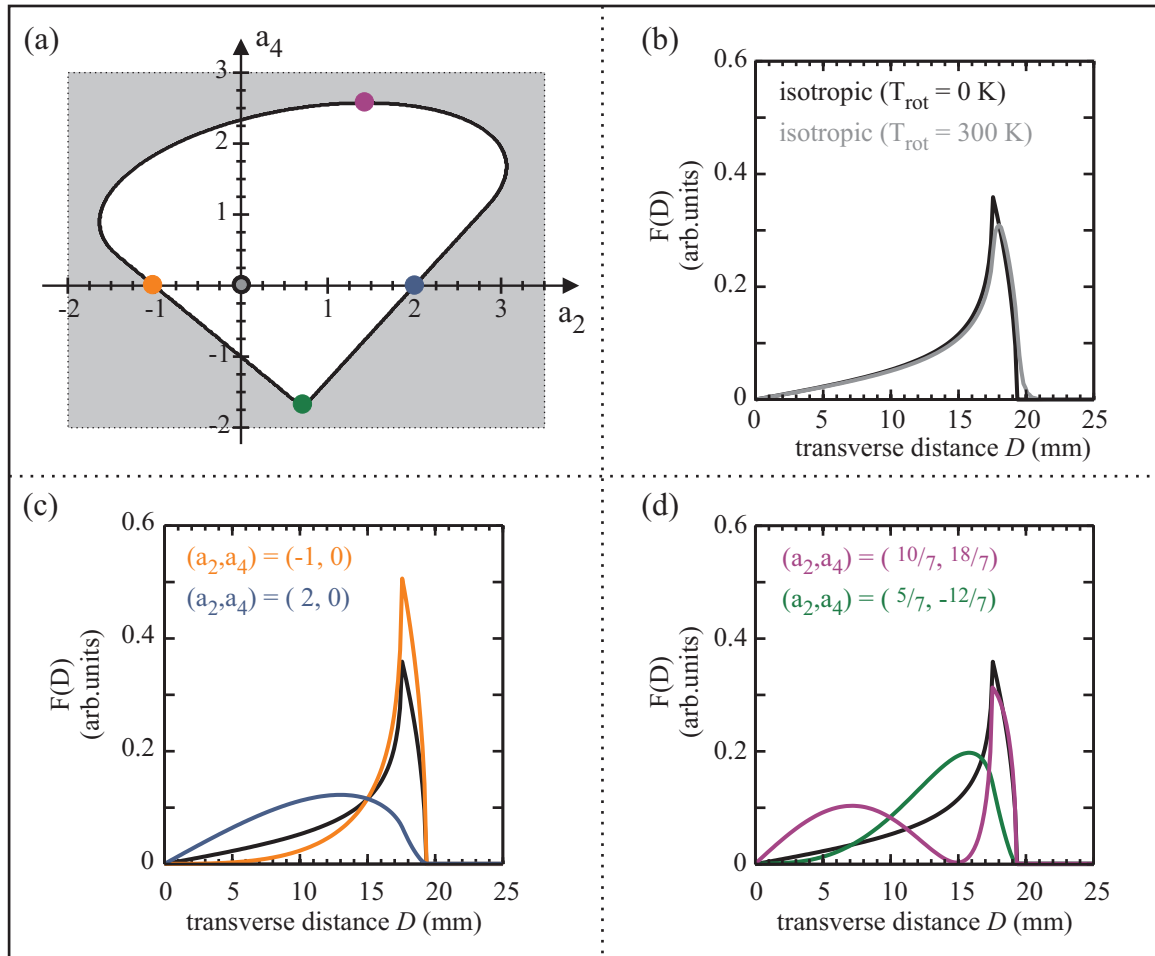
Figure 3.2: (a) The allowed (a_2, a_4) parameter range (white area including the black edge) for the 2nd and 4th order Legendre polynomials yielding $W(\theta) \geq 0$ is displayed. The windows (b,c,d) show the transverse distance line shapes for single reaction channels and selected (a_2, a_4) combinations (marked by color coded dots in (a)). The purple line $(10/7, 18/7)$ in window (d) reflects the angular distribution for a pure d partial-wave coupling (see Sec. 4.3.1). In (b) the single-channel distribution is compared to the one expected for a sum of Boltzmann distributed rotational state contributions (300 K HD$^+$ ions). Note the shift of the right edge towards larger distances.

3.3 Experimental setup

All experiments presented in this work were performed at the heavy-ion Test Storage Ring (TSR) of the Max-Planck-Institut für Kernphysik in Heidelberg, Germany [81]. The facility provides a variety of ion sources and two accelerators for the production of a wide range of molecular ion beams which can then be injected and stored in the TSR at energies

of the order 1 MeV per nucleon.

The tandem Van-de-Graaff accelerator is designed in particular for the production of heavy and highly charged atomic ion beams, such as Sc^{18+} [82], and well suited to yield heavier molecular ions of type CH_2^+ [83] and CF^+ [84]. The HSI (Hoch-Strom-Injektor, High Current Injector) on the other hand, is a modular accelerator system which can deliver high currents of light, singly charged molecular ions with a minimum charge to mass ratio $q/m = 1/9$ [85]. Therefore latter device has been used to accelerate the HD^+ and H_2^+ molecular ions subject to the research in this work. The HSI system basically consists of an exchangeable ion source, two Radio Frequency Quadrupole (RFQ) resonators [86] for acceleration of slow beams and eight 7-gap resonators [87] for additional acceleration. Depending on the number of accelerator structures used, molecular ion beam energies between 0.24 and 1.7 MeV per nucleon can be achieved. For the H_2^+ and HD^+ ion beam acceleration two RFQ units were applied, reaching final total beam energies of 0.96 MeV or 1.44 MeV, respectively.

At the HSI numerous ion sources are available taking in also the possibility to mount externally developed and built devices which may yield specific ion beam conditions. The HD^+ molecule is produced here as a standard ion beam through electron impact ionization of neutral HD gas in a Penning ion source. In the H_2^+ measurements a high emphasis was put on the state selectivity of the experiment. Hence a specific laser ion source (LISE), developed at the University of Louvain-la-Neuve, Belgium, was utilized to produce ro-vibrationally selected molecular ions [88].

After production and acceleration to the desired energy the molecular ions are injected into the TSR using a multiturn injection scheme and stored on a closed orbit confined by bending and focusing magnets. In the 55.4 m circumference storage ring, outlined in Fig. 3.3, the vacuum pressure is generally kept in the order of 10^{-11} mbar to reduce destructive residual gas collisions and allow experiments even after several tens of seconds after beam injection.

3.3.1 The twin-merged beam facility at the TSR

At the TSR two electron beams can be merged simultaneously in independent straight sections with the circulating molecular ion beam, turning the facility into a twin-merged beam setup. Combined with an electron beam of ultimately low energy spread this setup enables collision experiments at highest resolution.

The purpose of overlapping the molecular ions with electrons is twofold for the experiments described here. Firstly, the continuously renewed single-pass electrons can co-propagate
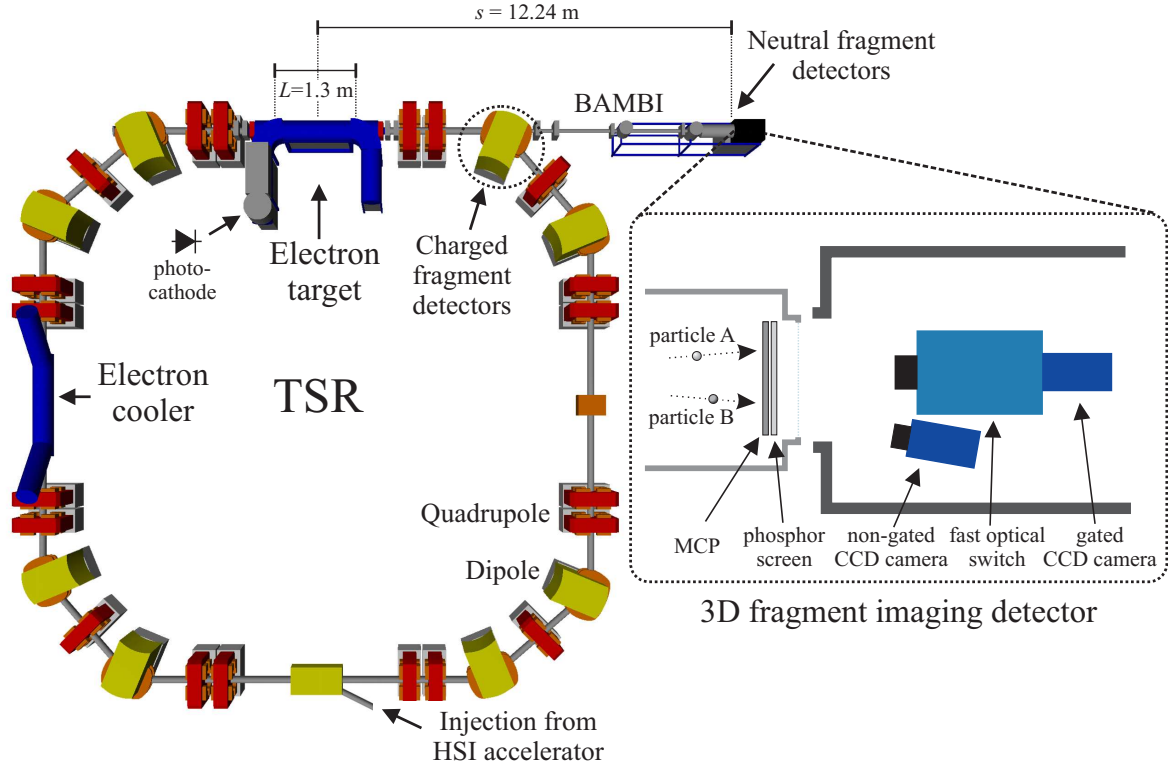
Figure 3.3: The twin-merged beam setup at the TSR consisting of the electron-cooler and electron-target section (ETS). Neutral fragments are recorded downstream of the ETS by counting detectors or the multi-hit 3D fragment imaging system (see Sec. 3.3.2) which can interchangeably be operated at the neutral particle beamline BAMBI (Beamline for Advanced Molecular Breakup Investigations).

velocity matched with the ions. Through elastic collisions the electrons absorb part of the molecule's kinetic energy and achieve *phase-space cooling* [89, 90] of the ion beam velocity distribution within a short storage time. The molecules' velocity spread is then determined by the electron beam thermal velocities $\vec{v}_e = (v_\perp, v_\parallel)$ which are described by an anisotropic flattened double Maxwellian distribution [91]

$$f(\vec{v}_e, v_d) = \frac{m_e}{2\pi k T_\perp} \left(\frac{m_e}{2\pi k T_\parallel} \right)^{1/2} e^{\left(-\frac{m_e v_\perp^2}{2k T_\perp} - \frac{m_e (v_\parallel - v_d)^2}{2k T_\parallel} \right)} \tag{3.12}$$

at a given detuning velocity v_d with respect to the ion beam velocity and defined by the transverse $T_\perp$ and longitudinal $T_\parallel$ (parallel to the ion beam) temperature in the co-moving frame (m_e is the electron mass and k the Boltzmann constant). In addition, the geometrical dimensions of the continuously circulating ion beam obtain a low divergence and a diameter < 1 mm (standard deviation) for HD^+.

Secondly, the electrons can also be used for electron-ion collision experiments. Depending on the aim of the experiment electrons from velocity matching to defined detuning values v_d can be provided with an accuracy limited mainly by the electron thermal velocity spread.

Consequently, distributing both tasks among two independent electron beams has the advantage to perform collision experiments under stable ion beam conditions and for variable electron energies. This has become possible at the TSR where the option of using two electron beam devices became operational in recent years (see Fig. 3.3). For the present experiments the *electron cooler* was assigned to constantly define the ion beam energy with electrons accelerated to the velocity matching value. Independently from the electron cooler the electrons generated in the *electron target* [92, 93] were tuned to well defined energies to study the collision process.

The thermal electron energy spread, mainly limiting the measurement's energy resolution, depends critically on the electron beam production. At the electron target there are optionally two types of electron emitters available [94]: a thermal cathode and a liquid nitrogen cooled GaAs-photocathode [95, 96]. Latter electron source emits electrons by laser illumination at a low initial temperature of $T_{cath.} \approx 100$ K. The slow acceleration to the ion beam velocity reduces the initial temperature in the longitudinal component to $kT_\parallel \approx 0.03$ meV, whereas an adiabatic expansion in a decreasing magnetic guiding field is responsible for achieving a sub-meV transverse electron temperature ($kT_\perp \approx 0.5$ meV). For the present experiments (HD$^+$) an electron beam with a typical current of $I_e \approx 0.35$ mA and a density in the range of $n_e \approx 1 \times 10^6$ cm^{-3} was used (more details in Chapters 4 and 5). The electron temperatures were derived from the sharpest structures in earlier energy dependent DR rate measurements [97]. In comparison the thermal cathode principally yields higher electron currents and densities, but at the cost of increased electron temperatures due to the higher initial temperature $T_{cath.} \approx 1000$ K ($kT_\parallel \approx 0.045$ meV and $kT_\perp \approx 2.0$ meV).

The second electron beam device, the electron cooler, is only equipped with a thermal cathode which emits an electron beam with a density of 1.6×10^7 cm^{-3} at thermal electron temperatures of $kT_\perp \approx 10.0$ meV and $kT_\parallel \approx 0.1$ meV transverse and parallel to the beam direction, respectively.

The superior performance of the photocathode electron beam in the electron target thus explains the preference of the electron-target section (ETS) for the study of electron-molecule collisions down to the low-meV energy range. Various detectors have been installed downstream of the electron target awaiting charged and neutral fragments originating from the interaction region. Positive and negative ion detection takes place already

in the first dipole succeeding the electron target. While positively charged ions are mainly studied in dielectronic recombination measurements of atomic ions [94], the negative ions give insights on the ion-pair formation in the DR process. Both types of product charged particles and the neutral fragments arising from DR events in the ETS are separated from each other and from the circulating ion beam by the storage ring dipole directly downstream of the electron target. The neutral particles enter the newly created particle beamline BAMBI (Beamline for Advanced Molecular Breakup Investigations) [17]. Here, currently three detectors can interchangeably be brought in to identify DR events through the quasi-simultaneous arrival of neutral fragments. At a distance of about 12 m from the electron target center two energy sensitive surface barrier detectors of different sizes are used for event-by-event counting experiments in DR rate measurements [17]. For the study of the fragmentation kinematics a multi-hit 3D fragment imaging detector has been set up within the present experimental project [98, 99], which will be discussed in the following section.

3.3.2   The multi-hit 2D and 3D fragment imaging detector

In order to reconstruct the complete kinematics in molecular fragmentation, the determination of the relative fragment velocities is necessary. The 3D fragment imaging technique outlined in the previous Section 3.2 offers the possibility to obtain the kinematics through the determination of the relative fragment positions, i.e. the transverse impact distances and their impact times at the detector. Of these, the time measurement on the nanosecond scale sets the main challenge to achieve highest resolution, whereas transverse fragment distances of a few centimeters can usually be determined within about 100μm accuracy. The fragment imaging system used in the experiments comprises both the possibility of 2D and 3D imaging. The detection principle [100] is independent of the number of fragments and can thus easily be extended to the study of multi-fragment dissociation stemming from polyatomic molecules. The following introduction to the detection system gives a brief overview on the detector's operational principle, with emphasize on latest developments in the subsequent paragraphs.

Simultaneous time and position measurement

The fragment imaging detector awaiting the particles at the end of the BAMBI beamline (1224(2) cm from the electron target center) is schematically drawn in the inset of Fig. 3.3. The setup basically consists of two detection stages: First, the impact of a fragment on a 78 mm diameter micro channel plate (MCP; Chevron type, Hamamatsu$^{\copyright}$) [101] creates
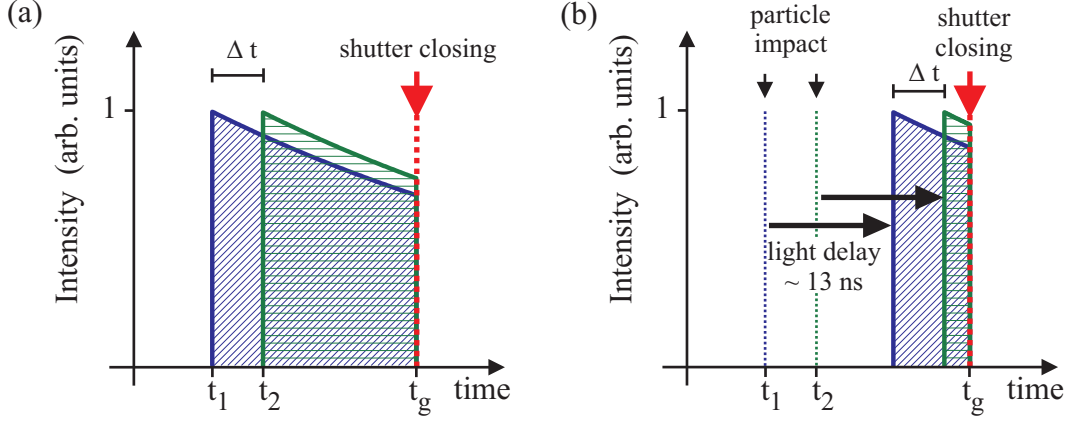
Figure 3.4: (a) The exponential decay of the light intensity is shown, which is emitted following the particle impact (t_1, t_2) and integrated by the gated camera until the optical shutter is closed at the gating time t_g. The comparison of the integrated intensities of each particle yields the impact time difference Δt. In (b) the light is delayed by the additional optical setup before it reaches the gated camera. This effectively shortens the gating time and improves the time resolution.

an electron cloud at its backside which is then further accelerated to the attached phosphor screen anode (P-47, $(Y_2SiO_5:Ce)$ [102], Hamamatsu$^{©}$) where it causes fluorescence light emission. The light intensity decays with a fast characteristic time constant ($\tau \approx 52$ ns) and is recorded by a two-camera system located outside the vacuum system. One of the CCD (Charge-Coupled Device) cameras facing the phosphor screen is equipped with a light-intensifier acting as a fast optical shutter. This camera is also called the *gated* camera in contrast to the second *non-gated* camera without the fast optical shutter.

The relative fragment distances at the detector are derived as follows. The transverse fragment distance is obtained from the relative positions of the particles' light spots observed by the non-gated camera. This is a common procedure for 2D imaging detectors and achieves a high spatial accuracy down to the sub-mm range depending on the camera setup and resolution. In the current experiment the transverse fragment distance was extracted from the light spot positions with a resolution of $< 100\mu$m.

The CCD averaging time interval of the camera enables the temporal integration over the complete exponential decay of the fluorescence light emitted following the particle impact at an arrival time t_i on the phosphor screen. However, at the *gated* camera the light integration of each light spot i is stopped already during the exponential decay by the closing of the optical shutter at a fixed gating time t_g ($t_g > t_i$) triggered by the first fragment on the MCP (Fig. 3.4(a)). Therefore, in the case that the gating time $t_g - t_i$ is

short compared to the decay constant τ, the integrated light intensity $I_{g,i}$ measured for each light spot i ($i = 1, 2$ for a two-fragment-breakup) by the gated camera depends on the arrival time of the fragment. Normalized by the corresponding, completely integrated light intensity of the non-gated camera $I_{n,i}$, the intensity ratio Ω_i for each light spot,

$$\Omega_i = \frac{1}{k(x,y)} \cdot \frac{I_{g,i}}{I_{n,i}} = 1 - e^{-(t_g - t_i)/\tau} \,, \tag{3.13}$$

[where $k(x,y)$ is a position dependent calibration (normalization) factor (see later paragraph)] yields the impact time difference Δt_i of particle $i > 1$ with respect to the first one,

$$\Delta t_i = t_i - t_1 = \tau \ln \frac{1 - \Omega_i}{1 - \Omega_1} \,. \tag{3.14}$$

Both the time and position measurement are independent of the number of particles and can easily be extended to the multi-particle fragmentation of polyatomic molecules as long as the fragments do not hit the same spot on the detector. Further details to the detector principle and the derivation of Eq.(3.14) can be found in [98, 99, 100].

Through the logarithmic dependence of the time difference Δt on the measured intensity ratio Ω, the time resolution is determined both by the interval of the gating time $t_g - t_i$ and the various noise contributions of the camera system, such as read out-, dark current- and shot noise.

An improvement of the resolution requires a suppression of the latter noise source by cooling of the camera system and diminishing the shot noise through an increase of the initial light input. Also a reduction of the gating time by the earlier closure of the optical shutter can achieve a better time resolution. However, since in DR studies at storage rings the arrival of an event is not known beforehand, the closure of the optical shutter can only be initiated by the impact of the first fragment at the earliest. Thus in practice the electronic processing and delay of the impact signal limits the earliest shutter closing, currently optimized for the 3D imaging detector to ≈ 20 ns. This corresponds to a time resolution of $\sigma_{\Delta t} \approx 1$ ns (standard deviation) [99].

For a further shortening of the gating time the camera setup was modified by adding an optical light path [99] for the images viewed by the gated camera (Fig. 3.5). While the closing time t_g of the shutter with respect to the impact of the first fragment on the MCP remains as before, the emitted light reaching the gated camera was delayed by the light path extension, yielding effectively shorter gated integration periods (Fig. 3.4(b)).

The requirements of a sufficient light delay at good image quality, which still allows to distinguish light spots from each other, resulted in an approximately 4 m long extension path with a parabolic mirror (ø $= 203$ mm; $f = 1016$ mm) as the main optical element.
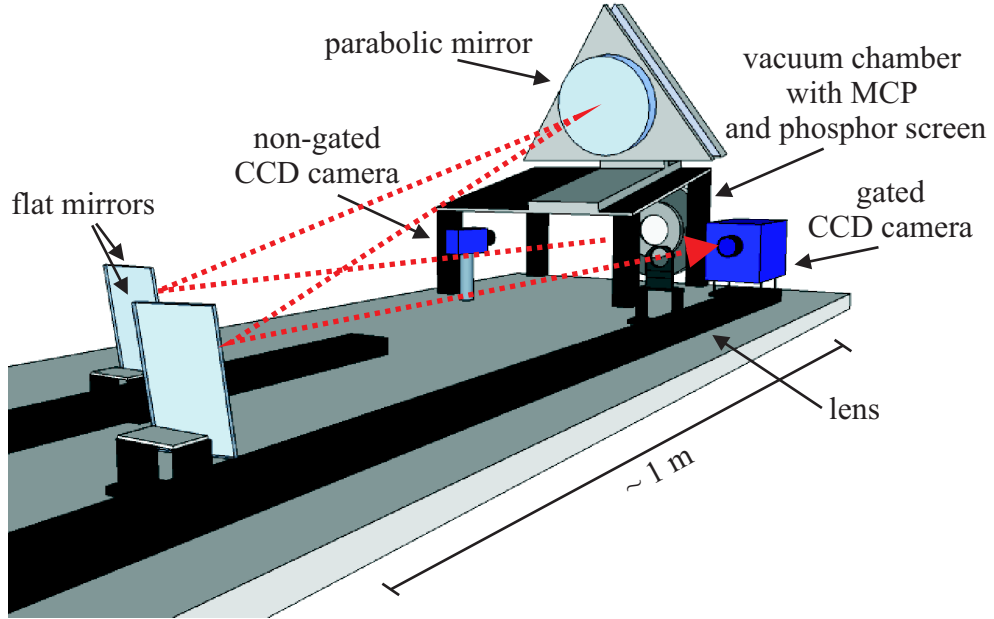
Figure 3.5: Schematic drawing of the light-path extension of the 3D imaging detector [99]. The main optical elements are a parabolic mirror, a lens and the camera's objective. Together they focus the image of the phosphor screen onto the CCD chip of the gated camera, while the non-gated camera faces directly the phosphor screen. To achieve a compact setup the light-path is folded by two flat mirrors.

Thereby the gated camera is kept close by the MCP and a lens is located at the image distance from the parabolic mirror to collect the reflected light onto the gated camera's objective. Finally two flat mirrors fold the light path in order to fit the whole setup in a 180 cm × 80 cm light-proof box. The variable distance of the parabolic mirror to the phosphor screen defines the magnification and consequently the fraction of the phosphor screen seen by the gated camera. Through the light path extension the effective gated integration period can be reduced by up to ≈ 13 ns, closing the optical shutter as soon as ≈ 7 ns after light of the first fragment has reached the gated camera. This has improved the time resolution by a factor of two, down to $\sigma_{\Delta t} \approx 0.5$ ns (standard deviation). In order to retain the good transverse distance resolution, the non-gated camera still views straightly the emitted light from fragment impacts.

Data acquisition

In DR fragment imaging experiments the experimental procedure for the TSR, i.e. the injection of the ion beam and the setting and changing of the electron beam velocities, is controlled independently of the imaging system (see e.g. [17, 94]). For the operation of the 3D fragment imaging detector a separate data acquisition software DaVis (**D**ata **a**cquisition by La**Vis**ion$^{©}$ [103]) is responsible, which controls the camera frame taking rate, the camera readout and the identification of light spots on the camera image. It has been mainly developed and provided by the camera manufacturer LaVision$^{©}$ but the C-type command language allows the user to modify and extend it to the specific needs.

Typically, particles at a rate of up to 1 kHz hit the detector and produce light spots on the phosphor screen. In contrast, camera frames are only acquired at a rate of about 30 s^{-1}; i.e. 10 ms exposure and $\approx$ 20 ms readout and processing. Consequently, since the particle beam cannot be interrupted, the light emission of any subsequent unwanted particle has to be prevented in order to ensure only fragments stemming from a single DR event in each camera frame. This is realized most efficiently by switching the phosphor screen voltage. Lowering the phosphor screen to the MCP potential is achieved within $\approx 2\,\mu$s and thus inhibits any light emission until the next camera frame. Typically the voltage of the MCP backside is set to 2.0 kV (front-side is set to ground potential) whereas the phosphor screen anode is operated at 5.2 kV.

The readout of the frames acquired simultaneously by both cameras is followed by an image-processing procedure searching for light spots above a minimum intensity threshold on the camera images. This fast peak finding routine determines the average light intensity within a rectangle of fixed size as well as the position of each identified light spot. Thereby the rectangle size has to cover the entire intensity distribution of the light spot. However, its size can be defined independently for each camera to adapt for the individual image quality which differs mainly due to the optical intensifier and the cameras' positions, and yields generally larger spot sizes in the gated camera. The individual adjustment of the rectangle size thus avoids that nearby fragments in the non-gated camera fall undistinguishable into one rectangle and enables the observation of smaller transverse distances in the non-gated camera of which in particular 2D imaging measurements benefit. The average intensities in each camera, normalized to correspond to the same rectangle area, are then used in the later analysis to calculate the impact time differences (Eq.(3.14)). From the intensity distribution of the camera pixel within the rectangle the exact fragment impact position is determined by the intensity weighted center-of-mass.

Finally the raw data of each camera, regardless of the number of identified light spots, are

stored together with possible additional frame information (elapsed time since injection, flag for cooling or detuning electron energy set at the electron target, CCD chip temperature, ...) in separate data files as functions of the camera frame number. Compared to the storage of the complete camera frames these initial online processing steps reduce efficiently the required disc space without loosing the essential information. The subsequent offline analysis of the raw data files is then performed with data analysis software, developed in ROOT$^{\textcircled{C}}$ [104] or MATLAB$^{\textcircled{C}}$. The principle procedure is briefly outlined in the following paragraphs.

Background elimination for 2-body breakups

At the beginning of the analysis of imaging data the recorded fragments from DR events, here mainly focusing on the breakup of diatomic molecules (for polyatomic molecules see e.g. [78]), have to be separated from background contributions. Background events can originate from various reactions of the stored ion beam in the ETS and may imitate a real breakup event on the phosphor screen. For example, collisions of the molecular ions with residual gas molecules are possible which mostly result in neutral and positively charged fragments. Similar products also evolve from electron induced dissociative excitation, where compared to DR the electron is set free after the breakup of the molecular ion. On the other hand, it is also possible that part of the DR fragments simply miss the detector or are not detected due to the limited MCP efficiency.

Mostly these false events can be sorted out easily by the number of particles recorded in each camera frame. For example, for the diatomic cases studied here only frames with two particles will pass, whereas all others are neglected. These conditions are even enhanced in 3D imaging measurements, since the same particle number is required in both cameras and the fast optical shutter suppresses more efficiently background events which may arrive within the $\approx 2\,\mu$s required for closing of the phosphor screen.

Nevertheless the restriction on the particle number alone may not be a sufficient criterion to eliminate all background events. Two background particles arriving in coincidence can imitate a diatomic breakup. Similarly, but even more unlikely, there is the chance of event mixing, i.e. at the simultaneous arrival of two or more dissociating molecules not all fragments are detected. This can produce two-, but even more likely three-particle events.

Further constraints are thus necessary to single out these background events arriving in coincidence from "good" events, where all fragments stem from the DR induced breakup of the same molecule. Partly this can be achieved in 3D imaging experiments by confining

the time difference between fragment impacts, which will be deduced from the measured intensities in the later part of the analysis. For example, the breakup kinematics of the hydrogen molecules studied under the present conditions do not separate the fragments by more than $\approx 3 - 4$ ns so that fragments $\gtrsim 5$ ns apart must originate from background events.

Another efficient procedure, applicable both in 2D and 3D Imaging, is the restriction on the transversal center-of-mass (c.m.) of the observed fragments. This has become possible due to the high quality ion beam preparation at the TSR. Within a short period of phase-space cooling the circulating ion beam reaches a low divergence (≤ 0.1 mrad root-mean-square (rms)) with small spatial extension projecting the c.m. positions of the individual events onto a small area of the detector (see Fig. 3.6(a)).

For the breakup of diatomic molecules with nuclei of identical masses (e.g. H_2^+) the c.m. is simply given by the center between the two fragment impact positions and is scattered statistically in a narrow range of the mean c.m., depending on the divergence and transversal extension of the ion beam. In contrast, for two particles of coincident background events the center position is distributed over the whole detector surface and can thus be distinguished from "good" events by the individual distance to the mean c.m.. As a measure of the quality of the individual c.m. location the transverse deviation Δ_{DEV} compares in horizontal and vertical direction the distance between the individual c.m. positions and the mean value ($\delta_{\bar{x}-x}$; $\delta_{\bar{y}-y}$) to the width of the total c.m. distribution (σ_x; σ_y). It describes an ellipse in the plane transverse to the beam direction :

$$|\Delta_{DEV}| = \sqrt{\left(\frac{\delta_{\bar{x}-x}}{\sigma_x}\right)^2 + \left(\frac{\delta_{\bar{y}-y}}{\sigma_y}\right)^2} . \tag{3.15}$$

Due to the normalization to the width of the c.m. distribution any restriction on Δ_{DEV} is independent of possible temporal variations of the ion beam's spatial extension which might occur in long time measurements. Coincident background events can thus be suppressed evenly and independent of the camera setup and the actual c.m. position through their transversal c.m. position by confining Δ_{DEV}.

From the c.m. distribution the relative background contribution can be evaluated (an example for the vertical direction is shown in Fig. 3.6(a)). Within a good approximation the shape is resembled by a double-Gaussian distribution (green line in Fig. 3.6(a)); a narrow Gaussian caused by the "good" events and a broad Gaussian offset originating from the background (red line). The relative background contribution is then computed by the ratio of the integrated offset in the limits defined by Δ_{DEV} and the sum over the total distribution in these limits. The data processed for the present work in the final
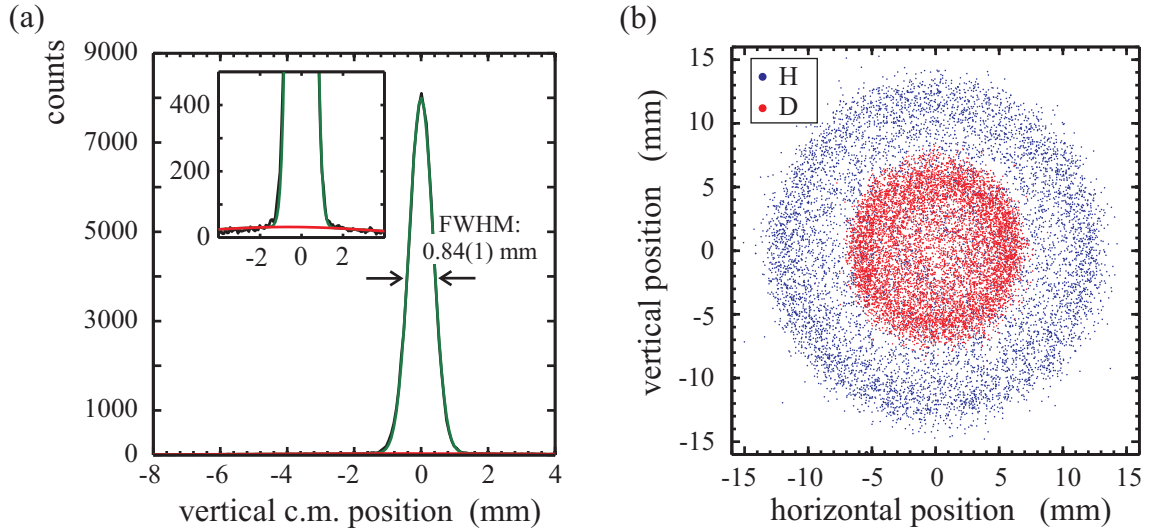
Figure 3.6: (a) The measured vertical c.m. distribution (black) is well described by a double Gaussian distribution (green line) of which one Gaussian represents the data and the second, broad Gaussian (red line) takes the background events into account. The inset shows an enlarged section of the total distribution, demonstrating the in general low background contribution in experiments with light molecular ions (HD^+, H_2^+). In (b) an accumulated image of the fragment impact positions of HD^+ DR events is shown. The fragment masses have been identified through their impact positions with respect to the c.m. (color code).

analysis generally comprised no more than 1 % "false" events at a transverse deviation limit of $|\Delta_{DEV}| \leq 1$.

Similarly for molecules with nuclei of different masses (e.g. HD^+) the transverse deviation may also serve as a constraint to sort out background events. However, the c.m. determination becomes less straightforward compared to the case with identical atomic constituents since the fragment masses cannot be assigned easily for a single event. Momentum conservation implies, on the other hand, that the heavier fragment is located closer to the c.m. proportional to the inverse mass ratio. For an ensemble of dissociating molecules the mean c.m. position can serve as a reference point compared to which masses of individual events are appointed and their c.m. determined. Since the mass identification depends both on the total c.m. distribution as well as on the single event the process runs iteratively, permuting if necessary the mass candidates until a stable condition of the mean c.m. is reached. In Fig. 3.6(b) the impact positions have been assigned to the fragments stemming from HD^+ DR events. Note, due to the doubled mass the circular impact area of the deuterium has roughly only half the radius compared to the one of the

hydrogen fragments.

Mapping of camera frames

In the next step of the analysis it has to be ensured that the corresponding fragments are recognized correctly in each camera and assigned to each other. This is essential for the time measurement which is based on the intensity ratio of a fragment's light spot recorded in the gated and non-gated camera. In practice, both cameras cannot be adjusted by hand with the required accuracy and focused onto the same part of the phosphor screen in order to automatically yield the correct assignment. Therefore the view of each camera has to be matched by a coordinate transformation which assigns the image of the gated camera to the same position seen by the non-gated camera. Considering not only horizontal or vertical shifts of the cameras with respect to each other, but also higher order relative image distortions, a single point on the gated camera (x_g, y_g) is related through a set of linear parameters $(\vec{a}, \vec{b})$ to the position on the non-gated camera (x_n, y_n):

$$
\begin{aligned}
x_n &= a_0 + a_1 \cdot x_g + a_2 \cdot y_g + a_3 \cdot x_g^2 + a_4 \cdot y_g^2 + a_5 \cdot x_g \cdot y_g \dots \\
y_n &= b_0 + b_1 \cdot x_g + b_2 \cdot y_g + b_3 \cdot x_g^2 + b_4 \cdot y_g^2 + b_5 \cdot x_g \cdot y_g \dots
\end{aligned}
\tag{3.16}
$$

Limiting the relation to a six-parameter description in $\vec{a}$ and $\vec{b}$, respectively, an ensemble of positions $(\vec{x}, \vec{y})$ is then described by two independent overdetermined sets of linear equations

$$
\begin{aligned}
\vec{x}_n &= A_g \cdot \vec{a} \\
\vec{y}_n &= A_g \cdot \vec{b}
\end{aligned}
\tag{3.17}
$$

where A_g is a matrix defined by the positions in the gated camera

$$
A_g = \left[\vec{1}, \vec{x}_g, \vec{y}_g, \vec{x}_g \cdot \vec{x}_g, \vec{y}_g \cdot \vec{y}_g, \vec{x}_g \cdot \vec{y}_g \right]
\tag{3.18}
$$

and which can be solved by an appropriate numerical method (see e.g. [105]) to yield the transformation parameters $(\vec{a}, \vec{b})$. Typically, single event frames are used to determine $(\vec{a}, \vec{b})$ before the transformation is applied to the data and particle positions in both cameras are compared to each other. In the case that a particle of a multi-fragment event in the gated camera cannot be mapped within a certain distance limit with any particle in the non-gated camera after permutation, the event is discarded. This might occur for example if the view of each camera only overlaps partly on the phosphor screen.

Finally, in order to obtain the relative fragment positions from the previously selected and processed data and study the fragmentation kinematics, it is necessary to transform and

calibrate the raw information. Therefore the transverse fragment positions are converted from pixel to meter and the measured intensity ratio is calibrated to deduce impact time differences in seconds. For the discussion of the details of the various procedures the following paragraph has been reserved.

Detector calibration

The detector calibration is an essential part in the analysis procedure and thus treated independently in this paragraph. It contains both the transformation of the recorded fragment positions into physical standard units as well as the position dependent calibration of the measured intensity ratios. The transformation parameters required for the various calibration processes are mostly retrieved in independent measurements either involving fragments stemming from an ion beam or an alpha source that has been mounted for that purpose about one meter in front of the MCP detector in the vacuum chamber.

In the so called *pixel-to-meter calibration* the fragment impact positions on the camera image (pixel) are transformed to the position on the detector (meter). Since the non-gated camera faces directly the phosphor screen it yields impact positions at higher resolution than the gated camera and is thus used to determine the transverse fragment distances. Therefore the pixel-to-meter calibration is only applied to the position information of the non-gated camera.

The pixel-to-meter transformation function is extracted in an independent measurement, where neutral particles from the ion beam impinge on the MCP detector. For that purpose a metal plate with 2 mm diameter holes is aligned parallel a few millimeter in front of the MCP, where its position selectively prevents the impact of the particles. The holes are arranged on a rectangular grid, horizontally and vertically 10 mm apart. Averaging over a large number of events the center position of each hole is projected onto the MCP detector and observed on the camera image. The recorded positions can then be related through a transformation to the known relative location on the phosphor screen. Thereby the functional dependence is similarly described as the mapping of the gated and non-gated camera images in Eq.(3.17), considering also higher order effects due to the tilting angle and image distortion of the non-gated camera. Estimations have shown that by far the transformation gives the largest error contribution to the spatial resolution, yielding ≈ 40 μm (FWHM) for the transformation of a single position; in contrast the position determination of a light spot from its intensity distribution can be neglected at typical spot sizes of 5×5 pixel^2.

The calibration of the measured intensity ratio is twofold: on the one hand it is essential

for the time measurement that the normalization constant $k(x,y)$ (see Eq.(3.13)) is determined as a function of the position (x,y) on the phosphor screen, on the other hand the impact time difference yields from the intensity ratios only if the light decay constant τ is known accurately.

The decay constant τ is characteristic for the MCP-phosphor screen assembly and is determined in an independent measurement. In this process alpha particles from a ^{210}Po emitter (185 MBq; E_α=5.3 MeV) initiate the closing of the optical shutter with variable delay so that the intensity ratio is recorded as a function of the gating time and the decay constant τ (=52.0 $\pm$ 0.5 ns) can be retrieved from the functional dependence. For the details of the measurement the reader is referred to [98].

The *position dependent calibration of the intensity ratio* aims at the compensation of variations in the measured intensities due to the cameras' sensitivity and setup. Thus a detailed procedure has been prepared which comprises several calibration steps applied between the acquisition of the camera image and the subsequent analysis of the raw data:

1. Dark image subtraction and flat-field correction of the raw images.

2. Matching the light sensitivity of each camera to one another.

3. Correcting variations of the intensity ratio correlated to the particle impact rate.

The calibration procedure starts directly after the readout of the raw images. Here, the pixel dependent thermal dark current is first corrected by the subtraction of a dark image. This is an average image of several (50) exposures taken before the measurement with a closed optical input, i.e. the phosphor screen remains dark, but the same exposure time (10 ms). In addition, the influence of time-dependent thermal changes on the dark current is taken into account by subtracting an intensity value, which is sampled in a dark part of each image. This also compensates an offset that was artificially added to the raw image intensity to avoid negative intensity values.

The light sensitivity of each pixel in the CCD camera and the possible disturbance of the light path through impurities on the objective is taken care of by a flat-field correction. The flat-field correction image is acquired by illuminating each camera equally to about 50-75 % of the saturation value (details can be found in [99]). In the actual correction step the intensity of the current frame is divided pixelwise after the dark current subtraction by the corresponding intensity value of the flat-field image and multiplied by the average intensity of the flat-field.

For the current camera setup the flat-field correction image can practically only be acquired independently for the individual cameras and thus not be used to match the sen-
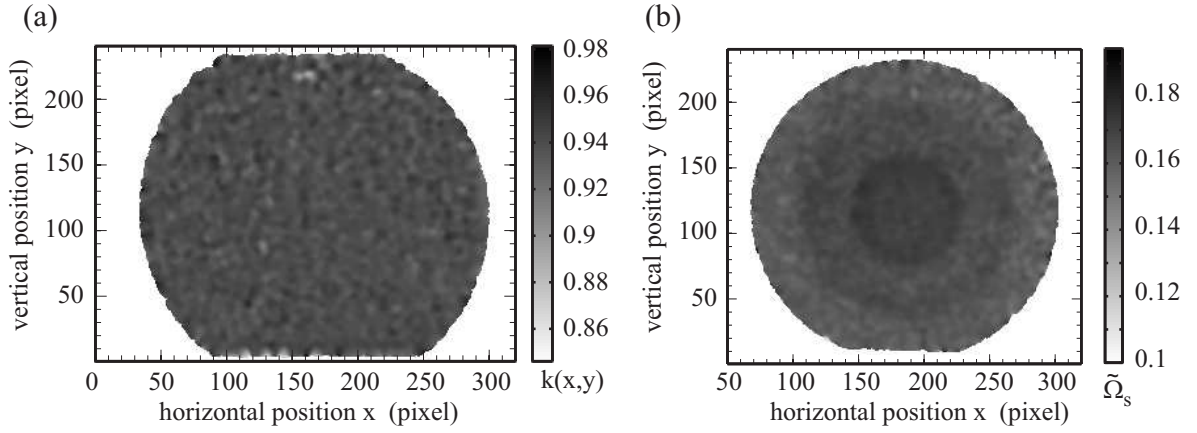
Figure 3.7: The position dependent correction factor $k(x, y)$ used to adjust the relative camera sensitivities is shown in (a). The distribution in (b) represents the calibrated intensity ratio $\tilde{\Omega}_s$ of single particle frames stemming from background events. Note, that the intensity ratio still possesses a position dependence which is closely correlated to the local particle rate on the phosphor screen (compare with Fig. 3.6(b)).

sitivity between the cameras on a pixel-wise scale. Therefore in the next calibration step the light intensity emitted from the phosphor screen and observed by each camera is compared. Since the phosphor screen cannot be illuminated completely, light spots from particle impacts are analyzed. Preferentially one uses single particles from residual gas collisions of the ion beam while the electron beam in the ETS is switched off to achieve equally distributed events. During these measurements the optical shutter remains open to integrate the complete light emission also by the gated camera. The relative camera sensitivity is then reflected by the deviation of the intensity ratio from a value of 1 and yields a position dependent correction factor $k(x, y)$ [98]:

$$k(x, y) = \frac{I_g(t_g \to \infty)}{I_n} \ . \tag{3.19}$$

The properly smoothed factor $k(x, y)$ avoids statistical artifacts and is shown for one of the performed measurements in Fig. 3.7(a). This correction factor is applied in Eq.(3.13) for a fragment impact at a specific position (x, y) to finally match the sensitivities between both cameras.

In the last step a position dependence of the intensity ratio has to be compensated which appears during DR measurements despite the previously described and applied calibration procedures and is thereby closely correlated to the local particle impact rate. In particular, measurements are affected where due to momentum conservation the breakup of a heteronuclear molecule leads to non-equally distributed fragments on the phosphor

screen. This effect is also observed for the calibrated intensity ratio of single particle frames which are labeled as background events along DR measurements. Their intensity ratios deviate from a flat position distribution in regions coinciding with the preferred particle impact locations (compare Fig. 3.7(b) and Fig. 3.6(b)). Consequently, the deduced time information can be distorted and the data may suggest strong, anisotropic and non-physical fragmentation geometries when omitting the compensation.

Currently the reason for this effect is not known. Since both the measured intensity ratio of single and multi-fragment events are influenced, a possible physical explanation due to the breakup dynamics of the molecule is excluded. The most probable reason must thus be a detector property which is revealed by the local increase of the particle impact rate and leads to a position dependent effect. Good candidates are a long decay constant of the emitted light intensity, influencing the recorded intensity of subsequent events at overlapping positions, or a position dependent change of the phosphor emission characteristics due to the higher particle rate. Conceivable might also be that the impact energy of the heavier fragments changes the properties of the phosphor screen through the number of emitted electrons from the MCP, as these fragments are generally confined due to momentum conservation on a smaller area of the detector.

However, a long decay constant of the order of $\approx 5 - 10$ ms, which was proposed above to explain this effect, is so far neither known to literature nor identified in first preliminary tests for both the P47 screen and the P43 screen located in the image intensifier (for details of the image intensifier see [98]). Most other reasons can also be argued to drop out or have been followed in independent studies where they appeared to be negligible. For example, a position dependence of the electronic trigger initiating the closing of the optical shutter will always affect all fragments in the same frame and cancels in the determination of the impact time differences. Also, the closing of the light path through the optical shutter was found to vary as a function of the position only by $\lesssim 30$ ps, which is not enough to explain the observed effects. Therefore only the local change of the light emission properties due to the particle impact rate or energy remain as possible causes but have so far not been studied specifically.

Nevertheless, the induced variations of the intensity ratio can efficiently be compensated. This is achieved by using the information on the intensity ratio of single particle frames labeled as background events during the two-fragment breakup measurements. Thereby one assumes that these events exhibit the same effects on the intensity ratio as the two-particle frames neglecting any position dependent fluctuations of the shutter closing signal. The intensity ratio of the single particle frames $\tilde{\Omega}_s(x, y)$, calibrated according to the previously described procedures and smoothed to avoid statistical artifacts, is shown as

a function of the position on the gated camera image in Fig. 3.7(b). Averaged by their mean value $\langle \tilde{\Omega}_s \rangle$, they can be applied as an additional position dependent correction factor on the calibrated intensity ratios $\Omega_{cal,i}$ of the individual fragments stemming from DR breakup events:

$$\Omega_i(x, y) = \frac{\Omega_{cal,i}(x, y)}{\tilde{\Omega}_s(x, y)} \cdot \langle \tilde{\Omega}_s \rangle . \tag{3.20}$$

A similar correction method, based on the idea of using the information from the recorded single particle, was developed in parallel [83]. Therein the calibrated intensity ratio Ω_1 of a single particle can be transformed according to Eq.(3.13) to the gating time

$$t_g(x, y) = -\tau \ln (1 - \Omega_1) . \tag{3.21}$$

as the particle impact itself initiates the closing of the shutter, i.e. $t_1 = 0$. After smoothing, the position dependent value $t_g(x, y)$ is used to correct the time difference between two fragment impacts:

$$\Delta t = t_2 - t_1 = \tau \ln \frac{1 - \Omega_2}{1 - \Omega_1} + t_g(x, y)_1 - t_g(x, y)_2 . \tag{3.22}$$

Both methods have shown to successfully compensate the effects on the measured intensity ratio correlated to the particle rate. Here, the first procedure is chosen and has been applied to the data.

Product kinematics at resonances of HD$^+$ DR

The hydrogen molecular ion has been favored due to its simple structure in numerous experimental and theoretical studies on DR research and offers in particular at low electron collision energies a unique possibility to focus on its fragmentation kinematics as depicted earlier in Sec. 2.3.

In this chapter experiments on the deuterated species HD$^+$ using the twin-merged-beam setup (Sec. 3.3.1) combined with the fragment imaging technique (Sec. 3.2) are presented, whereas the infrared *inactive* relative H$_2^+$ is treated in the subsequent chapter 5. Provided by the high experimental resolution rotational state contributions from initial HD$^+$ rotational levels in the recorded DR events could be followed by probing the DR process at selected low collision energies between ∼10 meV and ∼80 meV (Sec. 4.2.1). On the same narrow energy grid also the fragment angular distributions are studied (Sec. 4.2.2). They are compared to current theoretical models in the final section of this chapter (Sec. 4.3) in order to extract information on the electronic symmetries participating in the fragmentation process.

4.1 Controlled ion beam experiments

The studies of the fragmentation dynamics at low electron collision energies in the range of only a few tens of meV set high demands on the preparation of the ion beam prior to the induced breakup and require well directed electrons at stabilized collision energies.

Therein, the main limitations on the energy resolution are generally the thermal electron velocity spread and sustaining the stability of the ion beam energy after completion of the phase-space cooling. In particular at low electron detuning velocities v_d, close to the ion beam velocity v_i, electrons can effectively accelerate or decelerate the ions through *dragging* forces and thus shifting the actual detuning energy E_d away from the one adjusted.
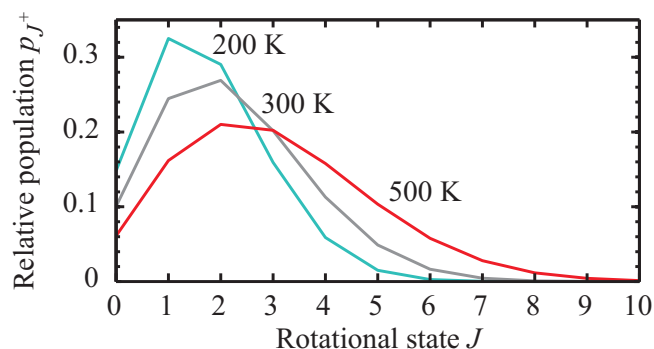
Figure 4.1: Relative populations p_{J^+} for Boltzmann distributed rotational states of HD$^+$ at 200 K, 300 K and 500 K.

In the case that only one electron beam is available this effect can partly be compensated by setting the electron beam velocities for tens of ms from the detuning back to the velocity matching value in order to maintain the ion beam energy stabilized through intermediate phase-space cooling. This is a common procedure applied in event-by-event counting experiments at storage rings. In fragment imaging experiments, on the other hand, this method is generally less preferred as it reduces the effective data taking rate on top of the slower event acquisition of the detection system. A second merged electron beam can be used here in order to define constantly the ion beam velocity and to realize fragment imaging down to low detuning energies for long continuous time periods of the order of several seconds.

At the TSR the twin-merged-beam setup (Sec. 3.3.1) offers the possibility to co-propagate independently two electron beams with the stored ions; i.e. utilizing the electron cooler to define precisely through the constant acceleration voltage the ion beam velocity while simultaneously the electrons produced either by a thermal- or photocathode source in the electron target are set to selected detuning energies E_d probing the DR process. Possible effects due to beam dragging have been thoroughly studied for this twin-electron-beam arrangement in experiments with highly charged ions ($^{19}F^{6+}$) described in [92]. Therein the competition of the dragging forces induced by either electron beam was found to be mostly suppressed by increasing the relative strength of the electron beam defining the ion velocity, i.e. through a higher electron density. For the experiments involving electrons emitted from the photocathode this is automatically satisfied since here electron beams are typically generated with a density reduced by a factor of ~ 10 compared to the electron cooler. In the current measurements the change of the ion velocity due to dragging forces are thus expected to be reduced to a negligible level (~ 0.3 meV) once the detuning energy exceeds $E_d \geq 0.5$ meV as discussed by [17].

Besides a good control of the ion beam and the electron collision energies, the storage-ring experiments largely profit from the availability of molecular ions in well known initial

Table 4.1: The electron beam conditions for the HD$^+$ measurements at 1.44 MeV ion beam energy. Listed are the electron densities n$_e$ and currents I$_e$ for given expansion ratios α_{target} and electron sources as well as the electron cooler beam density n$_{e,cooler}$.

Label	Electron source	n$_{e,target}$ (cm^{-3})	I$_{e,target}$ (μA)	α_{target}	n$_{e,cooler}$ (cm^{-3})
PC$_L$	photocathode	$(0.62\pm0.02)\times10^6$	203 ± 6	30	1.6×10^7
PC$_H$	photocathode	$(1.27\pm0.02)\times10^6$	415 ± 7	30	1.6×10^7
TC	thermal cathode	$(2.86\pm0.03)\times10^6$	353 ± 4	40	1.6×10^7

internal states. The HD$^+$ ions produced for the experiments through electron impact ionization of neutral HD gas in a standard Penning ion source generally exhibit high initial ro-vibrational excitations (see also Sec. 5.1.1), impeding state selective experiments and thus direct comparisons to theory. However, possessing a permanent dipole moment the HD$^+$ ion is infrared active and thus cools down radiatively. Within only hundreds of milliseconds the ions arrive through radiative interaction in the vibrational ground state [10, 80] with only negligible population in excited states and reach an equilibrium rotational state distribution mainly determined by the surrounding room temperature after a few seconds [63]. Thus, by the time the phase-space cooling process of the stored ions is completed ($\sim$ 1 s) only a handful of rotational states ($J^+ \lesssim 6$) in the ground vibrational state are populated, simplifying the analysis and the later comparison to theory. Figure 4.1 illustrates that for a Boltzmann distribution at 300 K, only rotational states $J^+ \leq 4$ are populated by more than 10 %.

These considerations have been taken into account to set up the measurement scheme scanning the fragmentation kinematics of DR induced HD$^+$ breakup events at selected detuning energies (see also [18, 19]). After each injection the molecular ions are stored for $\sim$ 20 s. During the initial 7 s of the total storage time period electrons at velocity-matching values are merged in both the electron cooler and the electron target to phase-space cool the circulating ion beam. The electron-ion collision energies thereby amount to the electron beam thermal energies. The electron beam emitted by the photocathode in the electron target is then detuned to the desired electron collision energies for 7-17 s from injection before it returns to the velocity matching value in the final 3 s. Taking advantage of the twin-merged-beam arrangement the electron cooler beam remains at cooling velocity throughout the whole storage time, thereby constantly defining and stabilizing the ion beam energy.

The initial 7 s precooling period is, on the one hand, sufficient to complete phase-space

cooling of the ion beam and, on the other hand, allows the internal excitations to reach an equilibrium distribution (discussed in Sec. 4.2.1). Common conditions can thus be ensured before the measurements at detuning energies are started. Moreover reference imaging measurements at the end of the initial 7 s and during the last 3 s are acquired, probing the rotational state distribution of the ions through DR at zero detuning energy. The first rotational probe is used to confirm that the same equilibrium state distribution for all measurements is reached before the electron target is detuned, whereas the final reference measurement determines possible rotational excitations by electrons at non-zero collision energy (Sec. 4.2.1).

Some measurements have been performed with an electron beam generated by the thermal cathode in the electron target (see also [106]). In those cases the total storage time was 15 s and the electron target could be operated continuously at detuning energies without affecting the ion beam quality. It should be noted here, that for comparisons to the data acquired with the photocathode, only events after 7 s storage time were used. A summary of the measurement conditions is given in Table 4.1.

4.2 Experimental results

The DR events observed on the detector are determined at a selected electron detuning energy E_d by the total DR rate $\alpha_{DR}(E_d)$ comprising all accessible initial-to-final-state DR channels. For studies on HD$^+$, where the vibrational cooling to the ground state is completed by the time the measurement starts, only initial *rotational* state contributions have to be considered, which access at low electron energies ($E_d \lesssim 1.14$ eV) one final fragment state configuration [55] ([H(n) + D(n')] or [H(n') + D(n)] with $n = 1$ and $n' = 2$ only; see Sec. 2.3). Therefore the observed total DR rate $\alpha_{DR}(E_d, t)$ represents a superposition of the rotational contributions according to their relative populations $p_{J^+}(t)$ in the stored ions at a certain time t after the injection and the respective state specific DR rates $\alpha_{DR}^{(v^+=0,J^+,n=1,n'=2)}(E_d)$

$$\alpha_{DR}(E_d, t) = \sum_{J^+} p_{J^+}(t) \, \alpha_{DR}^{(v^+=0,J^+,n=1,n'=2)}(E_d) \, . \tag{4.1}$$

The rotationally averaged DR rate coefficient $\alpha_{DR}(E_d)$ has been measured previously with high resolution in independent event-by-event counting experiments [13, 17] and consistently reported large variations at low electron collision energies superimposed on the general inverse energy dependence ($\alpha_{DR} \propto E_d^{-1/2}$) of the direct DR process (see Fig. 2.4 in Sec 2.3).

Measurement of DR rate coefficient

The DR rate coefficient $\alpha_{DR}(E_d)$ has also been obtained under the current experimental conditions (corresponding to those listed under PC_H in Table 4.1), utilizing the energy-sensitive solid state detector downstream of the electron target and following the general scheme common in DR rate measurements at the TSR. The measurement scheme comprises fast switching of the electron velocity between the selected detuning, a defined reference and possibly the velocity-matching value in order to enforce continuous phase-space cooling of the stored ions. Each consecutive step typically lasts for only a few tens of milliseconds depending on the aim of the experiment. While the count rate recorded at the detuning energy yields the DR rate, the count rate associated with the reference electron collision energy is used for a relative normalization to the number of stored ions. This is usually necessary since the typical ion currents are too low to be simultaneously measured accurately by the diagnostic tools in the TSR. The measured rate coefficient is finally corrected for possible background events as well as contributions stemming from the toroidal part of the electron target. Latter events arise from the merging of the electron beam with the ion beam, which impose electron-ion collision energies deviating from the adjusted detuning energy E_d in the collinear section. Depending on the DR cross section they can lead to additional count rates at the adjusted detuning energy E_d and have to be corrected in an iterative analysis procedure [107]. Further details of the complete analysis procedure can be found in the PhD thesis by H. Buhr [17].

The obtained DR rate coefficient $\alpha_{DR}(E_d)$ is shown for incident electron energies $E_d \leq 80$ meV in Fig. 4.2 and resolves a rich narrow structure down to meV electron collision energies, consistent with previous measurements (compare to Fig. 2.4 in Sec 2.3). The patterns, associated with the formation of ro-vibrational Rydberg resonances through non-adiabatic couplings between the initial HD^+ ion state and the colliding electron, are found to mostly reduce the total DR rate, remaining below the one calculated for the direct process (dashed line in the figure). Scaling the measured DR rate coefficient $\alpha_{DR}(E_d)$ by the square root of the electron collision energy E_d, avoids the representation of the superimposed $1/\sqrt{E_d}$-dependence attributed to the direct process. In fact, the scaled DR rate $\tilde{\alpha}_{DR}(E_d)$ $(= \alpha_{DR}(E_d) \cdot \sqrt{E_d})$ particularly pronounces the narrow resonant structures and is thus favored in the following.

The present studies approach the low-energy range from a different observational point of view, focusing on the fragmentation kinematics. In measurements using fragment imaging the initial ionic HD^+ states associated with the resonances can be inferred from the obtained kinetic energy release (KER). Moreover, this technique enables to analyze
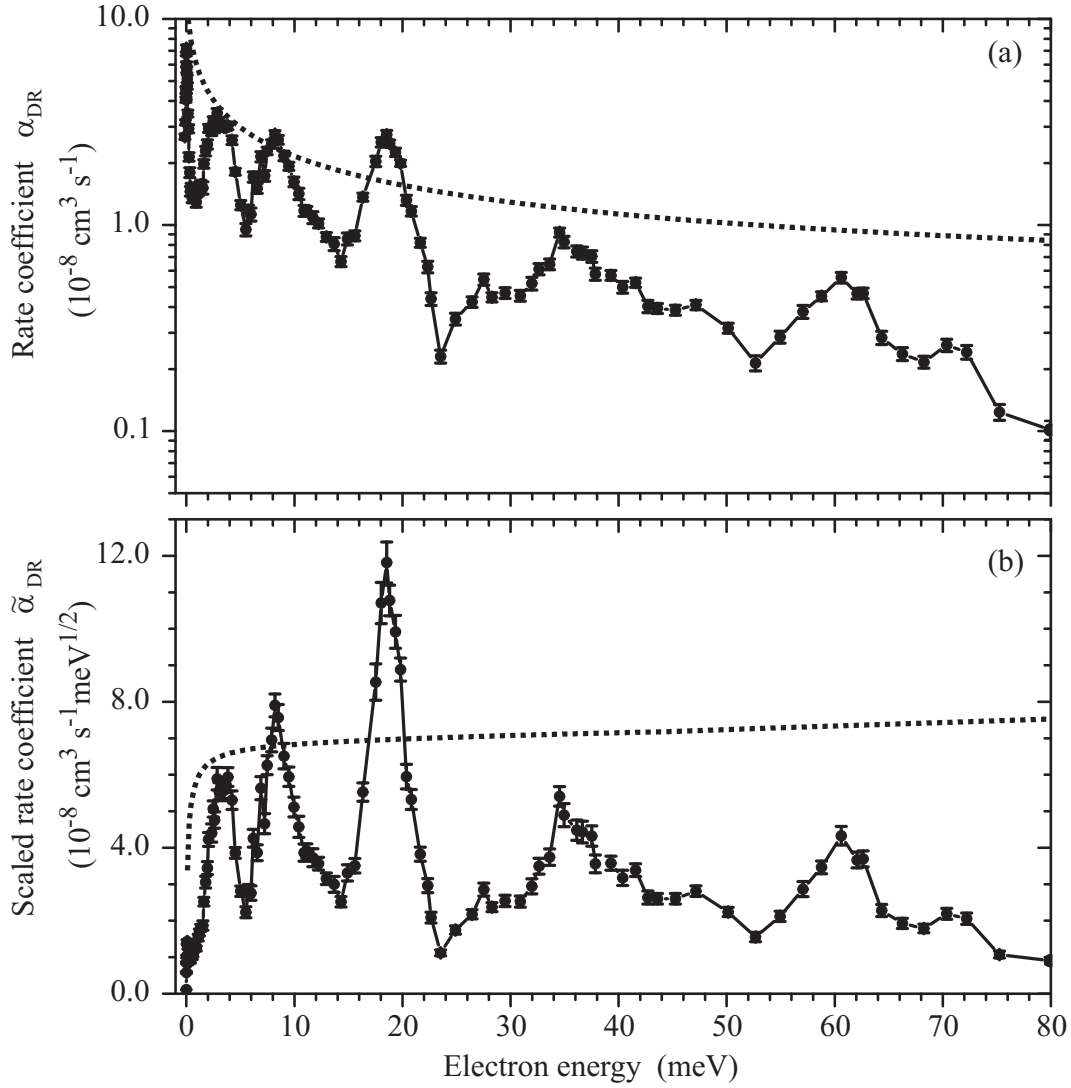
Figure 4.2: (a) The rotationally averaged DR rate coefficient $\alpha_{DR}(E_d)$ and (b) the scaled, rotationally averaged DR rate coefficient $\tilde{\alpha}_{DR}(E_d)$ $(= \alpha_{DR}(E_d) \cdot \sqrt{E_d})$ are plotted as functions of the electron detuning energy E_d. The data were acquired with the photocathode electron source and the parameters listed under PC$_H$ in Table 4.1. The dotted lines correspond to the direct DR rate coefficient.

the fragment angular distributions at the selected energies and provide insights to the coupled electronic symmetries necessary to yield the complete picture on the ongoing dynamics of the resonant electron capture process.

Both the KER as well as the fragment angular distributions are obtained on a narrow grid of collision energies in the vicinity of the resonant patterns reaching up to ∼80 meV. For the quantitative analysis of the fragment imaging data the transverse distance information is preferred instead of the complete 3D data which would determine directly the KER and the fragment angular distribution. However, at the applied high ion beam velocities the impact time differences are too small compared to the time resolution to yield information at similar quality as the transverse distance spectra.

4.2.1 Rotational state contributions to the DR rate

Within the first second after injection the internal excitations of the stored ions decay to rotational levels mainly of the vibrational ground state and determine together with the precisely known relative electron collision energy and the single final fragment excitations the KER available to the escaping neutral DR products.

Consequently, for the different amounts of the measured KER only rotational state contributions can be responsible and thus have to be considered. The total normalized distance distribution $F(D)$ (Eq.(3.10)) is then described by

$$F(D) = \sum_{J^+} b_{J^+} \sum_l a_l \, F_{l,J^+}(D) \tag{4.2}$$

with $a_0 = 1$ and relative rotational state contributions b_{J^+} $(= b_{(v^+=0,J^+,n=1,n'=2)})$,

$$b_{J^+} = \frac{p_{J^+} \cdot \alpha_{DR}^{(J^+)}}{\sum_{J^+} p_{J^+} \cdot \alpha_{DR}^{(J^+)}} \tag{4.3}$$

which are proportional to the relative population p_{J^+} as well as the state specific DR rate coefficient $\alpha_{DR}^{(J^+)}$ of the initial HD^+ ion rotational state J^+. The small rotational energy differences resulting from the rotational constant $B_{v^+=0} = 2.72$ meV [108] restrict the analysis to obtain only rotationally averaged angular distributions, that is Legendre coefficients a_l of order l (see Eq.(3.9)) independent of the rotational state J^+. Both parameters b_{J^+} and a_l are deduced from a least-squares fit to the transverse distance data after the normalized distance distribution $F(D)$ has been scaled to the number of counts N_0 of the data set, yielding $\tilde{F}(D) = N_0 \cdot F(D)$.

In the first analysis step, following the ideas presented in [80], constant, J^+-independent DR rate coefficients are assumed ($\alpha_{DR}^{(J^+)} = 1$) and the rotational populations are related

Table 4.2: The kinetic energy release (KER) for $E_d = 0$ eV DR of HD$^+$ is listed for ions in the first 8 rotational levels of the vibrational ground state. They are compared to the associated maximum transverse fragment distance of a dissociation event from the center of the electron target ($E_{beam} = 1.44$ MeV).

Rotational state J^+	Kinetic energy release (eV)	Maximum distance D (mm)
0	0.730	18.49
1	0.735	18.56
2	0.746	19.69
3	0.763	18.90
4	0.784	19.16
5	0.812	19.49
6	0.844	19.88
7	0.882	20.33

to each other through a Boltzmann distribution

$$p_{J^+} = (2J^+ + 1)\, e^{-\dfrac{J^+(J^+ + 1)B_{v^+=0}}{kT}} \tag{4.4}$$

where k represents the Boltzmann constant. Consequently the number of free parameters reduces and only an effective rotational temperature T is extracted from the fit as a measure of the rotational weighting factors b_{J^+}.

In the second step, the rotational contributions b_{J^+} are fitted independently with the exception of those of the lowest two levels, $J^+ = 0$ and 1. Their individual contributions to the transverse distance distribution are due to the small energy difference undistinguishable at the present transverse distance resolution of $\approx 100\ \mu$m (compare in Table 4.2) and therefore forced in the fit to $b_0 = b_1 = b_{01}/2$. For the recorded DR events this yields rotational weighting factors b_{01} characterizing the lowest two rotational state fractions.

Limitations in the rotational state analysis

The computation of the model functions $F_{l,J^+}(D)$ used in $F(D)$ (see Eqs.(3.10) and (4.2) as well Appendix A) assumes the probability for dissociation events to be independent of the position in the electron target as well as the electron detuning energy given by E_d.
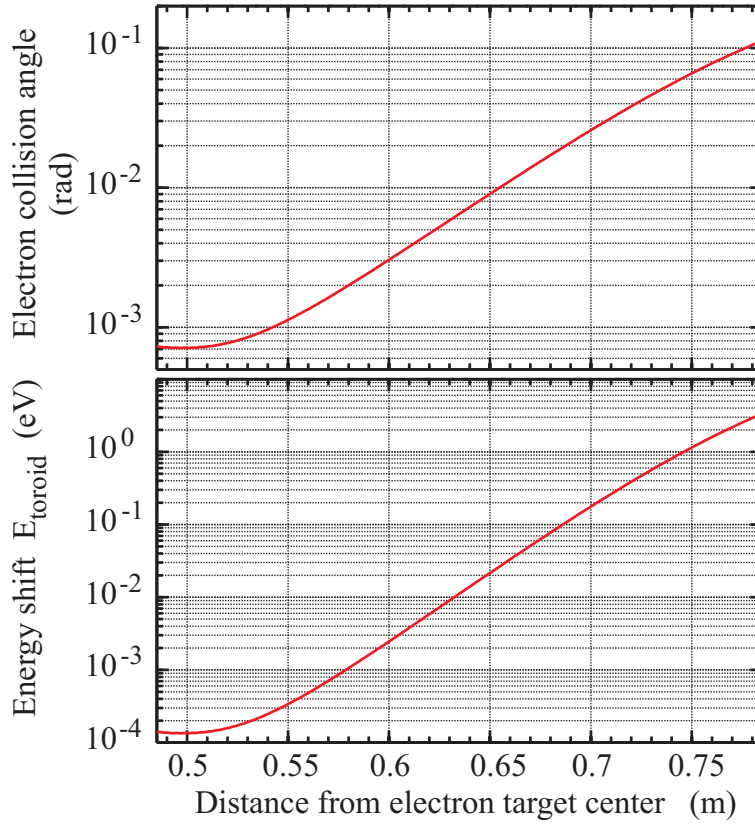
Figure 4.3: (a) The electron collision angle in the toroidal magnetic field is plotted as a function of the distance to the center of the electron target interaction section [92]. Here, the merging of the electron beam adds an energy shift E_{toroid} to the electron detuning energy E_d as shown in (b).

However, the merging of the electrons in the toroids at each end of the straight interaction section in the electron target causes deviations from this ideal assumption [92]. The non-vanishing angle under which the electrons approach the ion beam (Fig. 4.3(a)) in these parts results in an increased effective electron collision energy $E_d + E_{toroid}$, which deviates by E_{toroid} from the adjusted detuning energy E_d in the straight section (Fig. 4.3(b)). Hence, within the thermal electron velocity spread the implied parallel overlap is only valid in the collinear, central interaction section yielding DR events at detuning energy E_d. Events stemming from the toroidal sections are induced by an electron with collision energy $E_d + E_{toroid}$ and contribute according to the DR cross section. Their total KER exceeds the one expected from the adjusted detuning energy E_d and can thus be misinterpreted in the rotational state analysis. These effects are taken into account in the computed model functions by considering an effective overlap length L, greater than the nominal length of the straight interaction section.

In the analysis of the measurements on HD^+ the effective overlap length L is set to $L = 1.30 \pm 0.05$ m which imposes an additional systematic error on the deduced rotational state fractions. The uncertainty on the deduced temperature T is estimated to be $\pm$ 30 K and requires according consideration in the extraction of the individual rotational state
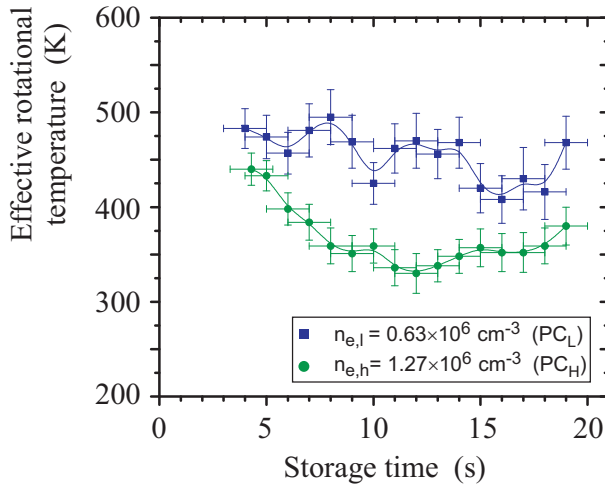
Figure 4.4: Effective rotational temperature deduced from $E_d = 0$ eV DR events as function of the storage time for the different measurement conditions listed as PC$_L$ (photo cathode; low electron density) and PC$_H$ (photo cathode; higher electron density) in Table 4.1 (lines to guide the eye).

fractions b_{J^+}. The deduced fragment angular distributions, on the other hand, depend less sensitive on the actual electron beam overlap as they are obtained from the total shape of the transverse distance distribution (see Sec. 4.2.2).

Rotational cooling and probing by zero energy electron collisions

Employing the high energy resolution of the experimental setup, the rotational state population of stored ions can be monitored through DR induced breakup events in fragment imaging measurements. Although the rotational state fractions inferred from the transverse distance distribution are proportional to both the rotational population and the J^+-dependent DR rate coefficients (Eq.(4.3)), measurements at the same electron detuning energy E_d can only differ by the J^+-distribution of the stored ions. Rotational state populations can thus be compared which enables to follow the time dependence of rotational cooling towards an equilibrium distribution. In the present work this tool has been utilized for reference measurements probing the J^+-contributions with velocity-matched electrons.

In Fig. 4.4 the measured effective temperatures T are shown as a function of the storage time. They were obtained from the transverse distance distributions by operating both electron cooler and target at zero detuning energy. Within the first ~ 7 s T decreases and approaches a nearly constant value, indicating that the stored ions have reached an equilibrium excitation. The time dependence as well as the asymptotic temperature level strongly depend on the electron beam density and are thus not consistent with a model based on radiative internal transitions only.

A complete description of the observed rotational time dependence requires destructive and non-destructive interactions with electrons besides radiative transitions. These addi-

tional processes have recently been reported to play an important role in the rotational decay of stored HD^+ ions merged with an electron beam at the TSR [109]. In the modeling described in [109] non-destructive inelastic and super-elastic collisions (SEC) which increase or decrease, respectively, the internal ro-vibrational excitations (v^+, J^+)

$$HD^+(v^+, J^+) + e^-(E) \rightarrow HD^+(v', J') + e^-(E') \tag{4.5}$$

were required apart from depletion of selected rotational states through J^+-dependent DR rate coefficients. Inelastic collisions $(E' < E)$ thereby impose an heating process onto the circulating ions once the electrons are detuned from the velocity matching value, that is in DR measurements at non-zero collision energies or in the toroidal sections of the electron cooler and target where the electron beam is merged. Super-elastic collisions $(E' > E)$, on the other hand, cool the internal excitations of the molecular ions and have so far only been reported to efficiently decrease the vibrational quantum numbers (e.g. [11, 110, 111, 112]). The studies presented in [109] give first experimental evidence for rotational SEC and are supported by the electron density dependent rotational cooling observed in the current experiments.

A detailed model is not computed at this point for the presented data in Fig. 4.4 since the purpose of these measurements is mainly to demonstrate the ability to probe the rotational state populations which allows to determine the required time in order to reach an equilibrium internal excitation.

Energy dependent rotational state contributions

DR events from collisions with velocity-matched electrons, as presented in the previous paragraph, allow to trace the rotational excitation of the stored ions towards an equilibrium distribution. In the current experiments this has ensured that scans of the fragmentation kinematics at non-zero detuning energies can be performed starting from the same initial rotational population of the ions.

The effective rotational temperatures T are deduced from the transverse distance distributions between 7 s and 17 s and displayed in Fig. 4.5(b) as a function of the detuning energy below ~ 80 meV [19]. They are found to vary strongly with energy on a similarly narrow scale as the scaled DR rate coefficient $\tilde{\alpha}(E_d)$ (Fig. 4.5(a)) and mostly deviate from the average effective temperature T probed in reference measurements at zero electron energy between 6.5 s and 7 s (shaded bars in Fig. 4.5(b) for the measurements at low and high electron density, respectively), i.e. at the end of the combined electron cooling and before the electron velocity is detuned.
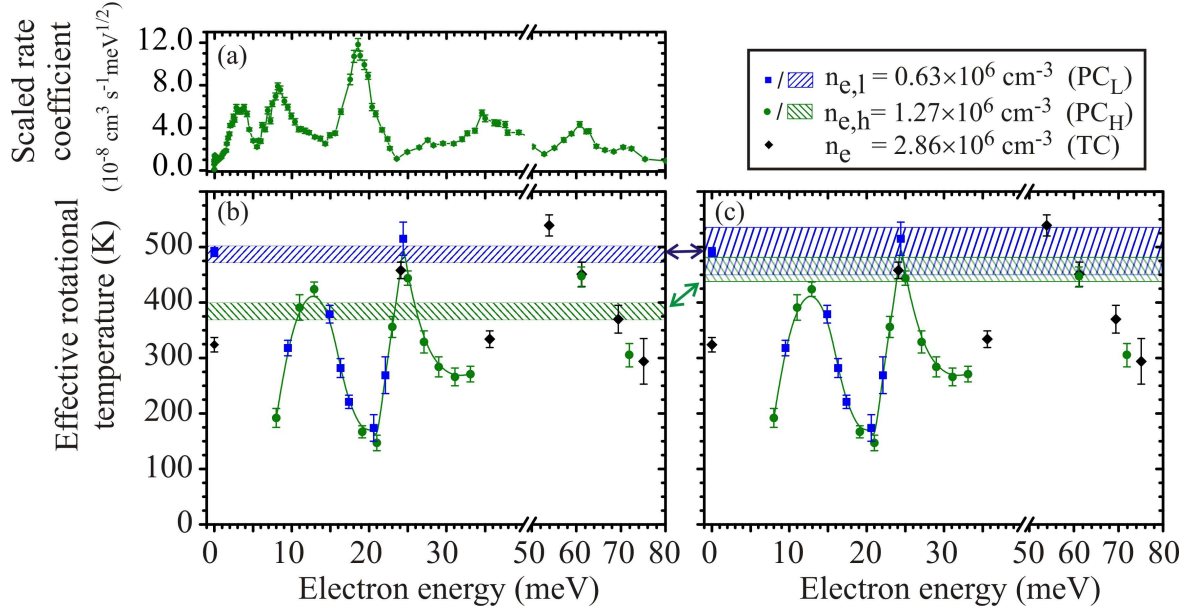
Figure 4.5: (a) Scaled, rotationally averaged DR rate coefficient $\tilde{\alpha}(E_d)$ and (b,c) effective rotational temperature as functions of the detuning energy E_d for the different measurements performed (see Table 4.1, lines to guide the eye). The two shaded bars extending over the full energy range mark the effective rotational temperature probed at zero detuning energy between 6.5 s and 7 s (b) [19] and between 17.0 s and 18.0 s (c), i.e. before and after the measurements at the detuning energy E_d.

Furthermore one observes that the effective rotational temperatures neither depend on the different electron densities employed in the measurements at detuning energies above 8 meV nor on the initial rotational state population reached after pre-conditioning the circulating ions with zero energy electrons. In fact, the measurements obtained with electrons generated by the thermal cathode show that although the electron target beam was detuned during the complete storage time period, their effective rotational temperatures are comparable to those which experience the initial combined cooling of the ion beam.

In contrast, at zero detuning energy super-elastic collisions cause electron density dependent changes in the effective rotational temperatures (see also Fig. 4.4 and [109]). Both the equilibrium temperatures obtained at the end of the cooling period as well as the effective temperatures measured between 7 s and 17 s without the electron cooler beam at $E_d = 0$ eV reflect differences between low and high electron densities attributed to rotational SEC.

After the detuning step, the electron target beam is set back to zero collision energy. This

allows to trace possible rotational excitations by non-zero electron collisions surviving the constant cooling effect induced by the electron cooler beam. The average effective temperatures extracted from reference measurements between 17 s and 18 s are compared in Fig. 4.5(c) (shaded bars for low and high electron density measurements, respectively) and indicate only at high electron densities possible preceding rotational excitations in contrast to the initial reference measurement between 6.5 s and 7 s (Fig. 4.5(b)). However, a general enhancement of $\sim$ 70 K related to the increased electron density cannot explain the distinct variations in T. In addition, at low electron densities the final reference measurements convincingly reveal an unchanged J^+-distribution of the stored ions. Therefore, rotational heating by non-zero electrons is found to be mostly compensated by the continuous cooling imposed by the electron cooler beam and remains at an insignificant level not able to explain the observed large variations in T at non-zero collision energies.

One can thus conclude that the energy dependence of T has to result from varying low and high rotational state contributions to the DR rate, which confirms the sensitivity of the HD$^+$ DR cross section below 80 meV on the initial rotational ion state, i.e. indicates state specific reaction rates.

In the second analysis step the rotational states participating to the total DR rate are obtained by treating their weighting factors b_{J+} individually. For the results presented in the following, the two lowest rotational states are combined in the fit to yield b_{01} and independent level contributions b_{J+} up to $J^+ = 7$ are included as free parameters as described above and in [18, 19].

Figure 4.6 gives an example for the transverse distance distribution measured at two selected detuning energies and thereby illustrates its sensitivity on the rotational state contributions at higher projected distances. Represented by the b_{01}-fraction the low-J^+ contributions dominate the recorded DR events at 21 meV (Fig. 4.6(a)) inducing a sharp edge limited by the maximum possible distance for $J^+ = 1$ (left arrow in (a) and (b)). Changing the detuning energy by only a few meV the ($J^+ = 0$ and 1)-fraction reduces rapidly and the overtaking high-J^+ signal smears out the right edge by an additional shift to larger distances (Fig. 4.6(b)). Influences caused by the different electron collision energies are negligible for these examples since the proportionality of the transverse distance to $\sqrt{E_{KER}}$ results in an increase by less than 0.1 mm for the added energy (compare the positions of the arrows in Fig. 4.6(a) relative to the ones in (b)).

The J^+-fractions obtained from all measurements on the energy grid are displayed in Fig. 4.7. They vary distinctly as a function of energy. Mostly, the lowest two rotational
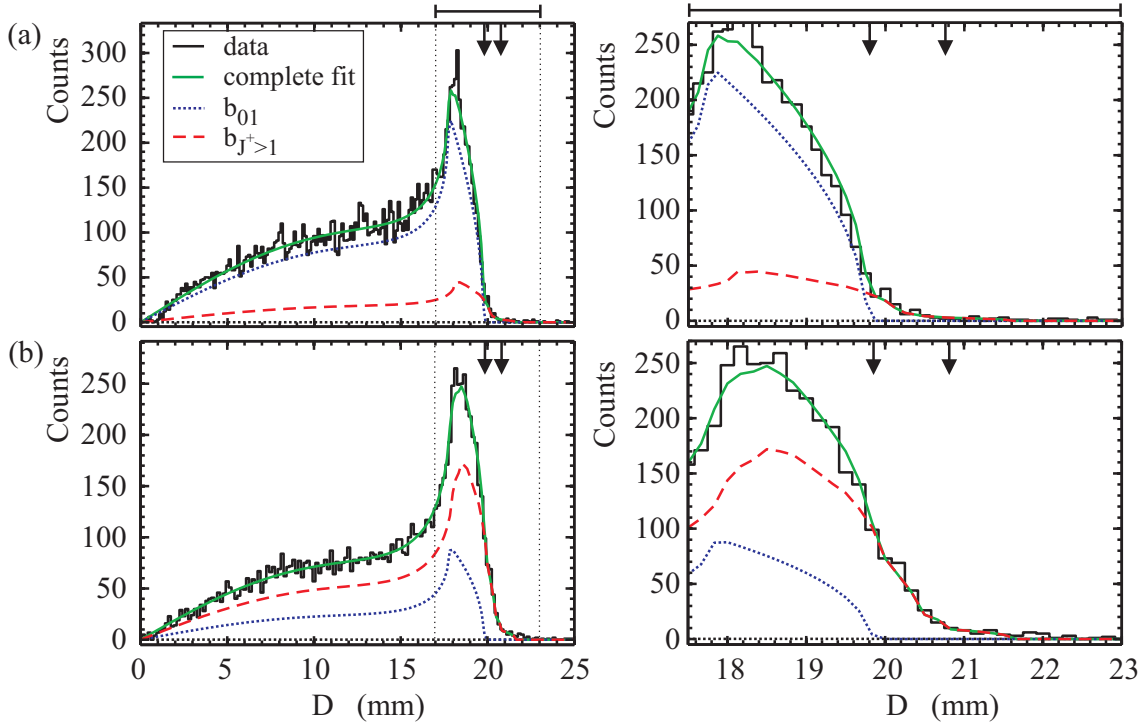
Figure 4.6: Transverse distance distributions at (a) 21 meV and (b) 25 meV are shown together with the total fit using individual J^+-contributions in Eq.(4.2) (solid lines, green). The relative low-J^+ (b_{01}, dotted blue line) and high-J^+ ($b_{>1}$, dashed red line) contributions are compared to the total fit result. The right figures enlarge the signal at large distances, respectively. The two arrows indicate the maximum distance expected for ions in $J^+ = 1$ and 5 ($v^+ = 0$).

state contributions b_{01} represent the dominant part of the recorded DR events, exceeding at certain energies more than 80%. The $J^+ = 7$ fraction, although formally included as a free parameter in the fit, is not shown in Fig. 4.7 as it was found to contribute even less to the total events than the $J^+ = 6$ fraction and thus does not yield any additional information.

In general, the J^+-fractions resemble an energy dependence which is found to be on a similarly narrow scale as the scaled, rotationally averaged DR rate coefficient $\tilde{\alpha}(E_d)$. Even most structures of the reaction rate are represented by the variations of the rotational state contributions. Note that certain energies are more pronounced by the b_{01}-contributions than one would expect from the variations of the DR rate coefficient. For example, between ~25 meV and ~ 33 meV only a slight increase in the total reaction rate is observed, which in contrast coincides with a strong change of the b_{01}-fraction. This indicates a DR resonance for ions in the $J^+ = 0$ and 1 state which is less pronounced and
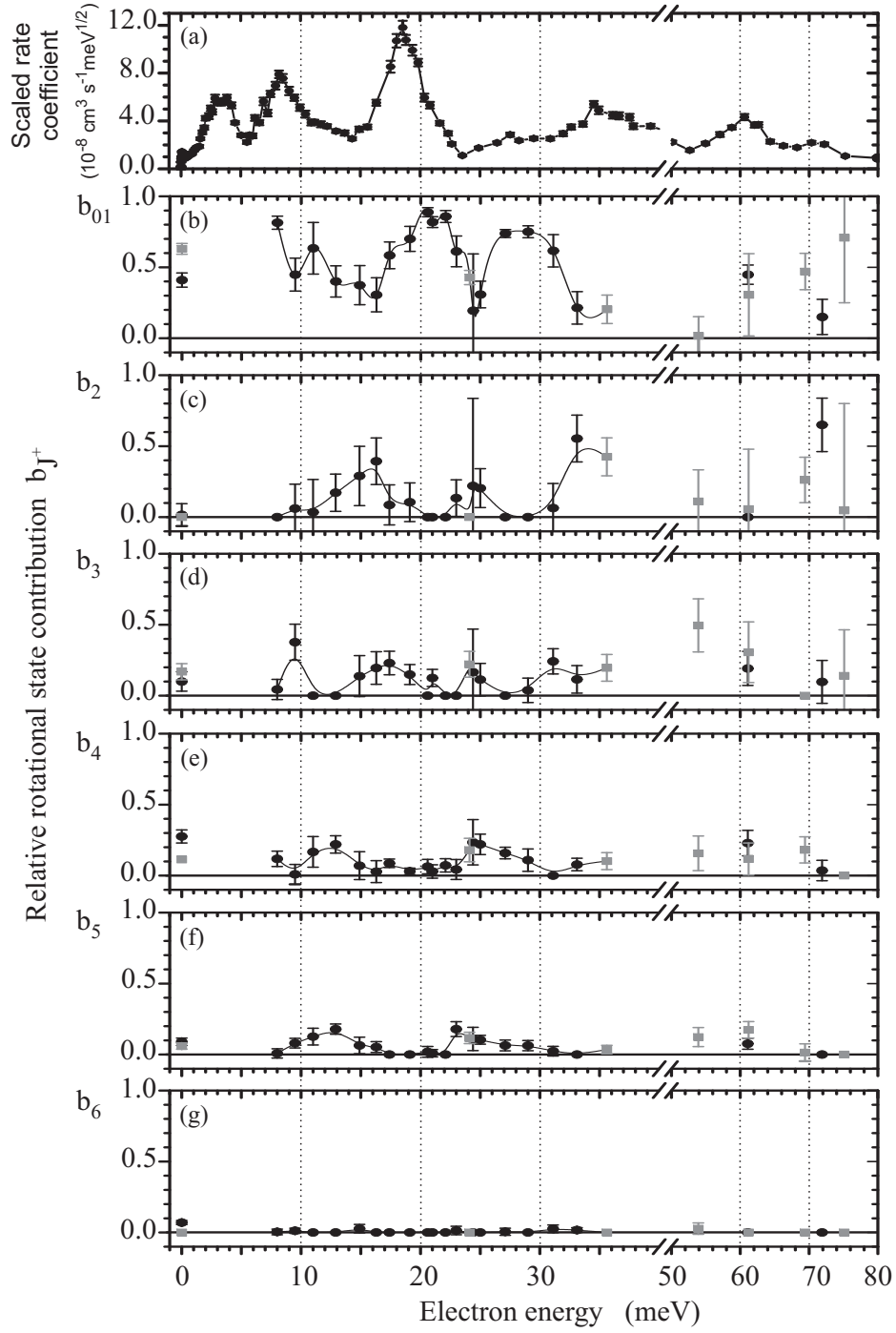
Figure 4.7: (a) The scaled rotationally averaged DR rate coefficient $\tilde{\alpha}(E_d)$ is compared (b - g) to the individual rotational state fractions b_{J+} deduced from fragment imaging measurements as function of the electron collision energy E_d. The different measurement conditions are distinguished by symbols (black circle: photocathode (PC), gray square: thermal cathode (TC) (see Table 4.1)). The zero eV result (black circle) corresponds to the PC_L condition.

hardly visible in the measured DR rate coefficient.

At the most dominant DR peak visible in the measured energy range ($\sim$19 meV) the maximum b_{01}-weighting factor is shifted by about 2-3 meV from the position of the maximum DR rate. The lowest rotational states are in fact mostly responsible for the decreasing right edge while at the energy of the maximum DR rate the next higher levels, $J^+ = 2$ and 3, give significant contributions.

On the other hand, the most pronounced high-J^+ contribution below 40 meV is associated with a dip in the DR rate coefficient. Here, the b_{01}-contribution drops within a few meV down to 20% and in turn J^+-fractions representing levels up to $J^+ = 5$ are observed.

At energies above 50 meV the fragmentation kinematics have been studied less dense and thus cannot be discussed on a similar narrow energy scale. In addition the DR rate drops quickly with increasing electron collision energy which imposes difficulties on collecting a comparable amount of DR events sufficient to reveal the rotational state contributions within small errors. Nevertheless, a general trend can be observed which indicates that the two lowest rotational states become increasingly important when changing the electron collision energy from $\sim$54 meV to $\sim$75 meV.

Summarized, these results experimentally reveal for the first time directly the dependence of the low-energy HD$^+$ DR process on the initial ionic state. Considering the common, initial rotational state population varying amounts of low, here mostly $J^+ = 0$ and 1, and high ionic rotational state fractions contribute to the total DR rate through resonant formation of intermediate ro-vibrational Rydberg states.

4.2.2   Fragment angular distributions

The fragment angular distributions are deduced from the transverse distance spectra by comparison with computed model functions expressed by Eq.(4.2). In doing so, the rotationally averaged anisotropy parameters a_l describe the contribution of the Legendre polynomial $P_l(\cos\theta)$ to the total angular distribution $W(\theta)$ (see detailed description in Sec. 3.2.2) and indicate through non-zero higher order coefficients increasingly fine angular emission patterns.

The measured transverse distance distributions lack the information on the fragment arrival times which accounts for their sensitivity on angular fragmentation patterns reflected by even order Legendre polynomials only. Possible asymmetric emissions differing between θ and $\theta - \pi$ ("*forward-backward asymmetry*") are represented by odd Legendre orders but are not observable in measurements restricted to the projected distance as discussed al-
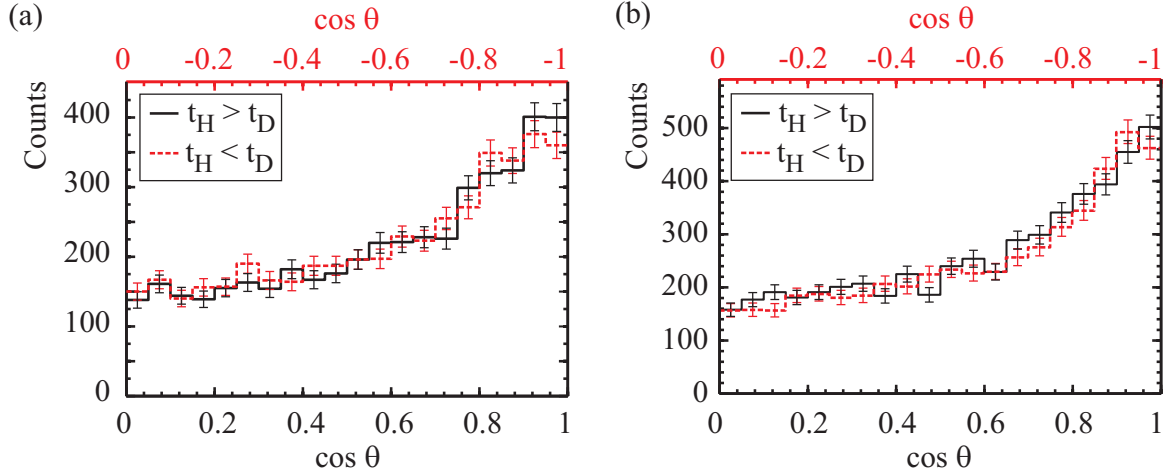
Figure 4.8: Measured fragment angular distribution at (a) 9.5 meV and (b) 19.1 meV. The solid black line describes the angular emission pattern for events where the deuterium arrives before the hydrogen fragment, whereas the dashed red line presents the opposite case.

ready in Sec. 3.2.2. In fact, odd-type angular distributions express the dependence of the electron capture on the component of the molecule directed along the beam axis towards the approaching electron, i.e. either the H or D fragment is arriving first at the detector. Consequently the observation of a forward-backward asymmetry requires the emitted fragments to be distinguishable and their impact time differences to be measured, i.e. full 3D detection.

In order to examine the HD^+ angular distributions for possible contributions stemming from odd Legendre polynomials, the 3D data are used in the analysis after the fragments have been identified according to the procedure described in Sec. 3.3.2. The obtained angular emission patterns, sorted for events with either the hydrogen ($t_H < t_D$) or deuterium ($t_H > t_D$) fragment arriving first at the detector, are found to show no significant difference between θ and $\theta - \pi$. Two examples at different detuning energies have been depicted in Fig. 4.8. The observed forward-backward *symmetry* suggests that the mass of electronically identical atomic components does not influence the capture probability of an electron in low-energy HD^+ fragmentation. In contrast, for electronically different atomic components the electron capture has been observed to be indeed sensitive on the fragment which is directed towards the approaching electron [113]. In these recent, precise 3D imaging measurements on the DR induced breakup of CF^+ at detuning energies in the range of ~ 1.5 eV, the forward-backward asymmetry has been demonstrated finding a preference for the dissociation when the carbon atom is directed towards the incoming
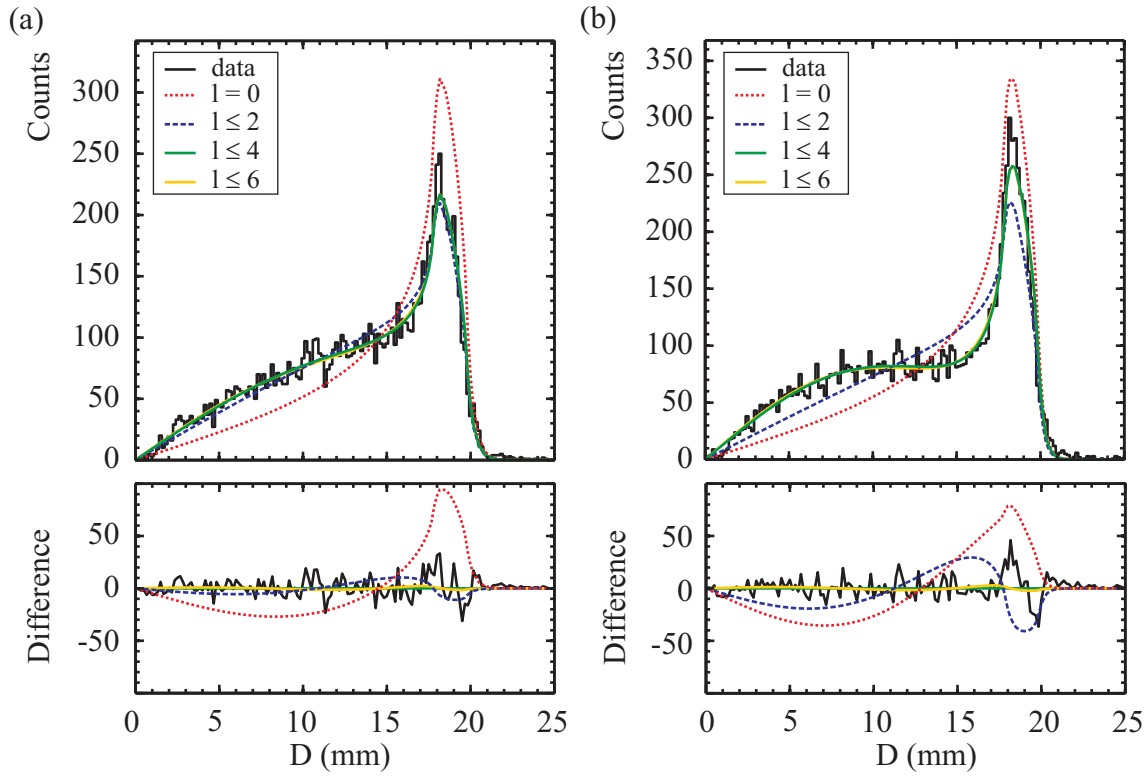
Figure 4.9: Measured transverse distance distributions (black line) for (a) 23.0 meV and (b) 29.0 meV detuning energy are shown together with the best fit results restricted to angular distributions of type $l = 0$ (red, dotted line), $l \leq 2$ (blue, dashed line), $l \leq 4$ (green, solid line) and $l \leq 6$ (yellow, solid line). Below the difference between the fitted line shape associated with $l \leq 4$ and the recorded transverse distance distribution as well as the higher and lower order fit results are displayed.

electron.

Back to the present analysis on HD$^+$, this implies that the angular distributions are sufficiently described by even order Legendre polynomials and the fragment angular emission properties can entirely be deduced from the measured transverse distance spectra, so that the high resolution of the 2D measurement can be exploit.

So far, experiments on angular emission patterns of DR induced breakup events have exclusively obtained non-zero Legendre coefficients a_l with a maximum order $l = 2$ (see, e.g. [55, 56, 57]). In contrast, the measurements presented here, represented by two examples in Fig. 4.9, point out the importance of higher order contributions. Neither transverse distance distribution shown in Fig. 4.9 can be associated with an isotropic fragment emission ($l = 0$) and also including the two lowest even order Legendre polynomials ($l \leq 2$) does not resemble the complete projected distance line shape. Instead, the necessity of

the $l = 4$ order is stressed by the comparison to the lower order fit results. On the other hand, the next higher even order ($l = 6$) is found to give only an insignificant additional contribution. Therefore in the final analysis anisotropy coefficients of even order up to $l \leq 4$ are considered, whereas higher orders are forced equal to zero.

Energy sensitive fragment angular characteristics

The angular distributions of the emitted neutral particles are obtained together with the rotational state contributions (Sec. 4.2.1) of the recorded DR events on the same low-energy grid. Thereby the deduced rotationally averaged anisotropy coefficients a_2 and a_4 ($a_0 = 1$ for normalization) yield within the errors the same results independent whether the rotational state contributions are extracted through an effective rotational temperature T or represented by individual parameters b_{J+} in the fit. Hence, subsequently only the results obtained from the latter fitting procedure are presented, i.e. considering individual rotational state fractions b_{J+}.

Already the two examples displayed in Fig. 4.9 have indicated an anisotropic fragment emission at the applied low electron collision energies and revealed significant contributions of Legendre polynomials of 2nd and 4th order in the fitting procedure. Furthermore, similar to the extracted rotational state fractions in Sec. 4.2.1 the angular emission pattern is found to vary within only a few meV. The enhancement of events with low transverse distances D ($\lesssim 15$ mm) suggests in either example of Fig. 4.9 a preferential dissociation parallel to the beam direction, whereas the probability for perpendicular fragment emission ($D \geq 15$ mm) is reduced compared to a normalized isotropic angular distribution.

In order to accentuate the changes of the fragment angular distributions described by the deduced anisotropy parameters (a_2,a_4), they are compared for selected detuning energies in the polar diagram representation in Fig. 4.10. Therein the total fit results are contrasted for increasing electron collision energies to the respective contribution from the lowest two Legendre polynomials as well as to the case of isotropic emission. Note, that the deduced angular fragmentation properties are repeated in each quarter due to the axial as well as the forward-backward symmetries exhibited in the measurement.

For vanishing contributions of the 4th order Legendre polynomial and positive anisotropy coefficients a_2, reflecting the example in Fig. 4.10(a) at 14.9 meV, the fragment angular distribution approaches a nearly dipole-type emission pattern directed parallel to the beam axis ($\theta = 0°$). Together with the increase of the detuning energy the measured angular distributions in Fig. 4.10 are more and more associated with a simultaneously elevated a_4 coefficient, while the a_2 anisotropy parameter is remaining at an almost con-
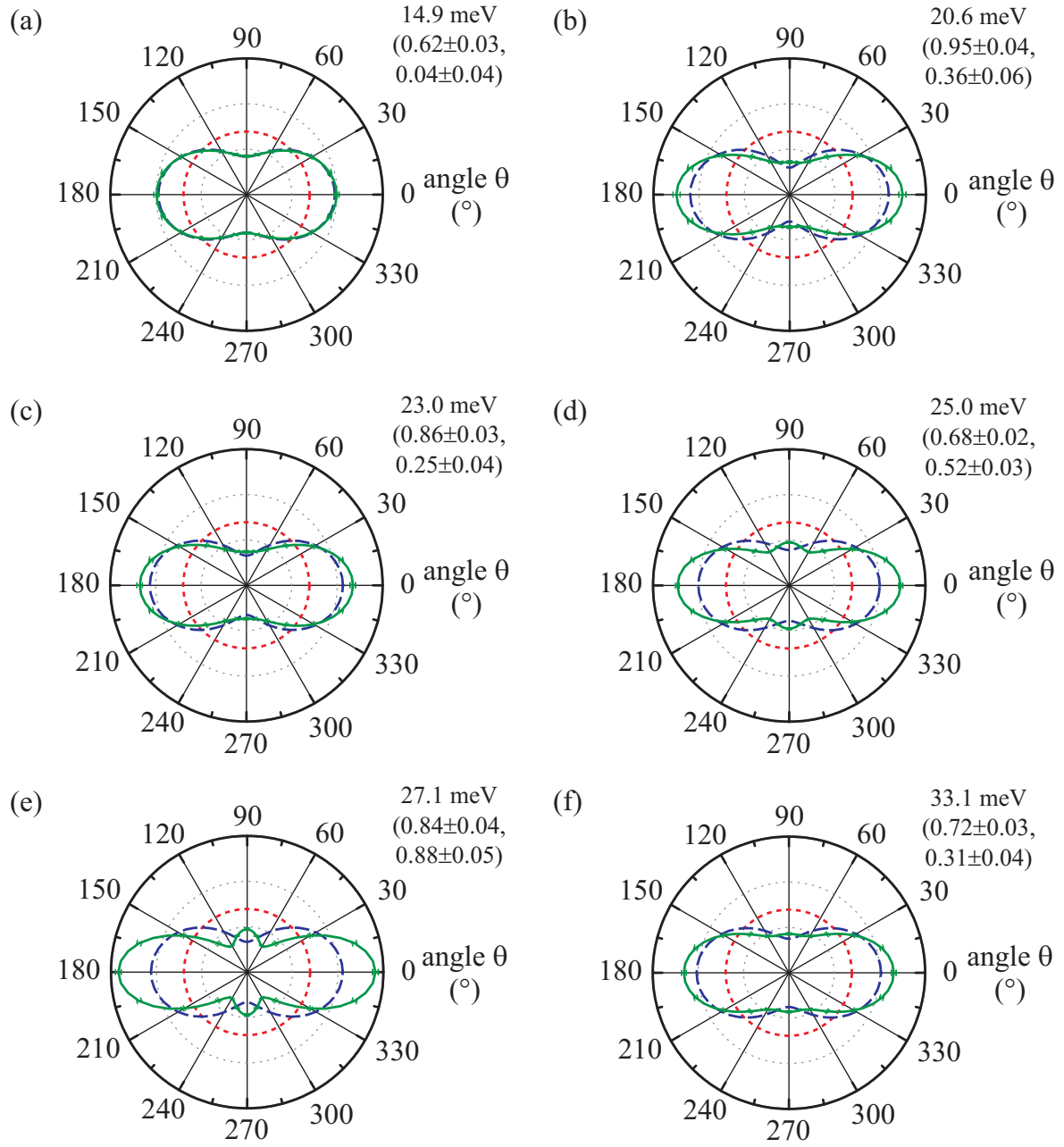
Figure 4.10: The total fit results (solid green line) are compared to the contributions of the two lowest Legendre polynomials (dashed, blue line) and the isotropic distribution (dashed, red line) in the polar diagram representation at different detuning energies between 14.9 meV and 33.1 meV. The deduced anisotropy coefficients (a_2, a_4) for the respective total fits are given for each measured energy.

stant value. This corresponds to an enhanced fraction of fragments directed into both extreme directions, i.e. perpendicular ($\theta = 90°$) and parallel to the beam axis, resulting in a quadrupole type emission characteristic.

All anisotropy coefficients deduced from the transverse distance distributions are presented in Fig. 4.11 as function of the electron collision energy E_d [18, 106]. The Legendre parameters clearly deviate from a value equal to zero, i.e. an isotropic fragmentation, and feature structures on a similarly narrow energy scale as the scaled DR rate $\tilde{\alpha}(E_d)$. Even for certain conditions at zero detuning energy a small but significant anisotropic fragmentation is observed [19] (see next paragraph). Enhanced anisotropic emission patterns are generally found to coincide with peaks in the low-J^+ fraction b_{01}. The 4th order Legendre contribution, observed for the first time in DR induced fragmentation patterns, turns out to be particularly sensitive on the detuning energy E_d and decreases for E_d approaching 0 eV as recognized already above. In contrast, the a_2 parameter oscillates slightly around a value of 0.8 for energies above 8 meV.

The largest change associated with the a_4 coefficient occurs between ∼24 meV and ∼30 meV, where in fact no distinct structure is found in the measured DR rate. The same energy range is also accentuated by a pronounced increase of the b_{01}-fraction discussed in the previous section, thus presenting an example where the measurement of the fragmentation kinematics can yield additional information on the DR process.

On the other hand, large fractions of highly rotating molecules, i.e. small low-J^+ contributions, seem to correlate with minima in the anisotropy parameters. This can hint at a loss of the anisotropy due to sizable rotation of the molecular axis before the dissociation and thus possibly indicates a breakdown of the non-rotation assumption of the axial-recoil approximation.

The partial correlation of the variations found in the anisotropy parameters and the extracted rotational state fractions may also allude to J^+-dependent fragment anisotropies, which are not accessible through the rotationally averaged anisotropy coefficients. In fact, due to the small energy difference between the rotational levels of the hydrogen molecule, the J^+-dependence of the angular distributions can only be disentangled by full initial ro-vibrational state selectivity of the provided ions in the experiments. This is difficult to attain for the HD$^+$ molecular ion. Although it radiatively cools to the ground vibrational state, the radiative coupling to the background radiation may still populate several rotational levels. For the H$_2^+$ molecular ion, on the other hand, state-selective experiments become feasible once selected ro-vibrational states can be produced initially. This has enabled the experiments discussed in Ch. 5.
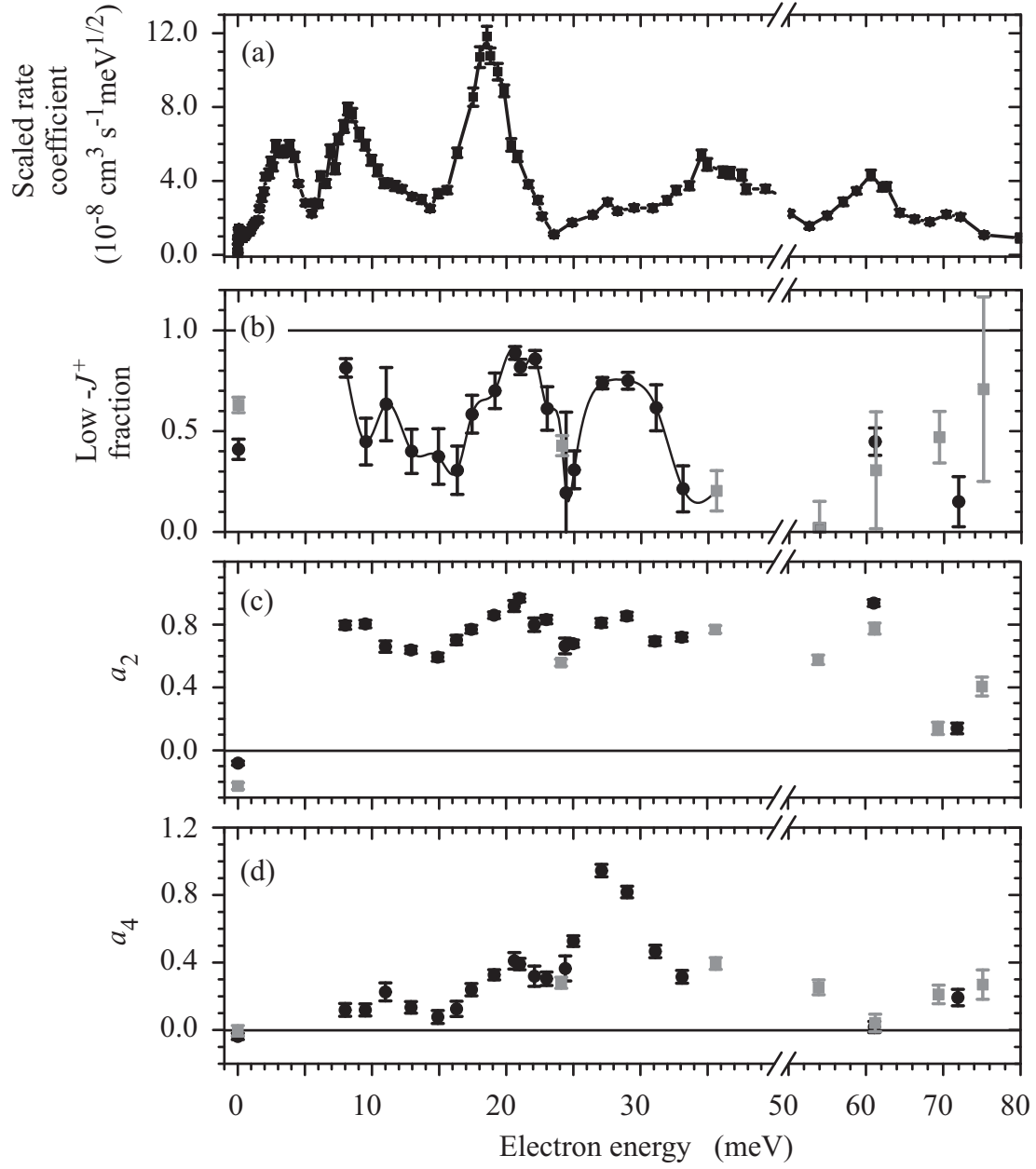
Figure 4.11: (a) Scaled, rotationally averaged DR rate coefficient $\tilde{\alpha}(E_d)$, (b) low-J^+ fraction b_{01} (symbols connected to guide the eye), and (c, d) Legendre coefficients a_2 and a_4 as functions of the detuning energy E_d [18]. The photocathode was used except for the gray symbols indicating use of the thermionic cathode.

Angular fragmentation at near-zero energy

The measured fragment angular distribution is determined both by the velocity distribution of the electrons as well as the angular dependence of the electron-ion interaction. This yields for electrons featuring a spherical symmetric energy distribution centered around the detuning energy and approaching randomly oriented molecules, a fragment angular distribution which has to be isotropic due to symmetry reasons if the detuning energy is set to zero. In that case the incoming electrons exhibit no preferred direction to probe the angular dependence of the DR process so that only an isotropic angular distribution of the recorded fragments can be the result.

However, the flattened Maxwellian velocity distribution of the electron beam breaks the spherical symmetry in the experiments and thus anisotropic fragment emissions are even possible at $E_d = 0$ eV. In the measurements presented here this could be demonstrated for the first time in DR induced molecular breakup [19]. As expected the effect is sensitive on the electron temperatures, in particular on the transverse temperature as $T_\perp \gg T_{||}$. They determine the electron velocity distribution and can be controlled in the current experimental setup at the TSR mainly by the choice of the electron beam production.

In fact, an anisotropic fragmentation characterized by a small but statistically significant negative a_2 coefficient (Fig. 4.11) is only observed applying electrons generated in the thermal cathode at an estimated transversal temperature of $kT_\perp \sim 2.0$ meV, while the fragment distribution obtained with the colder photocathode electron beam, which is characterized by $kT_\perp \sim 0.5$ meV, is still compatible with an isotropic emission. Both transverse distance distributions are compared in Fig. 4.12(a) and (b) with the fit result and an isotropic fragmentation line shape.

In contrast to the angular distribution results at non-zero detuning energies the anisotropic angular emission at zero detuning energy prefers fragment directions perpendicular to the beam direction, expressed by the deduced negative a_2 parameter. Note, that the negative a_2 coefficient qualitatively agrees with the anisotropy coefficients at non-zero detuning energies considering for the small thermal electron velocity spread a change of electrons predominantly approaching from the longitudinal direction at the applied non-zero collision energies to the case of electrons exhibiting mainly a perpendicular approach caused by the transverse electron temperature. This can be pictured as a rotation of the c.m. frame by $\theta = 90°$ and hence explains the observed change of the a_2 sign.
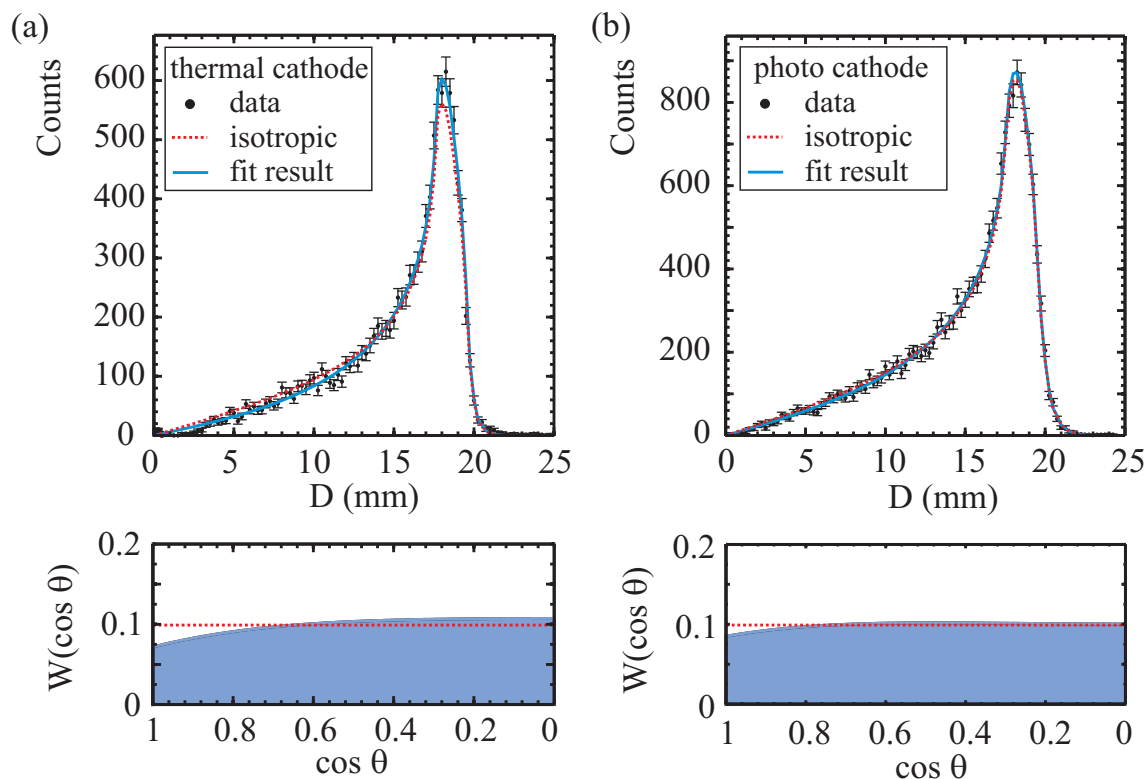
Figure 4.12: Transverse distance distributions measured at zero detuning energy with either electrons emitted by (a) the thermal cathode (TC, see Table 4.1) or (b) the photo-cathode (PC$_L$). The data are compared to an isotropic line shape (red dotted line) and the fit result including Legendre contributions of order $l \leq 4$ (blue solid line). In the lower graphs the angular distribution deduced from the fit (blue shaded area) is compared to the isotropic emission (red dotted line) as a function of $\cos\theta$.

4.3 Angular distribution models

The observed fragmentation kinematics, which are described by the obtained rotational state contributions and the angular emission of fragments, suggest an extremely energy sensitive dynamical picture associated with the low-energy DR of HD$^+$. Additional aspects of the ro-vibrational Feshbach resonances become attainable reflecting through the J^+-contributions their sensitivity on the initial ro-vibrational state of the ion whereas the fragment angular distribution can be linked to the angular dependence of the electron capture process.

The DR angular dependence is determined by the electronic symmetries involved in the process. Theoretical descriptions of electron-molecule collisions have traced the source of the dependence on the molecule's orientation to the electronic coupling matrix element

$V_{el}(\theta)$ as introduced in Secs. 2.2.2 and 2.2.3 for DEA and DR, respectively. Measured fragment angular distributions $W(\theta)$ can thus be compared as $W(\theta) \propto |V_{el}(\theta)|^2$ and give experimental access to the electronic symmetries participating in the reaction.

For the results presented here on the low-energy range only one dissociative state is responsible, which anticipates that the observed variations of the angular fragmentation characteristics cannot be explained by the symmetries of the involved molecular configurations alone, as initially suggested by Dunn [39]. In fact, also the electronic symmetries of the incoming electron's partial waves have to be considered once they couple to the ionic molecular state in the process. For HD$^+$ the importance of the d partial-wave has long been predicted by theory [14, 71] which encourages the expectation of an anisotropic dissociation pattern even at low electron collision energies. In addition, some s-wave ($l = 0$) contribution possibly has to be taken into account as calculations of the electronic couplings have shown and its importance for the resonant structure of the DR cross section has been revealed [16, 72].

In the following the measured angular fragmentation characteristics are contrasted via the deduced Legendre coefficients with two theoretical approaches. First, the measured fragment angular directions are compared to model distributions that are based on a partial wave description of the angular dependence in the DR process [59] (see also Sec. 2.2.3). Subsequently, recently performed Multichannel-Quantum-Defect-Theory (MQDT) calculations which implicitly include calculated electronic couplings of the participating partial waves are contrasted with the results [114]. Both theoretical approaches are based on the assumption of a molecule rotating slow compared to the time required for dissociation, i.e. are only valid in the axial-recoil approximation. In particular for the fast rotations, which the hydrogen ion exhibits already for low rotational quantum numbers, the validity of this assumption is questionable and requires the discussion of possible consequences in the end.

4.3.1 Partial wave approach

In this section the measured fragment angular distributions are compared to those expected for the DR of HD$^+$ from theoretical calculations based on the configuration-interaction approach [59]. This concept has already been introduced in Sec. 2.2.3. Accordingly the product angular distributions are expected to be determined by the electronic symmetry of the molecular configuration as well as the one of the incoming electron represented by the coupled partial wave. In fact, the predicted fragment angular distribution is proportional to the squared absolute value of the dominating partial wave's spherical

harmonic for a slow rotating molecule (Eq.(2.15)).

First, a pure d-wave induced DR angular dependence is considered within the axial-recoil approximation. For a molecule which is aligned under an angle δ with respect to the incident electron direction $\hat{R}_e$ (see Fig. 4.13) the angular dependence $d\sigma(\delta)/d\Omega$ is determined according to Table I. in [59] by the $Y_{2,0}$-spherical harmonic:

$$
\begin{aligned}
\frac{d\sigma(\delta)}{d\Omega} &= \|V_{el}(\delta)\|^2 && (4.6)\\
&= \|Y_{2,0}(\cos\delta)\|^2 \\
&= \frac{5}{4}(3\cos^2\delta - 1)^2 \\
&= 1 + \frac{10}{7}P_2(\cos\delta) + \frac{18}{7}P_4(\cos\delta) && (4.7)
\end{aligned}
$$

with $\cos\delta = \hat{R}_e \cdot \hat{R}$. The expected angular distribution is normalized so that $\int_0^{2\pi} d\phi \int_0^{\pi} \|V_{el}(\delta)\|^2 \sin\delta\, d\delta = 1$. For unidirectional electrons pointing along the ion beam direction ($\beta = 0 \to \delta = \theta$), the description converts to a fragment angular distribution expressed by even order Legendre polynomials $P_l(\cos\delta)$ ($= P_l(\cos\theta)$) with $l \leq 4$, as indeed found in the experimentally obtained angular emission characteristics in the DR of HD$^+$. However, in order to compare the experimental results to the explicitly predicted coefficients $\tilde{a}_2 = 10/7$ and $\tilde{a}_4 = 18/7$ of a pure d-wave capture (Eq.(4.7)), the influence of the finite electron velocity spread has to be taken into account. This becomes particularly important at low electron collision energies approaching the electron energy spread determined by $T_\parallel$ and $T_\perp$. At these energies the electron velocity distribution is no longer compatible with an unidirectional approach so that the different incident electron directions yield a superposition of fragment angular distributions. Hence, since not all electrons approach the molecule parallel to the ion beam direction $\hat{R}_{beam}$, that is $\beta \neq 0$, the product angular distribution $d\sigma(\delta)/d\Omega$ has to be transformed to a $\hat{R}_{beam}$-centered frame in order to enable the comparison to the measured fragment angular distributions.

The coordinate transformation utilizes the Wigner formulas [115] for the rotation of spherical harmonics $Y_{l,m}$ through angles represented by the Euler angles (α, β, γ):

$$
Y_{l,m}(\cos\delta) = \sum_{m'=-l}^{+l} Y_{l,m'}(\cos\theta)\, R^{(l)}_{m,m'}(\alpha, \beta) \qquad (4.8)
$$

where due to symmetry reasons the angle γ is set equal to zero. Assuming axial symmetry with respect to $\hat{R}_e$ integration over the Euler angle α transforms an angular dependence $d\sigma(\delta)/d\Omega$ of type $1 + \tilde{a}_2 P_2(\cos\delta) + \tilde{a}_4 P_4(\cos\delta)$ into

$$
\frac{d\sigma(x, u)}{d\Omega} = 2\pi\left[1 + \tilde{a}_2 P_2(x)P_2(u) + \tilde{a}_4 P_4(x)P_4(u)\right] \qquad (4.9)
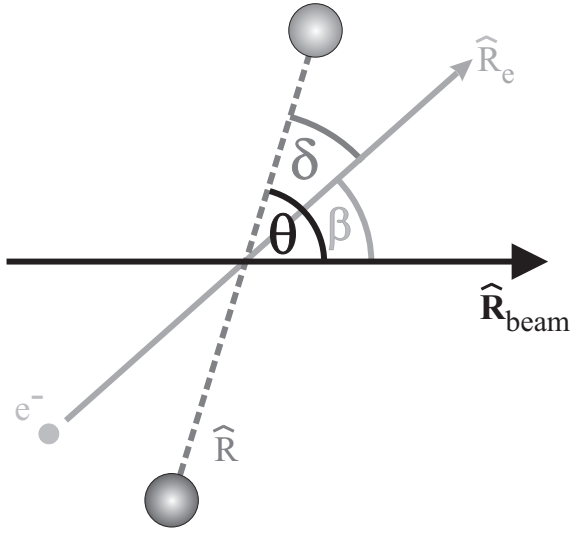$$

Figure 4.13: Geometric correlation of the electron direction $\hat{R}_e$ and the molecular orientation $\hat{R}$ with respect to the ion beam $\hat{R}_{beam}$.

where x and u are defined by $x = \cos\beta$ and $u = \cos\theta$. The expected fragment angular distribution $W(\theta, E_d)$ at a defined detuning energy E_d is then obtained after convolution of $d\sigma(x, u)/d\Omega$ over all electron velocities and directions:

$$
\begin{aligned}
W(\theta, E_d) &= \frac{1}{m_e} \int_0^\infty dE \int_{-1}^1 dx \, \sigma(E) \frac{d\sigma(x, u)}{d\Omega} f(E, E_d, x) \\
&= \frac{2\pi A}{m_e} \int_0^\infty dE \, \sigma(E) \, e^{-\dfrac{E - E_d/\xi}{k\,T_\perp}} \\
&\quad \cdot \int_{-1}^1 dx \, [1 + \tilde{a}_2 P_2(x) P_2(u) + \tilde{a}_4 P_4(x) P_4(u)] \cdot e^{-\dfrac{(\xi\, x\, \sqrt{E} - \sqrt{E_d})^2}{\xi\, k\, T_\parallel}} .
\end{aligned}
$$

(4.10)

Therein $\sigma(E)$ denotes the energy dependent, but angle independent, part of the DR cross section, E the electron energy, m_e the electron mass, $\xi = 1 - \frac{T_\parallel}{T_\perp}$ and the constant A is defined by Eq.(12) in Appendix B. Note, that in Eq.(4.10) the electron velocity distribution $f(\vec{v}_e, v_d)$ (Eq.(3.12)) is represented in energy space $f(E, E_d, x)$ according to Eq.(14) derived independently in Appendix B.

The initial Legendre coefficients $\tilde{a}_l$ are thus related to the measured anisotropy coefficients
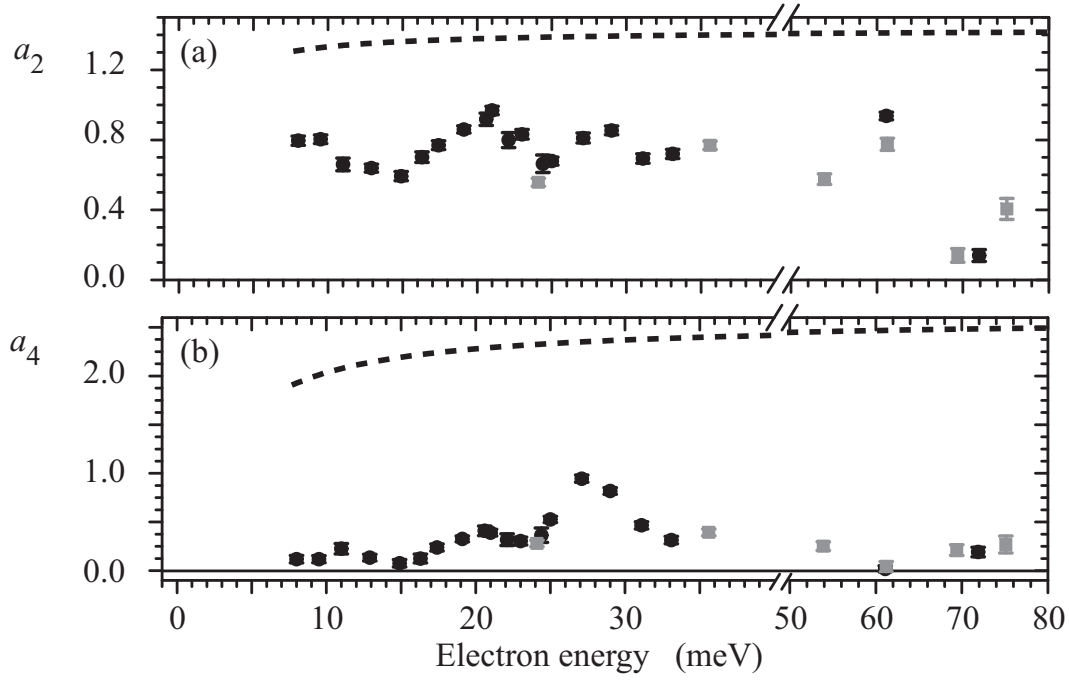
Figure 4.14: Measured Legendre coefficients a_2 (a) and a_4 (b) are compared to the expected angular dependence of a pure d partial-wave contribution to $V_{el}(\theta)$ after convolution with the flattened Maxwellian velocity distribution of the electron beam (dashed lines in (a) and (b)) [18]. (for symbols see caption of Fig. 4.11)

$a_l = \chi_l(E_d)\tilde{a}_l$ through attenuation factors $\chi_l(E_d) \leq 1$ ($l = 2, 4$; $\chi_0 = 1$):

$$\chi_l(E_d) = \frac{\int\limits_0^\infty dE\, \sigma(E)\, e^{-\frac{E - E_d/\xi}{k\,T_\perp}} \int\limits_{-1}^{1} dx\, P_l(x) \cdot e^{-\frac{(\xi\, x\, \sqrt{E} - \sqrt{E_d})^2}{\xi\,k\,T_\parallel}}}{\int\limits_0^\infty dE\, \sigma(E)\, e^{-\frac{E - E_d/\xi}{k\,T_\perp}} \int\limits_{-1}^{1} dx\, e^{-\frac{(\xi\, x\, \sqrt{E} - \sqrt{E_d})^2}{\xi\,k\,T_\parallel}}} \tag{4.11}$$

which deviate for the present low transverse electron temperatures by only less than 20% from unity for detuning energies above 8 meV [18].

In Fig. 4.14 the deduced Legendre coefficients a_l are compared to the values $a_l = \chi_l(E_d)\tilde{a}_l$ characterizing a pure d-wave induced angular dependence[1], i.e. $\tilde{a}_2 = 10/7$ and $\tilde{a}_4 = 18/7$, using $\sigma(E) \propto 1/E$ in Eq.(4.11) [18]. The experimental results confirm the predicted role of the d-wave in the DR of HD$^+$ through the significant contribution of the 4th

---

[1]The corresponding expected transverse distance distribution is illustrated in Fig. 3.2 of Sec. 3.2.2 for unidirectional electrons.
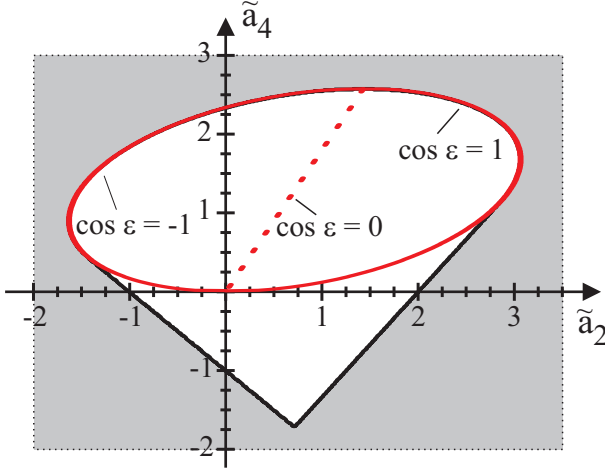
Figure 4.15: The generally allowed parameter range ($[\tilde{a}_2, \tilde{a}_4]$; white area including the black edge) is restricted in the description of a coherent sum of s and d-waves by $0 \leq |c_d|^2 \leq 1$ and $-1 \leq \cos \epsilon \leq 1$ (area within solid red line).

order Legendre polynomial obtained from the measured fragment emission anisotropies. Nevertheless, in particular the a_4 coefficients are found to strongly deviate from a pure d-wave description, contrary to the predicted dominance of the partial wave in the electron capture. Also, this model fails to reproduce the energy dependent narrow variations and instead predicts almost constant emission patterns independent of the electron detuning energy. The overall reduction of the measured anisotropies expresses a more isotropic distribution which may indicate significant contributions from the s partial-wave.

Therefore, in the next step, the more general case of interfering s and d partial-waves is considered [18]. Assuming that the theoretical approach [59] can simply be extended to the case of a coherent sum of two partial waves, i.e. their contribution to the angular dependence is still separable from the total expression of the DR cross section σ, the angular dependence may be expressed by

$$\frac{\sigma(\delta)}{d\Omega} = \|c_s\, Y_{0,0} + c_d\, Y_{2,0}\|^2 \ . \tag{4.12}$$

Here, the parameters c_s and c_d denote the complex s and d-wave amplitudes, respectively, and are related to each other through the normalization condition $c_s = \sqrt{1 - |c_d|^2}$. They are associated to the measured Legendre coefficients a_l through the relations :

$$a_2 = \chi_2(E_d) \left\{ 2\,|c_d|\,\sqrt{5(1 - |c_d|^2)} \cos \epsilon + (10/7)\,|c_d|^2 \right\} \tag{4.13}$$

$$a_4 = \chi_4(E_d)\,(18/7)\,|c_d|^2 \tag{4.14}$$

which are simply derived from Eq.(4.12) by expressing $Y_{0,0}$ and $Y_{2,0}$ through Legendre polynomials of order $l \leq 4$. In Eq.(4.13) the parameter ϵ describes the s and d relative phase. The parameter range for $\tilde{a}_2$ and $\tilde{a}_4$ ($= a_l/\chi_l(E_d)$), restricted by $0 \leq |c_d|^2 \leq 1$ and $-1 \leq \cos \epsilon \leq 1$, is illustrated in Fig. 4.15. Hence, the relative d-amplitude $|c_d|^2$ is
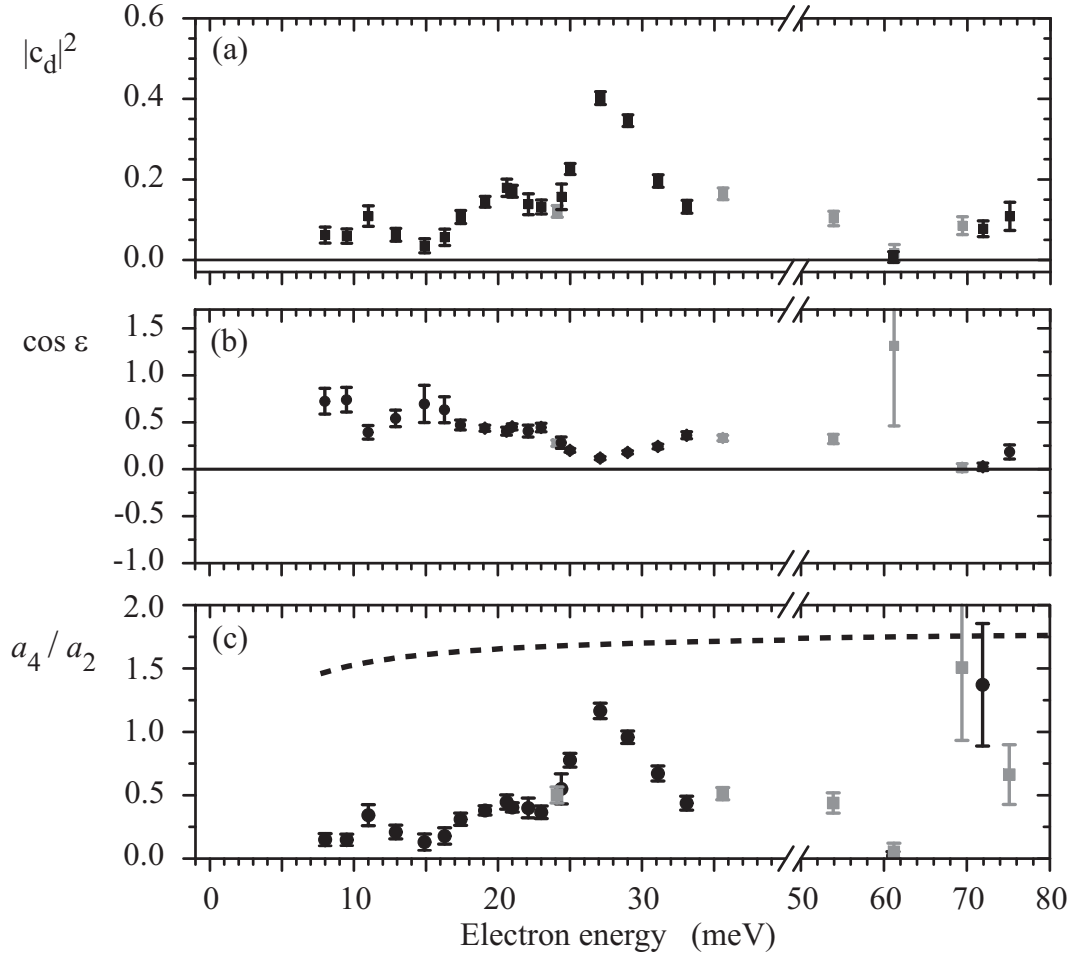
Figure 4.16: Assuming a coherent superposition of s and d partial-waves (a) the relative d-wave amplitude $|c_d|^2$, (b) the s and d relative phase represented by $\cos \epsilon$ and (c) the ratio a_4/a_2 are given for the measured results. The a_4/a_2 ratio is compared to the case of incoherent superposition of both symmetries reflected by $\tilde{a}_4/\tilde{a}_2 = 9/5$ after considering the flattened Maxwellian velocity distribution of the electron beam (dashed line). (for symbols see caption of Fig. 4.11)

proportional to the a_4 anisotropy coefficient and can directly be read off from the values in Fig. 4.11(d), considering $\chi_4(E_d)$. Presuming that the axial-recoil approximation applies, the deduced d-wave amplitudes $|c_d|^2$ shown in Fig. 4.16(a) are small in accordance to the earlier conclusion finding a pure d-wave contribution not supported by the measured anisotropy coefficients. In fact, the maximum value of $|c_d|^2$ does not exceed 0.5 and in addition rapidly decrease towards $E_d = 0$ eV.

In addition, both the a_2 and a_4 values jointly yield the s and d relative phase ϵ displayed in Fig. 4.16(b). At low detuning energies the relative phase ϵ reveals near-zero values

while a trend towards $\pi/2$ for increasing energy can be observed. The compliance of an incoherent superposition of both partial waves is reflected by $\cos \epsilon = 0$ or, can in fact directly be traced by the a_4/a_2 ratio in Fig. 4.16(c). Here an incoherent superposition is represented by $\tilde{a}_4/\tilde{a}_2 = 18/10$ which corresponds to the dashed line after applying the convolution factors $\chi_l(E_d)$. The results are mostly consistent with interfering s and d-waves, i.e. significantly deviate from the dashed line in Fig. 4.16(c), whereas only the measurements close to $E_d = 70$ meV possibly indicate an underlying incoherent process.

Overall the contributions from 4th order Legendre polynomials deduced in the present fragment angular distribution studies comply with the expected d-wave coupling in the HD$^+$ DR process. In fact, according to the applied theoretical approach the highest order Legendre coefficient can only be induced by a d-wave coupling and thus directly reflects its relative amplitude. However, the analysis within the axial-recoil approximation has also revealed that the d-wave is not dominant and cannot alone explain the variations in the anisotropy coefficients which are observed when passing over the ro-vibrational Feshbach resonances at low electron collision energies. At least equally large s-wave contributions are suggested to interfere coherently with the d-wave in most part of the studied energy range. The s and d-wave mixing thereby seems extremely energy sensitive and varies as represented by the relative phase ϵ or the a_4/a_2 ratio in Figs. 4.16(b) and (c) on a similarly narrow scale as the DR rate coefficient (Fig. 4.11(a)).

The applicability of the axial-recoil approximation is required for the comparisons stated above. This implies long rotational periods compared to the dissociation time. Any delay in the dissociation process of the fragments and a simultaneous considerable rotation of the molecule might smear out the angular dependence towards the observation of an isotropic distribution which would be undistinguishable from an enhancement of the s-wave contribution.

4.3.2 MQDT description of the angular dependence

The previous comparison of the obtained angular distributions with the theoretical framework proposed by Guberman has stressed the importance of both s and d partial-wave couplings to the ionic ground state $^2\Sigma_g^+$ in the description of the HD$^+$ DR product angular dependences. Utilizing this theoretical framework and relying on the axial-recoil approximation, the s and d-wave relative amplitudes and phases can be deduced from the experimental results.

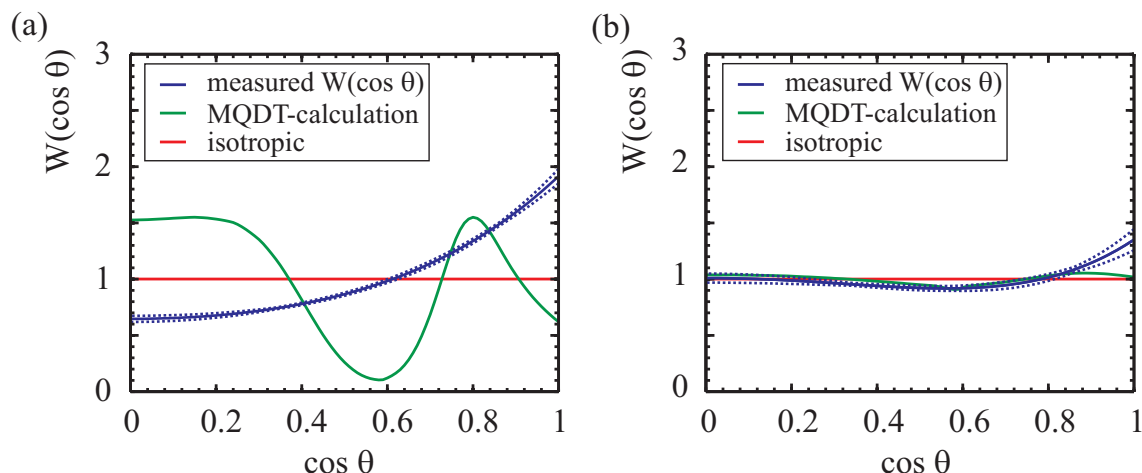On the other hand, a prediction of the expected angular dependences requires the in-

Figure 4.17: The angular emission characteristics predicted by MQDT-calculations in the axial-recoil approximation [114] (green line) are compared to the measured fragment angular distributions (blue line; dashed lines give error margin) at (a) 8.0 meV and (b) 69.4 meV. For comparison also the isotropic case is shown (red line).

formation on the electronic couplings of the s and d partial-waves. Within a recent first attempt, MQDT-calculations on the DR angular dependence of HD$^+$ were performed [114] computing electronic couplings of both partial waves. Since the implemented electronic couplings itself do not exhibit an explicit angular dependence, the angular dependence is included by multiplying the couplings with the spherical harmonics of the respective partial waves, i.e. $Y_{0,0}(\cos\theta)$ and $Y_{2,0}(\cos\theta)$, before the MQDT-calculation is initiated. Rotational couplings, on the other hand, are currently not yet regarded in these calculations, although they have successfully been employed in previous treatments of the HD$^+$ angle-independent DR cross section [15, 16, 116] reproducing the rich structure in the measured DR rate coefficient [17, 117]. The ionic rotational excitation (assuming the vibrational ground state) is insofar only accounted for in the calculation of the angular dependence by the corresponding centrifugal distortion of the molecular potential curves [118], that is in the description of an effective potential which determines the vibrational wave functions.

The calculated angular dependences for each ionic rotational state are convoluted over the electron energy distribution and properly normalized [114]. Subsequently, the experimentally deduced relative rotational state contributions are used to determine the final rotationally averaged result at a selected electron detuning energy. Two examples are shown in Fig. 4.17.

Overall the theoretical results [114] support the sensitivity of the angular dependence
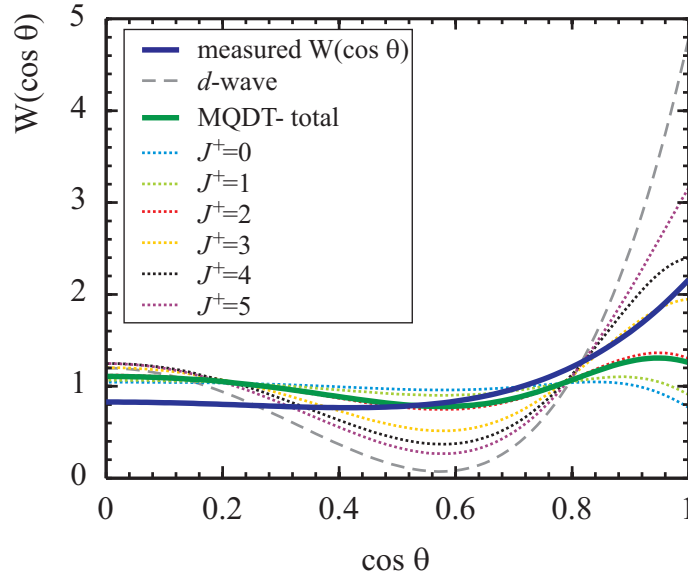
Figure 4.18: The measured fragment angular distribution (thick, blue line) is compared to the result of the MQDT calculation in the axial-recoil approximation [114] (solid green line) at 31 meV. The individually normalized J^+-contributions of the total MQDT-result are shown separately (dotted lines) as well as the angular dependence expected for a pure d partial-wave induced fragmentation (dashed, gray line).

on the electron collision energy observed in the experiments. The obtained theoretical emission patterns find within the axial-recoil approximation reasonable agreement with the data at selected energies (Fig. 4.17(b)), but partly predict too large anisotropies (Fig. 4.17(a)) which are not reproduced by the measurement. This can again indicate the need to expand the treatment beyond the axial-recoil approximation in order to properly account for fast rotations of the molecular ion or the neutral intermediate resonant state compared to the dissociation or resonance lifetime.

A decomposition of the calculated angular distributions into the individual rotational state components reveals a strong variation of the individual fragment angular distributions. In Fig. 4.18 the normalized J^+-state angular distributions are compared to the rotationally averaged fragment angular distribution as well as the measurement at 31 meV electron collision energy. The lowest two rotational states, found most abundant in the measurement, are closely associated with an isotropic emission indicating a strong s-wave coupling to the $J^+ = 0$ and 1 states of the HD^+ ion at 31 meV electron collision energy. In contrast, for high rotational quantum numbers the anisotropy increases towards a pure d-wave induced interaction, clearly overestimating the measured angular distribution. Generally, the rotationally averaged MQDT-result resembles a more isotropic dependence and is less

influenced by the computed large anisotropies associated with fast rotating molecular ions when considering the experimentally obtained J^+-state fractions.

4.3.3   Beyond the axial-recoil description

The previously presented theoretical studies on the fragment angular distributions rely on the validity of the axial-recoil approximation. This assumption is required in order to reveal directly from the experimental results the electronic symmetries of the molecular states as well as those of the coupled electron partial waves involved in the electron induced breakup process. In general, the applicability of the axial-recoil approximation in molecular dissociation processes implies either steep dissociative potential surfaces or long rotational periods compared to the lifetime against dissociation [40, 41] (see also Sec. 2.2.1). Studies of fragment angular distributions induced by photodissociation or dissociative electron attachment [32, 43, 44, 45, 119] have shown that the necessary conditions are not always satisfied and can result in a considerable reduction of the observed anisotropies. Thus the validity of the slow-rotation approximation in the current case, the DR of HD$^+$, should carefully be verified at this point.

Comparing the deduced anisotropy coefficients a_l with the rotational state fractions b_{J^+} one finds that high contributions of fast rotating molecules, i.e. low $J^+ = 0$ and 1 fractions b_{01}, seem to correlate with reduced anisotropy coefficients a_l approaching isotropic values (see Fig. 4.11). This possibly gives a first indication for a breakdown of the axial-recoil conditions. In addition, the deduced large s-wave amplitudes contrary to the predictions, on the one hand, and the generally exaggerated anisotropies found by the MQDT calculations compared to the measurements, on the other hand, might also be explained in view of a possible violation of the slow-rotation assumption in the present studies on the HD$^+$ ion.

The low-energy DR of HD$^+$ is dominated by interference effects between the two dissociation pathways, the direct and the indirect process. While dissociation along the direct route is expected to be fast, the resonant formation of an intermediate ro-vibrationally excited Rydberg state in the indirect reaction path can impose a delay in the dissociation process.

Typical dissociation times along the direct path are roughly estimated from the vibrational frequency ($\sim 10 \times 10^{-15}$ s) and found considerably faster than the classical rotational period T_{J^+}

$$T_{J^+} = \frac{1}{2\,c\,B_{v^+=0}\sqrt{J^+(J^+ + 1)}} \quad \sim \quad \frac{0.8 \times 10^{-12}\,\mathrm{s}}{\sqrt{J^+(J^+ + 1)}} \tag{4.15}$$

of the HD^+ ion in the lowest rotational levels J^+ (c - speed of light; $B_{v^+=0}$ - rotational constant of the HD^+ vibrational ground state). This has been estimated from the rotational energy given by [22]

$$\frac{1}{2}I\omega^2 = J^+(J^+ + 1)hcB_{v^+=0} \tag{4.16}$$

which yields after replacing the moment of inertia I by $h/(8\pi^2 cB_{v^+=0})$ the classical rotational frequency ω

$$\omega^2 = J^+(J^+ + 1)16\pi^2 c^2 B_{v^+=0}^2 \tag{4.17}$$

with the Planck constant h. Hence, reductions of the obtained anisotropy are less likely to be expected for the direct DR.

It is thus in particular the indirect dissociation pathway where the conditions for the axial-recoil approximation are possibly violated depending on the lifetime of the resonance τ_r compared to the rotational period T_{J^+}. From the observed narrow structures in the DR rate coefficient (Fig. 4.11(a)) a typical natural resonance width $\Gamma_r \sim 3$ meV can be estimated corresponding to a mean resonance lifetime of $\tau_r \sim 0.2$ ps ($\tau_r = \hbar/\Gamma_r$) [21]. This has to be contrasted to the rotational period $T_{J'}$ of the rotational state J' characterizing the intermediate HD^+ ion core of the resonantly formed Rydberg state. Approximated by the rotational period in Eq.(4.15), the molecular axis is indeed found to exhibit even for the lowest rotationally excited Rydberg resonances a considerable change in orientation before the molecular compound dissociates.

The range of rotational states accessible in the formation of the resonance is limited through conservation of the total angular momentum to $|J' - J^+| \leq 2l$ [16] for a coupled partial wave l of the incoming electron and an initial ionic state J^+ (see also Sec. 2.3). Hence, the deduced HD^+ J^+-level contributions b_{J^+} allow a rough estimate on the range of rotational quantum numbers which determine the rotational period of the resonance. While s-wave coupling will preserve the ionic rotational period in the resonance, fast rotating intermediate states may become accessible even for slow rotating HD^+ ions once the d-wave coupling is strong ($|J' - J^+| \leq 4$). Consequently, the conditions for the axial-recoil approximation also have to be checked for DR resonances associated with predominant $J^+ = 0$ and 1 initial HD^+ ion states.

An estimate for the expected attenuation of the anisotropy in the breakdown of the axial-recoil approximation can be given utilizing a semiclassical model [43] initially introduced to describe higher-order effects in the fragment angular emission of photodissociated molecules. The comparable dissociation dynamics allow to apply the approach also here in order to yield correction factors for predicted angular distributions, following also the ideas given in [44].

In this model [43], a Poisson distribution is used to describe the dissociation probability of the molecule after a time t from the capture of the electron. Depending on the molecular rotation frequency ω and the lifetime τ against dissociation, the probability $D(\theta_0)$ for fragments dissociating at an angle θ_0 relative to the initial axis orientation is given by [43]:

$$D(\theta_0)d\theta_0 = \frac{d\theta_0}{\omega\tau} \left[\frac{e^{-\theta_0/\omega\tau} + e^{(\theta_0 - 2\pi)/\omega\tau}}{1 - e^{-2\pi/\omega\tau}} \right]. \tag{4.18}$$

Any subsequent rotation of the emission direction is neglected as it is assumed that the rotation ceases due to the large kinetic energy of the fragments and the simultaneous fast separation [43]. The angular dependence for *instantaneous* fragmentation, expressed here by even Legendre polynomials, is then modified by the dissociation probability $D(\theta_0)$ at rotation angles θ_0 and yields the *attenuated* fragment distribution $W(\theta)$ [44]:

$$W(\theta, \omega, \tau) = K(\omega, \tau) \sum_{l \text{ even}} \chi_l(E_d)\tilde{a}_l P_l(\cos\theta) \cdot \int_0^\pi \left[e^{-\theta_0/\omega\tau} + e^{(\theta_0 - 2\pi)/\omega\tau} \right] \cdot P_l(\cos\theta_0)d\theta_0 \tag{4.19}$$

where $K(\omega, \tau) = [\omega\tau(1 - e^{-2\pi/\omega\tau})]^{-1}$, $\tilde{a}_l$ are the Legendre coefficients and $\chi_l(E_d)$ the convolution factors taking the electron velocity distribution into account (Eq.(4.11)). The integration over the angle θ_0 is evaluated term by term in closed form for the 0th, 2nd and 4th order Legendre polynomials and determines the attenuation factors $\gamma_l(\omega, \tau)$:

$$
\begin{aligned}
\gamma_0(\omega, \tau) &= 1 \\
\gamma_2(\omega, \tau) &= \frac{1 + (\omega\tau)^2}{1 + 4(\omega\tau)^2} \\
\gamma_4(\omega, \tau) &= \frac{1 + 10(\omega\tau)^2 + 9(\omega\tau)^4}{1 + 20(\omega\tau)^2 + 64(\omega\tau)^4}.
\end{aligned}
$$

$$\tag{4.20}$$
$$\tag{4.21}$$

The fragment angular distribution $W(\theta, \omega, \tau)$ is thus expressed by

$$W(\theta, \omega, \tau) = \sum_{l=0,2,4} \gamma_l(\omega, \tau)\chi_l(E_d)\tilde{a}_l P_l(\cos\theta) \tag{4.22}$$

so that the measured anisotropy coefficients (a_2, a_4) are related to those for instantaneous fragmentation through

$$
\begin{aligned}
a_2 &= \gamma_2(\omega, \tau) \cdot \chi_2(E_d) \cdot \tilde{a}_2 \\
a_4 &= \gamma_4(\omega, \tau) \cdot \chi_4(E_d) \cdot \tilde{a}_4.
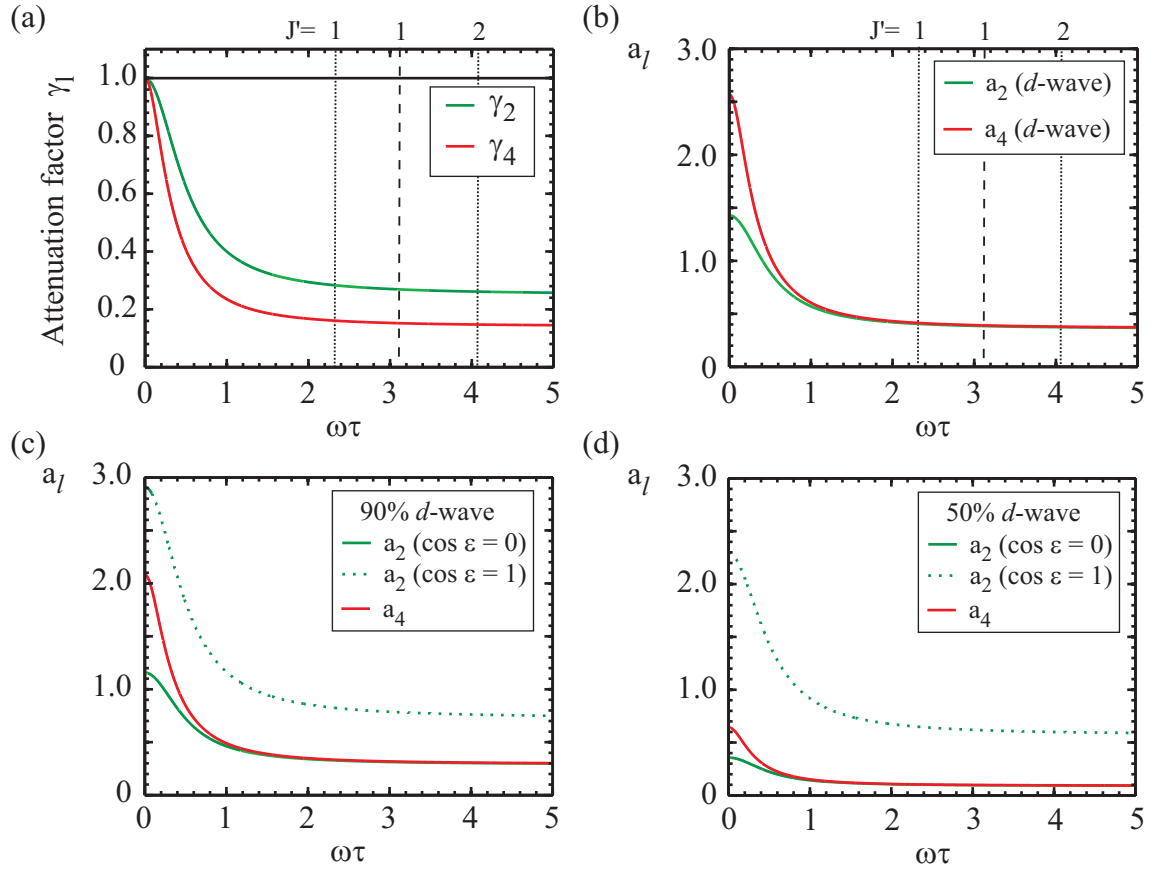\end{aligned}
$$

$$\tag{4.23}$$
$$\tag{4.24}$$

Figure 4.19: (a) The angular attenuation factors γ_l are given as a function of the product $\omega\tau$ between the rotational period ω and the lifetime against dissociation τ. In windows (b, c, d) the attenuation factors are applied as a function of $\omega\tau$ to the anisotropy coefficients $a_l = \gamma_l(\omega\tau)\tilde{a}_l$ of fragment angular distributions corresponding to a (b) pure d-wave ($\tilde{a}_2 = 10/7$ and $\tilde{a}_4 = 18/7$), (c) 90% relative d-wave amplitude (with 10% s-wave) and (c) 50% relative d-wave amplitude (with 50% s-wave). The a_2 coefficients are given in (c, d) for relative s and d phases of $\cos\epsilon = 0$ (solid green line) and 1 (dotted green line). Assuming $\tau = 0.2$ ps, the vertical dotted lines mark the values $\omega_{J'}\tau$ corresponding to rotation of a molecular system in state $J' = 1$ and 2 (HD$^+$ ion core). The dashed line corresponds to a H$_2^+$ ion core in the $v^+ = 0$ and $J' = 1$ state.

As a function of the product $\omega\tau$, which represents different delay times of the dissociation with respect to the rotational frequency, the attenuation factors $\gamma_l(\omega, \tau)$ are displayed in Fig. 4.19(a). The anisotropy is found to be reduced rapidly and represents already for $\omega\tau = 1$ only ~ 40 % (a_2) and ~ 20 % (a_4) of the initial value. Interestingly, in case of $\omega\tau \to \infty$ the attenuation factors γ_l approach a constant, *non-zero* value which implies that even for fast rotating molecules the anisotropy is not completely smeared towards

an isotropic distribution as recognized also in [44].

Utilizing this semiclassical model, the effects of molecular rotation during the fragmentation process can be studied on different initially undisturbed angular dependences. Three cases of s and d partial-wave couplings are compared in Fig. 4.19 (b, c, d) by applying the attenuation factor $\gamma_l(\omega\tau)$ as a function of $\omega\tau$ to the initially undisturbed Legendre coefficients $\tilde{a}_2$ and $\tilde{a}_4$: the pure d-wave coupling in inset (b), 90% relative d-wave amplitude in (c) and 50% relative d-wave amplitude in (d), latter two cases for relative s and d phase angles $\cos\epsilon = 0$ and 1. The Legendre coefficients a_2 and a_4 corresponding to the ones measured (use Eqs.(4.13, 4.23) and (4.14, 4.24) without the convolution factor $\chi_l(E_d)$) rapidly decrease within $\omega\tau \lesssim 1$ and approach a nearly constant value. In fact, one finds in case of a pure d-wave as well as in case of an incoherent superposition of both partial waves ($\cos\epsilon = 0$) nearly matching asymptotic values a_2 and a_4 for $\omega\tau \to \infty$. Any coherently interfering partial wave coupling, on the other hand, can be recognized by the measured 2nd order Legendre coefficient exceeding the value of a_4.

Assuming the resonant formation of an intermediate Rydberg state with a lifetime against dissociation of $\tau_r \sim 0.2$ ps (see above), one finds already for molecular compounds in the first rotationally excited state $J' = 1$ that at the corresponding value of $\omega\tau \approx 2.34$ the observed anisotropy coefficients are expected to be reduced by a factor of nearly ~ 3.5 (a_2) and ~ 6.2 (a_4) with respect to the initial dependence. In fact, the respective attenuation factors γ_l almost reach the asymptotic level so that additional effects for faster rotating molecules can be regarded as negligible. Consequently, the influence of rotational excitation on the reduction of the anisotropy can be treated in first order with the same attenuation factors γ_l, independent of the rotational state of the resonance for $J' > 0$.

The coefficients representing instantaneous fragmentation and thus the angular *dependence* of the dissociation process can then be inferred from the measured anisotropy coefficients a_2 and a_4 considering the attenuation factor γ_l. For the above suggested value $\gamma_4 = 0.16$ the relative d-wave amplitudes $|c_d|^2$ in the s and d partial-wave description are directly reflected by the measured a_4 values as a function of the detuning energy and are determined by $7a_4/(18\gamma_4 \cdot \chi_4)$. The accordingly deduced relative d-wave amplitudes are shown in Fig. 4.20(a). Their values are significantly enhanced compared to those determined *under* the axial-recoil approximation in Fig. 4.16(a). At some electron collision energies they even exceed the maximum possible value of unity, whereas in particular at low electron energies $E_d \lesssim 14$ meV the relative amplitudes partly remain below $\sim 50\%$.

Relative d-wave amplitudes exceeding a value of one are artificial and result from the applied attenuation factor γ_4. They *do not make sense* from a physics point of view, but they indicate that the assumed attenuation is too large. This can either be attributed to
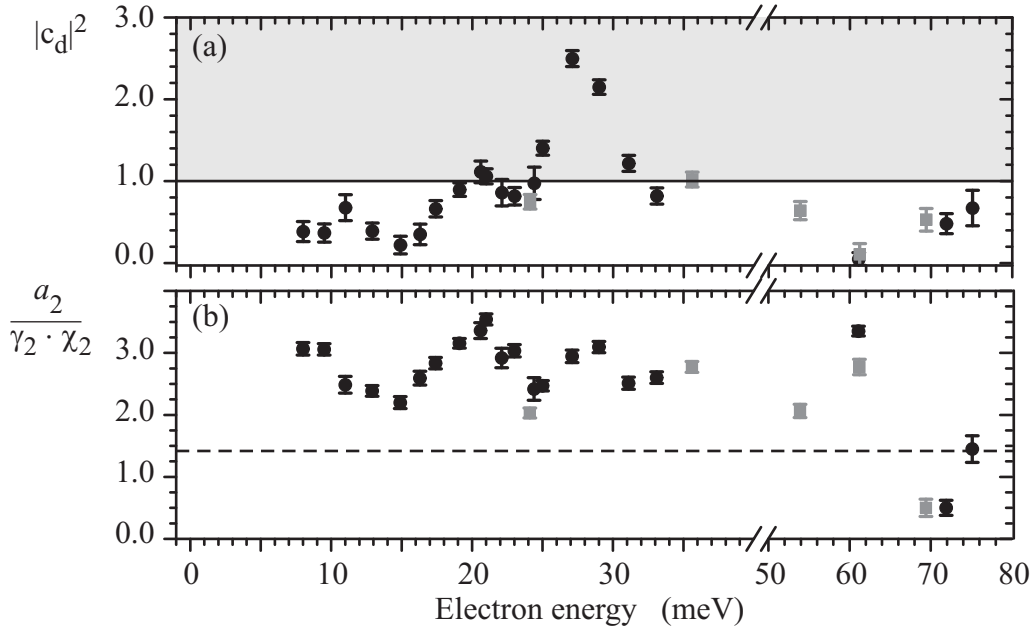
Figure 4.20: (a) The corrected relative d-wave amplitudes $|c_d|^2$ deduced from the measured a_4 coefficients according to Eqs.(4.14) and (4.24) are presented, associating the attenuation $\gamma_4(\omega_{J'=1}\tau)$ with rotation of the molecule in a $J' = 1$ intermediate state ($\tau = 0.2$ ps; see Fig. 4.19(a)). Note, values of $|c_d|^2 > 1$ (gray shaded area) are artificial and indicate that the applied γ_4 is too small (attenuation is estimated too strong). In window (b) the accordingly corrected a_2 coefficient is given, that is $\tilde{a}_2 = a_2/(\gamma_2 \cdot \chi_2)$. The dashed line represents the expected coefficient $\tilde{a}_2 = 10/7$ for a pure d-wave. (for symbols see caption of Fig. 4.11)

the neglected participating ground rotational state (which cannot be described at all by the semiclassical model; note that a strong $J^+ = 0, 1$ contribution is observed just in the range of 25 - 30 meV, see Fig. 4.11(b)), or to significantly faster dissociation times due to a smaller resonance lifetime or dissociation upon the direct DR pathway. Considering that the applied attenuation correction appears too strong, a pure d-wave coupling even seems in view of a breakdown of the axial-recoil approximation not likely. This is in particular underlined when regarding simultaneously the accordingly corrected a_2 coefficients in Fig. 4.20(b) which generally deviate from $\tilde{a}_2 = 10/7$ (dashed line), i.e. a pure d-wave coupling. Instead the measured a_2 and a_4 values rather comply with *interfering s and d* partial-waves ($\cos \epsilon > 0$), which is also stressed by the larger a_2 values compared to those found for a_4 in the measurements (compare the measured values in Fig. 4.14 with those expected according to the model in Fig. 4.19 (c,d)).

One can conclude that the effect of molecular rotation together with the concept of res-

onance delays can induce a significant reduction of the observed anisotropy and thus influence the deduced participating electronic symmetries. In particular the relative d-wave amplitudes can find in the treatment beyond the axial-recoil approximation an enhancement towards its predicted role in the DR of HD$^+$ [14]. Nevertheless, these results also stress the importance of the s partial-wave and find it to interfere with the d partial-wave in the DR process. Future theoretical models should thus incorporate the possibility to expand the treatment beyond the assumptions of the axial-recoil approximation, in particular for systems where the rotational period is of the same order as the typical lifetime against dissociation. This applies mostly to small molecular systems such as HD$^+$ where due to strong rotational coupling the indirect DR process plays an important role [120] and the dissociation can thus be considerably delayed.

4.4 Conclusions

On a dense energy grid reaching up to $\sim$75 meV electron collision energies the fragmentation kinematics of HD$^+$ ions have been studied through 2D and 3D fragment imaging in twin merged beam experiments at the TSR.

First, from the different amounts of kinetic energy release identified in the transverse distance distributions, the relative rotational state fractions were deduced as a function of the electron collision energy. In particular the lowest two rotational ionic states, $J^+ \leq 1$, revealed a strong energy sensitivity on a similar narrow scale as the rotationally averaged DR rate coefficient $\alpha_{DR}(E_d)$. These findings underline the importance of the ionic rovibrational state in the resonant electron capture.

Second, the obtained fragment angular distributions reflect within the axial-recoil limit the electronic symmetries involved in the electron capture process. Described by a sum of even Legendre polynomials ($l \leq 4$), anisotropies of 4th order were observed for the first time in DR experiments and are in fact in accordance with the predicted role of the d partial-wave in the electron capture. Both deduced anisotropy coefficients, a_2 and a_4, are found to be in general strongly different from zero and exhibit strong variations as a function of energy, again similar as the DR rate coefficient. However, within the axial-recoil approximation their amplitudes remain significantly smaller compared to the one expected for a pure d-wave and in addition rather large interfering s-wave fractions were deduced from a simple model, contrary to the predicted dominance of the d partial-wave. Indications for a possible breakdown of the assumed axial-recoil approximation are given and were in fact shown to possibly significantly reduce the initial anisotropies already for the first rotational excited resonant state, affecting the analysis of the partial wave

contributions.

At zero detuning energy the influence of the flattened Maxwellian electron velocity distribution on the fragment emission characteristics was studied. For electrons generated by the thermal cathode the slightly larger transversal electron velocity spread there in contrast to the electron beam emitted by the photocathode was sufficient to observe a small anisotropy in the fragmentation process as expected for an anisotropic electron velocity distribution even at a zero average velocity difference between the colliding particles.

State-selective DR of H_2^+

The process of dissociative recombination is found to be particularly sensitive on the internal excitation of the molecular ion. This has direct influence in environments where DR dominates the destruction of molecular ions, for instance in interstellar space [5, 6], but also often hinders the detailed comparison of theoretical and experimental studies since the internal excitations of the participating ions in the measurements remain unknown. Therefore, experiments are desired where molecular ions can be prepared in distinct ro-vibrationally selected states. In this chapter results are presented on the DR of H_2^+ ions which were produced in defined states by resonantly enhanced multiphoton ionization (REMPI). The focus will be on the fragmentation kinematics but also state-selective DR rate coefficients are discussed at low electron collision energies, where the strongest sensitivity on the ionic ro-vibrational state is expected.

5.1 Production of H_2^+ ions in defined states

State selective experiments have been driven in the past years by the aim to be able to yield through distinct comparisons with theory a better, if not even a complete understanding of the DR process. In particular, the unknown internal population of the investigated molecular ions often hindered a decomposition of the results into the respective contributions. The required independent probe of the ions' excitation state is not always available at experimental setups. One possible tool is the Coulomb-Explosion Imaging (CEI) technique [121], which enables in-situ measurements to infer the vibrational population of circulating ions in storage rings. It has been applied inter alia to deduce the absolute DR rate coefficients for H_2^+ and D_2^+ ions in the first six vibrational levels during earlier experiments at the TSR [68].

Other methods focus on influencing the population of the stored molecular ions, either

before injection or even during the storage period. For instance, the ro-vibrational distribution of the stored H$_2^+$ ions has been modified through depletion of high vibrational states in photodissociation, nevertheless still remaining with an ion ensemble in unknown excitation levels [9]. A different approach focuses on the development of ion sources in order to provide molecular ions in distinct excitations before injection, mostly providing rotationally cold molecular ions at temperatures below ∼50 K. In these experiments either a supersonic expansion source [122, 123] or buffer gas cooling in a radiofrequency multipole ion trap [124] have so far been employed to produce H$_2^+$ [123] and H$_3^+$ molecular ions in the lowest rotational states. While the infrared active H$_3^+$ ions reached in addition the vibrational ground state already by the time of injection into the storage ring, the vibrational population of H$_2^+$ could only be influenced through the subsequent interaction with electrons by super-elastic collisions (SEC; Eq.(4.5)).

The study of selected *excited* ion states, on the other hand, is generally impossible with molecules exhibiting a permanent dipole moment, such as H$_3^+$ or HD$^+$ ions. Their coupling to the ambient thermal background radiation will impede long observation times as the internal excitation will change. Instead ions lacking a permanent dipole moment are preferred. Once they can be produced in defined states already in the ion source experiments with ions in distinct, but arbitrarily excited states will become possible.

As will be discussed in the following, in standard ion sources molecular ions are generally created through electron impact ionization of a parent neutral molecule in a broad ro-vibrational state distribution and will thus not be suitable for state selective experiments if the population cannot be probed in-situ. To overcome this problem an ion source has been developed by a research group at the University of Louvain-La-Neuve which is based on the idea of resonantly enhanced multiphoton ionization (REMPI). It yields H$_2^+$ ions in selected vibrationally and rotationally excited states for storage ring experiments on DR. The concept of the ion source will briefly be described here but the reader is referred to [88] for more details.

5.1.1 Electron impact ion beam production

A common production method for molecular ions is electron impact ionization of the parent neutral molecule. Within the Born-Oppenheimer approximation the ionization process is described as an electronic transition which takes place instantaneously compared to the timescale of vibrations; complying with the Franck-Condon principle introduced in Sec. 2.1.2 (see also Fig. 5.1(a)). Accordingly, the transition amplitude from an initial neutral molecule in the vibrational state v to a vibrational state v^+ of the respective ion
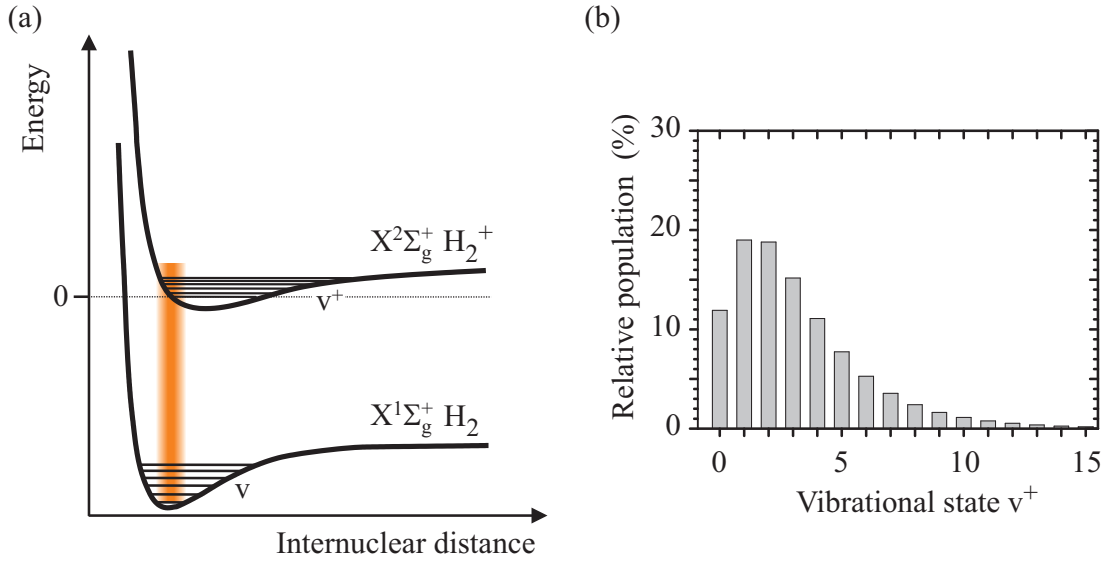
Figure 5.1: (a) Schematic drawing of the potential energy surfaces involved in the H$_2^+$ ion production from electron impact ionization of neutral H$_2$. The orange area reflects the vertical transition from the ground state of H$_2$ as expected from the Franck-Condon principle. (b) Typical broad vibrational state distribution of H$_2^+$ ions generated by electron impact ionization [125].

is proportional to the Franck-Condon factor (Eq.(2.1)). In case the potential energy surfaces exhibit their minima at the same internuclear distance R, transitions with $\Delta v = 0$ are favored. On the other hand, a displacement of the potential energy surfaces along the internuclear axis will induce large changes in the vibrational quantum number, as for instance expected for the hydrogen molecule. The initial vibrational population of the H$_2$ molecule is thus not reflected by the ion's excitation after ionization. Figure 5.1(b) illustrates an example of a measured vibrational state distribution of H$_2^+$ ions after electron impact ionization [125]. The range of vibrational states reaches with significant contributions up to at least $v^+ = 10$ and exhibits a maximum between $v^+ = 1$ and 2; clearly not suitable for state selective experiments.

In contrast to the deuterated hydrogen molecular ion HD$^+$, the H$_2^+$ ion lacks a permanent dipole moment so that long lifetimes ($\approx 10^6$ s [126]) of individual vibrational states are expected and radiative cooling is practically inhibited. Experiments at storage rings exhibit the possibility to merge cold electrons with the circulating molecular ions, which allows to induce vibrational cooling through super-elastic collisions (SEC). Through this method the initial broad vibrational distribution can efficiently be reduced to only a few vibrational states ($v^+ \lesssim 4$) within storage times of a few seconds (see, e.g. [11, 68]).

This cooling mechanism was also investigated under the current experimental conditions. Provided with an H_2^+ ion beam, which was produced in a standard Penning ion source and subsequently accelerated to a beam energy of $E_{beam} = 0.96$ MeV, SEC was employed by merging a velocity matched cold electron beam from the photocathode in the electron target section ($I_e \approx 0.481$ mA and $n_e \approx 1.5 \times 10^6$ cm^{-3}). The vibrational cooling was monitored through DR measurements at near-zero electron collision energies ($E_d = 0$ eV) with the fragment imaging detector. From the recorded transverse distance distributions the relative contributions $b_{v^+,1s,n}$ of each initial-to-final-state DR channel ($H_2^+(v^+ \leq 8, J^+) + e^- \rightarrow H(1s) + H(n)$; $n \geq 2$) were identified as a function of the storage time t by fitting Eq.(3.10) to the data. While assuming an isotropic dissociation ($a_{l>0} = 0$), contributions from initial rotational excitations of the ion were related through a Boltzmann distribution p_{J^+} (Eq.(4.4)) with free (for $t < 5$ s) temperature parameter T to each other (T was fixed after storage times $t > 5$ s to 250 K , the last unconstrained fitted value of T).

The results of the relative vibrational state fractions are summarized in Fig. 5.2 together with depicted examples of the measured transverse distance distribution. Within the first second after injection the initial vibrational excitation of the stored ions ($v^+ \geq 5$) is even sufficient to populate the next higher state of the final atomic products ($n = 3$), which is energetically not accessible at zero detuning energy from low ($v^+ < 5$) ionic vibrational states. The deduced ground state fractions at $t < 5$ s are most likely misinterpreted, even higher vibrational state contribution ($v^+ > 8$) which were not included as initial-to-final-state DR channels in the fitting routine. Moreover, the vibrational ground state fraction is not expected to be resolved at early storage times due to the low state specific rate coefficient [68]. Note also, that vibrational states $v^+ \geq 5$ populate predominantly the final state configuration with $n = 3$, which corresponds to the DR channel with the lower kinetic energy release. The high excitations reduce quickly so that after about 10 s the observed vibrational state fractions comprise only the lowest four states ($v^+ \leq 3$).

The current findings are in agreement with earlier experiments carried out at the TSR [68]. For those experiments the H_2^+ ion beam was produced by the single-ended Van-de-Graaff accelerator and injected at comparable ion beam energies (≈ 1 MeV) into the TSR. Using electrons from the electron cooler at slightly higher densities ($n_e \approx 6.1 \times 10^6$ cm^{-3}) they utilized the fragment imaging technique to extract the relative vibrational state fractions from recorded DR events as functions of the storage time. They report a similar time dependence of the deduced vibrational state fractions. In addition, they also studied the vibrational fractions of D_2^+ ions at long (> 60s) storage times, revealing almost complete relaxation to the vibrational ground state.
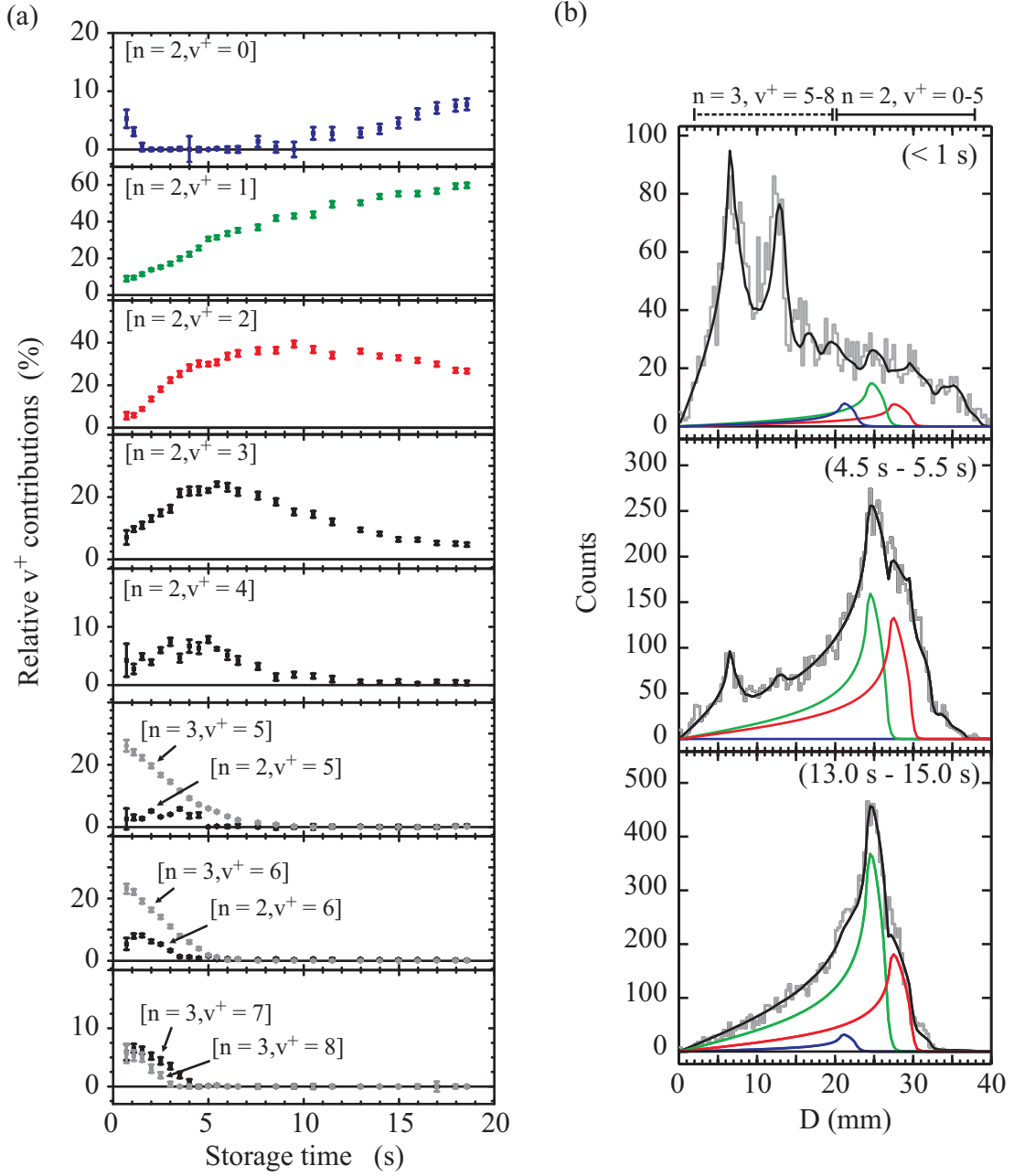
Figure 5.2: (a) The relative fractions $b_{v^+,1s,n}$ of H$_2^+$ DR channels from an ionic vibrational state v^+ into H(1s) + H(n) ([n,v^+], $n \geq 2$; color code see inset (b)) are compared as a function of storage time ($t = 0 - 20$ s) at $E_d = 0$ eV. The $b_{v^+,1s,n}$ were deduced from a fit to the measured transverse distance distributions. The H$_2^+$ ions were produced in a Penning ion source. (b) Depicted examples of the measured transverse distance distribution are shown for data within $t < 1$ s, $4.5 < t < 5.5$ s and $13.0 < t < 15.0$ s after injection. The line shapes for the $v^+ = 0$ (blue line), $v^+ = 1$ (green line) and $v^+ = 2$ (red line) channel are compared to the total fit result (black line) and the data (gray line).
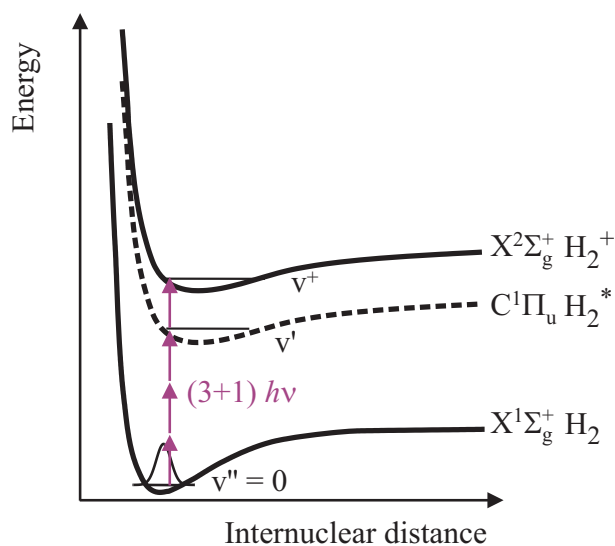
Figure 5.3: Schematic drawing of H_2^+ ion production in selected ro-vibrational states through $(3 + 1)$ resonantly enhanced multiphoton ionization (REMPI).

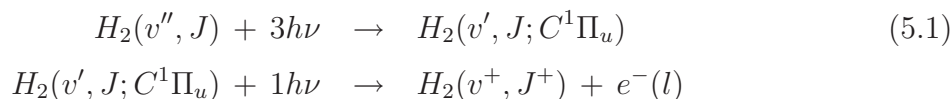## 5.1.2 The laser ion source (LISE)

The production of selected ro-vibrational states of H_2^+ ions is realized in a new type of ion source (named Laser Ion Source (LISE)) [88] which utilizes the technique of resonantly enhanced multiphoton ionization (REMPI).

Already more than 20 years ago the REMPI process has been suggested to afford the production of particular ion states through the selection of a specific ionization path (see e.g. [127, 128]). Briefly, the resonant multiphoton ionization process can be described by first promoting a molecule to an intermediate Rydberg state through the absorption of m photons before in the final step a single additional photon ionizes the molecule. Choosing an intermediate Rydberg state with a similar potential energy surface as the ionic state, the Franck-Condon factors (Eq.(2.1)) favor the preservation of the vibrational level v' of the Rydberg state, i.e. $\Delta v = v^+ - v' = 0$. In addition, rotational selection rules restrict in an $(m+1)$ REMPI process the production of diatomic ions to defined rotational levels [129].

H_2^+ ion production through $(3 + 1)$ REMPI

The photoionization of the H_2 molecule in a $(3+1)$ REMPI process via the $C^1\Pi_u$ Rydberg state has been proposed by S.T. Pratt and co-workers [127, 128, 130] (see Fig. 5.3):

$$H_2(v'', J) + 3h\nu \quad \rightarrow \quad H_2(v', J; C^1\Pi_u) \tag{5.1}$$
$$H_2(v', J; C^1\Pi_u) + 1h\nu \quad \rightarrow \quad H_2(v^+, J^+) + e^-(l)$$

They demonstrated in measurements of photoelectron spectra from excited $\text{C}^1\Pi_u$, $v' = 0 - 4$, $J = 1$ [127] levels that H$_2^+$ ions can be prepared in vibrationally selected states through multiphoton ionization. Depending on the vibrational level v' of the intermediate Rydberg state, ions are dominantly created in $\Delta v = v^+ - v' = 0$ transitions. Significant deviations from the Franck-Condon predicted populations were observed at increasing v' due to the dependence of the electronic transition matrix element on the internuclear distance, whereas for the lowest vibrational states, $v^+ \leq 1$, level populations with $\Delta v \neq 0$ did not exceed a few percent [127].

In these studies also the sensitivity of the ionization process on the rotational level was pointed out. From selection rules for three-photon excitation $\Pi \overset{3\,h\nu}{\longleftarrow} \Sigma^+$ seven rotational transitions are in principal allowed, labeled as N, O, P, Q, R, S, T and which correspond to $\Delta J = -3$ through $+3$. Three of those were observed in the experiments: the P, Q and R branches ($\Delta J = -1, 0, +1$).

Further detailed studies [128, 130] were able to resolve the rotational structure of these transitions in photoelectron spectra, paving the way for the production of rotationally and vibrationally selected H$_2^+$ ions. The underlying rotational selection rules for a $(3+1)$ ionization of H$_2$ $^1\Sigma_g^+$ via the C$^1\Pi_u$ can be understood when the ion plus the continuum electron are treated in Hund's case (d) coupling [22]; i.e. the photoelectron is completely decoupled from the molecular axis. The selection rules are thoroughly discussed in the respective articles [128, 129, 130], giving thus only a short summary at this point:

The schematic diagram in Fig. 5.4(a), which has been presented in [128, 130], illustrates the allowed ionization pathways following excitation through the R(0) and Q(1) transitions, i.e. the initial neutral molecule is in the $J = 0$ or 1 rotational state, respectively. Note, that in Fig. 5.4(a) J describes the total angular momentum.

Based on parity considerations the continuum electronic partial wave l must be even. In fact, only s and d partial-waves are taken into account, as higher orders are expected to yield a negligible contribution. The excitation by the absorption of three photons promotes the ground state molecule into the Π^- component for the Q-branch, and into the Π^+ component of the C$^1\Pi_u$ state for the R (or P)-branch transition. Subsequently, single-photon selection rules [22] apply to the ionization of the Π^- and Π^+ states:

- $\Delta J = 0, \pm 1$

- total parity $+ \leftrightarrow -$, $+ \not\leftrightarrow +$ and $- \not\leftrightarrow -$

- nuclear spin symmetry $s \leftrightarrow s$, $a \leftrightarrow a$ and $s \not\leftrightarrow a$

- electronic parity $u \leftrightarrow g$, $g \not\leftrightarrow g$ and $u \not\leftrightarrow u$
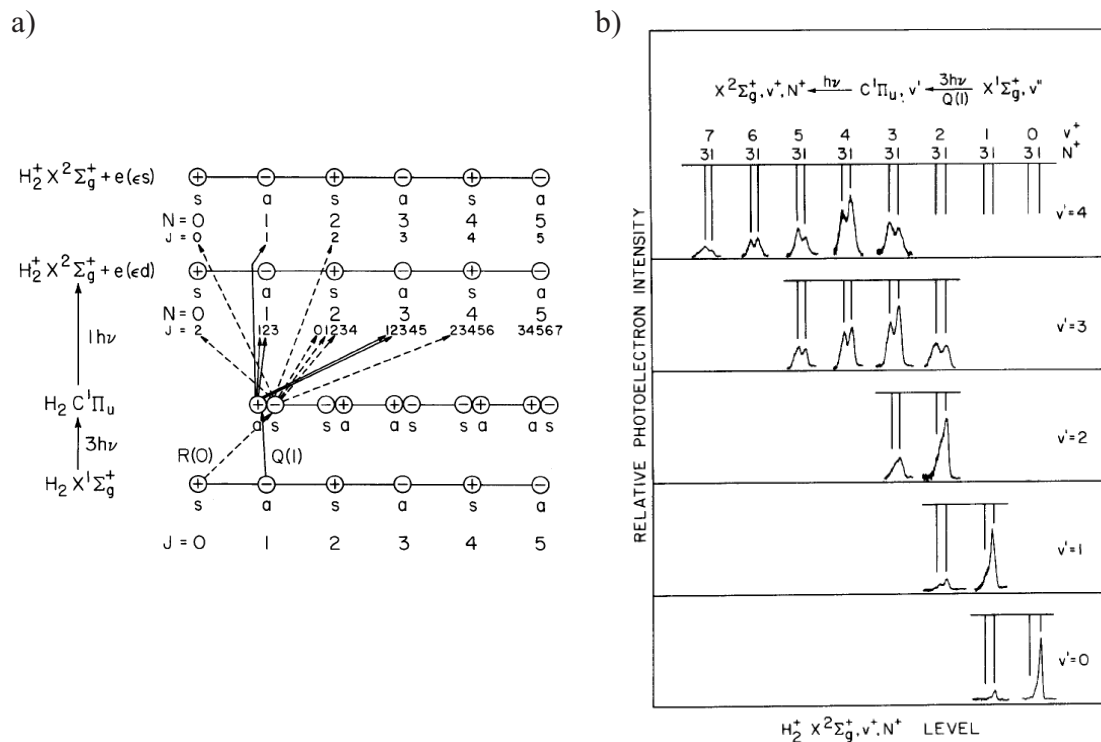
Figure 5.4: (a) Schematic diagram [128] of the allowed ionization transitions for $(3+1)$ REMPI of H_2 via the $C^1\Pi_u$ state. (b) Photoelectron spectrum measured for a three-photon resonant H_2 $C^1\Pi_u$, $v' \leftarrow X^1\Sigma_g^+$, $v'' = 0$, Q(1) transition [128].

yielding for the respective transitions different sets of rotational states in the H_2^+ ions. For the two cases presented here, only even ionic rotational levels are accessed from photoionization via R(0), whereas odd rotational levels are populated in the ion through the Q(1) path [129, 130].

Figure 5.4(b) shows a measured photoelectron spectrum for H_2^+ ions produced through the Q(1) transition from neutral molecules in the vibrational ground state [128]. The spectra convincingly demonstrate that molecular ions are only produced in the $N^+ = 1$ and 3 rotational states[1], in agreement with the selection rules. Furthermore, it can be noticed that the $N^+ = 1$ ionic rotations are predominantly created from low vibrational levels v' of the $C^1\Pi_u$ state. This opens up the possibility of selective H_2^+ ion production in distinct rotational and vibrational states. For the experiments presented in the following mainly Q-transitions via different vibrational levels v' of the $C^1\Pi_u$ state were chosen. Unfortunately, for the production of vibrational ground state ions the R(0) transition

---

[1]The ionic rotational state is labeled here by N^+ in contrast to the J^+ notation used throughout this chapter.

wavelength overlaps with the one corresponding to the R(1) transition [127]. Therefore, it was not possible to create ions both in the vibrational and rotational ground state through the (3 + 1) REMPI process at the high laser intensities applied in the current setup [131].

LISE setup and preliminary experiments

In the collaboration of the present experiment the H$_2^+$ ion production by LISE is realized through the above described (3 + 1) REMPI technique with an intense Nd:YAG laser, which is tuned to the selected transition (operating with $\sim$30 mJ close to $\sim$300 nm; the detailed properties depend on the selected ionization path [88]). The laser beam is focused below a nozzle for the H$_2$ gas inlet and the created ions can then be extracted through a series of electrodes [88]. Typically on the order of 1×10^6 ions are produced, yielding an ion current of $\leq$5 pA. Alternatively, ionization can be achieved by a filament through electron impact ionization which produces higher ion currents ($\sim$100 nA) and is thus favored for the adjustment of the extraction as well as the first acceleration stages. LISE was developed and optimized to yield an efficient ion production at the University of Louvain-La-Neuve, Belgium. Independent measurements utilizing dissociative charge exchange of H$_2^+$ ions with a Potassium jet thereby convincingly confirmed the dominant ($\sim$90%) creation of ions in a single vibrational state, in agreement with the photoelectron spectra in Fig. 5.4. A measurement resolving the ionic rotational excitations of the produced ions was not yet performed. In Table 5.1 the measured vibrational state populations of the H$_2^+$ ions are compared for the Q(1) transition via the $v' = 0$ or 1 vibrational state of H$_2$ C$^1\Pi_u$. Further details to these measurements together with additional wavelength dependent results can be found in [88].

In order to perform DR experiments at the TSR, LISE was temporarily installed at the HSI accelerator. The ions created in LISE are extracted and subsequently accelerated to 0.96 MeV in the RFQ accelerator before injection into the TSR. There they were optionally overlapped with electrons both in the electron cooler as well as the electron target (photocathode). At typical electron currents of I$_{target}$ = 0.92 − 0.98 mA ($n_e \sim$ 2.9×10^6 cm^{-3}) fragment imaging and DR rate measurements could thus be performed at selected detuning energies with an energy resolution similar to the one stated for the HD$^+$ measurements, i.e. characterized by $kT_\parallel \approx 0.03$ meV and $kT_\perp \approx 0.5$ meV.

The ro-vibrational population of the injected and circulating ions were monitored through DR induced breakup events by the fragment imaging setup as a function of storage time. For this purpose the electron beam in the electron target section was accelerated to the

Table 5.1: The measured vibrational state (v^+) populations of H_2^+ ions produced through Q(1) transitions via the v'= 0 or v'= 1 vibrational state of H_2 $C^1\Pi_u$ [88].

Ionization path	Vibrational state v^+	Measured population (%)
302.35 nm (Q(1),v'=0)	0	91.0 ± 1.2
	1	8.6 ± 0.9
	2	0.4 ± 0.9
295.85 nm (Q(1),v'=1)	0	8.4 ± 1.5
	1	85.9 ± 1.9
	2	5.7 ± 1.5

velocity, which matches the one of the circulating ions, i.e. tuned to $E_d = 0$ eV. From the obtained transverse distance distributions the different amounts of kinetic energy release could be identified to yield the relative contributions $b_{v^+,J^+,1s,2}$ of initial-to-final-state DR channels (Eq.(3.10)). Since the ion production in LISE was restricted to low vibrational states $(v^+ < 3)$, the final atomic product state configuration was limited to H(1s) + H(2). Therefore, the obtained transverse distance distributions can only differ by the ro-vibrational state distribution of the stored ions and allow direct comparison between different ionization pathways and storage times. In particular, the high spatial resolution of the detection system enables the identification of contributions down to the rotational level.

The vibrational populations of H_2^+ ions produced through the Q(1) (v'= 1) transition, were monitored accordingly as a function of storage time. The results are presented in Fig. 5.5. In this storage time period the time dependence of the vibrational state fractions is markedly different to the one for ions from a standard ion source, as presented in Fig. 5.2 earlier.

Within the first two seconds after injection, the recorded data comply with the dominant vibrational *and* rotational ionic state contribution as the close-up view of Fig. 5.5(b) in Fig. 5.6 reveals. In Fig. 5.6 the obtained distribution is compared at large transverse distances to different model functions $F_{v^+=1,J^+=1,3}(D)$, which correspond to $J^+ = 1$ and 3 ionic rotational states in $v^+ = 1$, respectively. Although, based on the selection rules, the ionization can yield both $J^+ = 1$ and 3 ionic excitation levels, the data comply with a dominant $(v^+ = 1, J^+ = 1)$ - fraction shortly after injection. This agrees with the results of the photoelectron spectra [128] shown in Fig. 5.4.
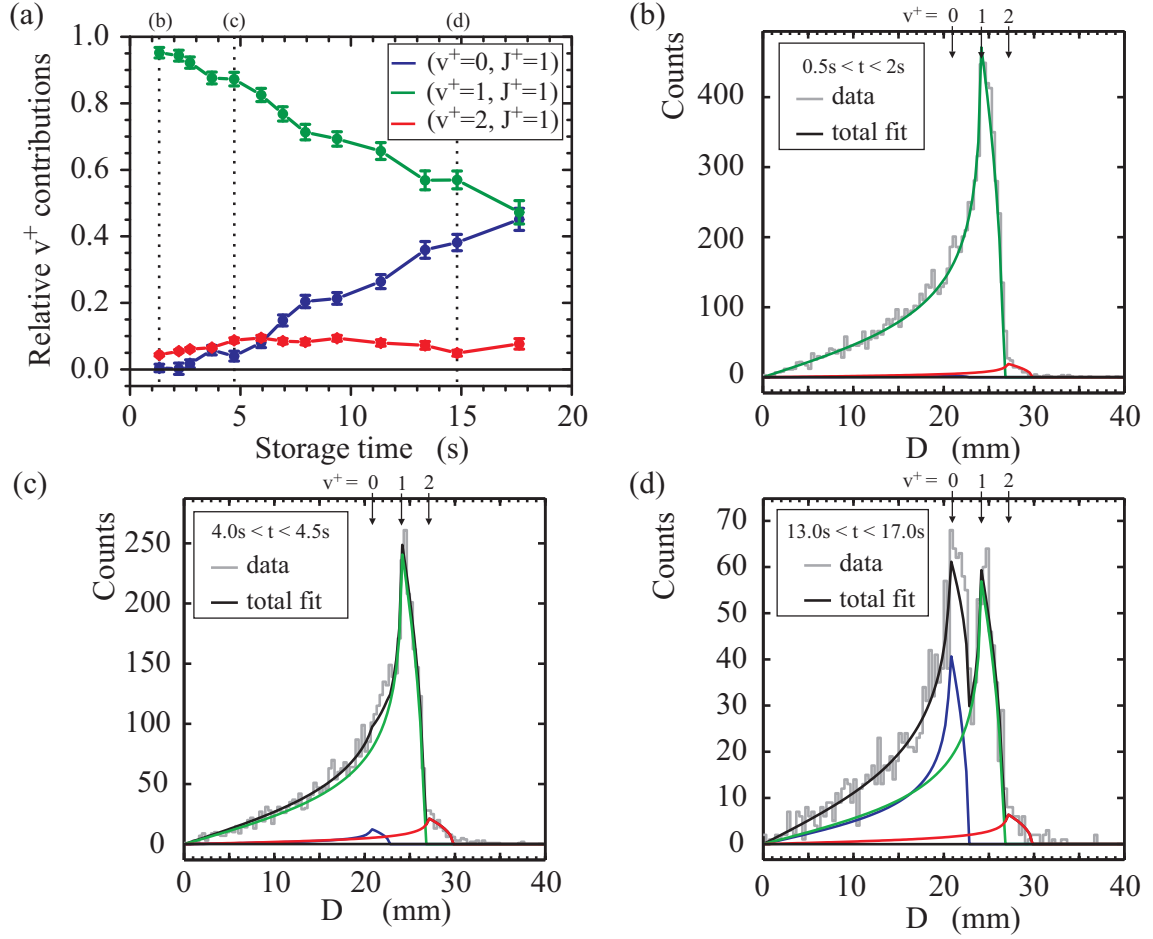
Figure 5.5: (a) As function of storage time the ionic ro-vibrational state contributions (v^+, J^+) are extracted from the recorded transverse distance distributions of H_2^+ ions produced in a Q(1) transition from the $v' = 1$ $C^1\Pi_u$ Rydberg state. Samples of measured transverse distance distributions are taken at three different storage times (see marks in (a)) and are displayed in windows b, c and d. The data are shown together with fitted model functions of the respective ionic state contributions (color code resembles the one in inlet (a)).

Applying the velocity matched electron beam over an extended period to the circulating ions, induces vibrational cooling through SEC. This affects the state populations and is reflected by the rapidly enhancing ground vibrational state fraction in the transverse distance distributions (Fig. 5.5). After $\sim$18 s the lowest two v^+ state contributions have reached an equal level in the recorded DR events.

Also note the nearly constant number of events associated with large transverse distances exceeding the expected kinetic energy release (KER) of $(v^+ = 1, J^+ = 1)$-ions. Their
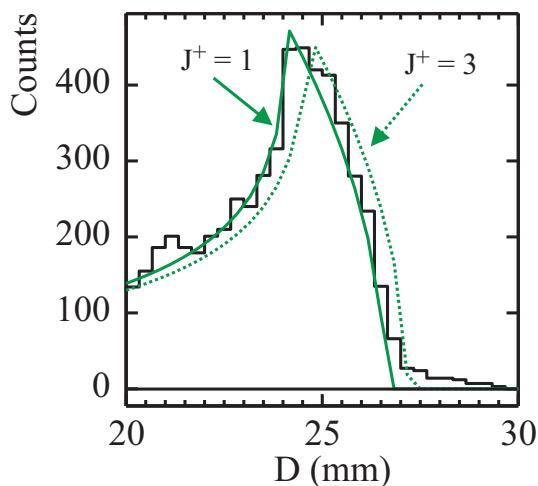
Figure 5.6: The measured fragment distance distribution (black line) for ions produced in the $v^+ = 1$ vibrational state through a Q(1) transition is compared to model functions $F_{v^+=1,J^+=1,3}(D)$ expecting either a pure $J^+ = 1$ (solid green line) or $J^+ = 3$ (dotted green line) ionic state contribution.

KER resembles closely the one for $v^+ = 2$ ions, which in fact exhibit a small initial population in the ion source (Table 5.1). Considering a similar SEC cooling time as for the $v^+ = 1$ ions [68], fractions originating from $v^+ = 2$ ions should rapidly approach a negligible amount within the first seconds after injection, contrary to the observation. On the other hand, coincident background events are excluded to cause these events due to the good beam quality, so that they probably originate from ions exposed to an efficient ro-vibrational heating process or from DR induced molecular breakups in the toroidal sections of the electron target. Despite of their origin, their relative contribution hardly exceeds a few percent and is thus treated as an $v^+ = 2$ ionic fraction in the following analysis. Since explicit measurements on $v^+ = 2$ ions were not performed, the angular distribution of the $v^+ = 2$ fraction is taken to be isotropic although a possible anisotropy cannot be excluded at non-zero collision energies.

The here presented vibrational state contributions reflect both the population of the stored ions as well as the state specific DR rate coefficients. Earlier measurements [68] have shown that in particular the $v^+ = 1$ rate is ~10 times larger than the one for $v^+ = 0$ ions at near-zero electron collision energies, thus severely influencing the measured state fractions of DR events.

Consequently, DR measurements with ions produced via the $v' = 0$ C$^1\Pi_u$ Rydberg state will yield only a restricted state selectivity; small $v^+ = 1$ populations from the ion source will significantly contribute to the recorded DR events. Figure 5.7 illustrates an example for a measurement employing the Q(1) ($v' = 0$) ionization pathway. Although the independent measurements on dissociative charge exchange (see Table 5.1) as well as the photoelectron spectra in Fig. 5.4 have found a dominant $v^+ = 0$ population, almost equal level fractions are deduced from the recorded DR events. Employing vibrational cooling
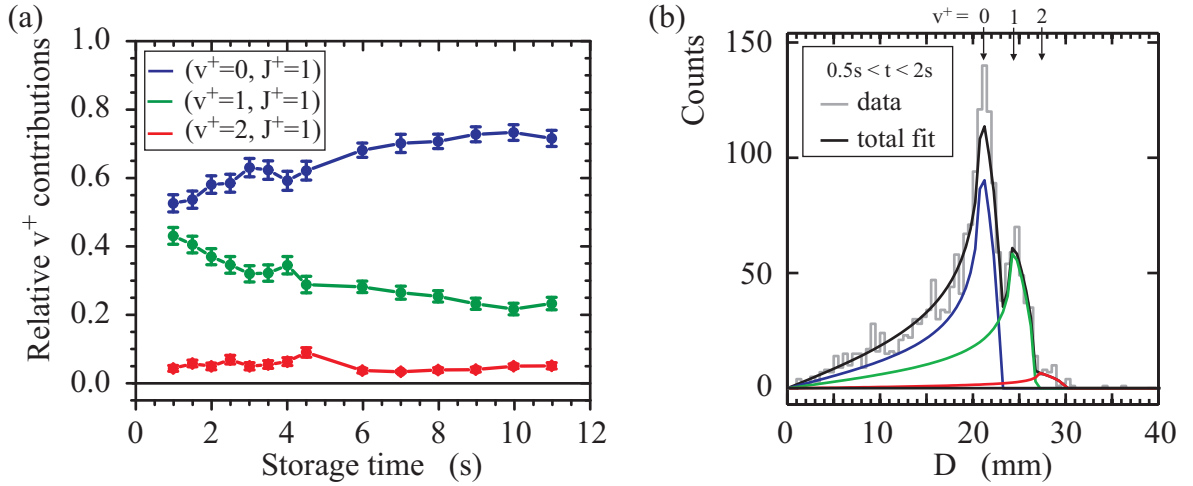
Figure 5.7: (a) As function of storage time the ionic ro-vibrational state contributions (v^+, J^+) are extracted from the recorded transverse distance distributions of H_2^+ ions produced in a $Q(1)(v' = 0)$ transition. The measured transverse distance distribution averaged over the events recorded between 0.5 s and 1.5 s after injection is displayed in (b) together with fitted model functions of the respective ionic state contributions (color code resembles the one in inset (a)).

through SEC will enhance the $v^+ = 0$ population. Nevertheless, the $v^+ = 1$ contribution will have to be taken into account accordingly in the analysis, in particular in vibrationally averaged DR rate measurements, where the vibrational state fractions are not identified.

5.2 State selective measurements

Taking advantage of the ro-vibrational state selectivity provided by the H_2^+ ion production in LISE, this opens up the possibility to study both the DR rate and the fragmentation kinematics of distinct ionic state configurations. Hence, a range of REMPI ionization pathways has been scanned providing ions in the lowest two vibrational states ($v^+ = 0, 1$) and their first three excited rotational levels ($J^+ = 1, 2, 3$) for the present experiments. The configurations are summarized in Table 5.2. The present work will concentrate on the results obtained on the fragmentation dynamics but will start out by presenting the measured DR rate coefficients.

Table 5.2: Summary of the REMPI transitions employed to yield selected ionic ro-vibrational state configurations for DR rate (marked by ∘) and fragment imaging (marked by ×) experiments.

Transition	vibrational state	
(dominant J^+)	$v' = 0$	$v' = 1$
Q(1) ($J^+ = 1$)	(∘; ×)	(∘; ×)
Q(2) ($J^+ = 2$)	(∘)	(∘; ×)
Q(3) ($J^+ = 3$)	(∘)	(∘; ×)

5.2.1 DR rate coefficients of selected ro-vibrational states

The DR rate coefficient $\alpha_{DR}(E_d)$ was measured as a function of the electron detuning energy E_d independently for H_2^+ ions produced via the lowest two vibrational ($v' = 0, 1$) $C^1\Pi_u$ Rydberg states in Q(1), Q(2) and Q(3) transitions, i.e. expecting to dominantly find $J^+ = 1$, 2 and 3 ionic states, respectively. After combined phase-space cooling of the ion beam by electrons generated both in the electron cooler and the electron target the measurements were restricted to storage time cycles of $\lesssim 5$ s. Thereby the data acquisition followed the general procedure common in DR rate measurements at the TSR [17] as briefly also introduced in Sec. 4.2, i.e. implied fast switching of the electron velocity within consecutive steps lasting ~ 50 ms between the measurement and the reference value used for a relative normalization. The final analysis comprises, among others, corrections for event contributions stemming from electron-ion collisions in the toroidal section of the electron target. The analysis then yields the DR rate characterizing ions created through the selected ionization path.

Preparing H_2^+ ions through the REMPI ionization process via $v' = 0$ $C^1\Pi_u$ causes in addition to the dominant $v^+ = 0$ also a small $v^+ = 1$ (8.6 %) ionic state population of the stored ions; accordingly the $v' = 1$ ionization path prepares also $v^+ = 0$ ions (8.4 %; see Table 5.1), whereas the $v^+ = 2$ contribution is neglected in the following. Additional minor rotational state fractions populated in the ion production will also be neglected. The measured DR rate

$$\alpha_{DR}^{(\bar{v}, J^+)}(E_d) = \sum_{v^+} p_{v^+}\, \alpha_{DR}^{(v^+, J^+)}(E_d) \tag{5.2}$$

thus reflects a superposition of vibrational states, instead of a pure v^+ rate coefficient (indicated by $\bar{v}$). Therefore $\alpha_{DR}^{(\bar{v}, J^+)}$ has to be decomposed according to the vibrational
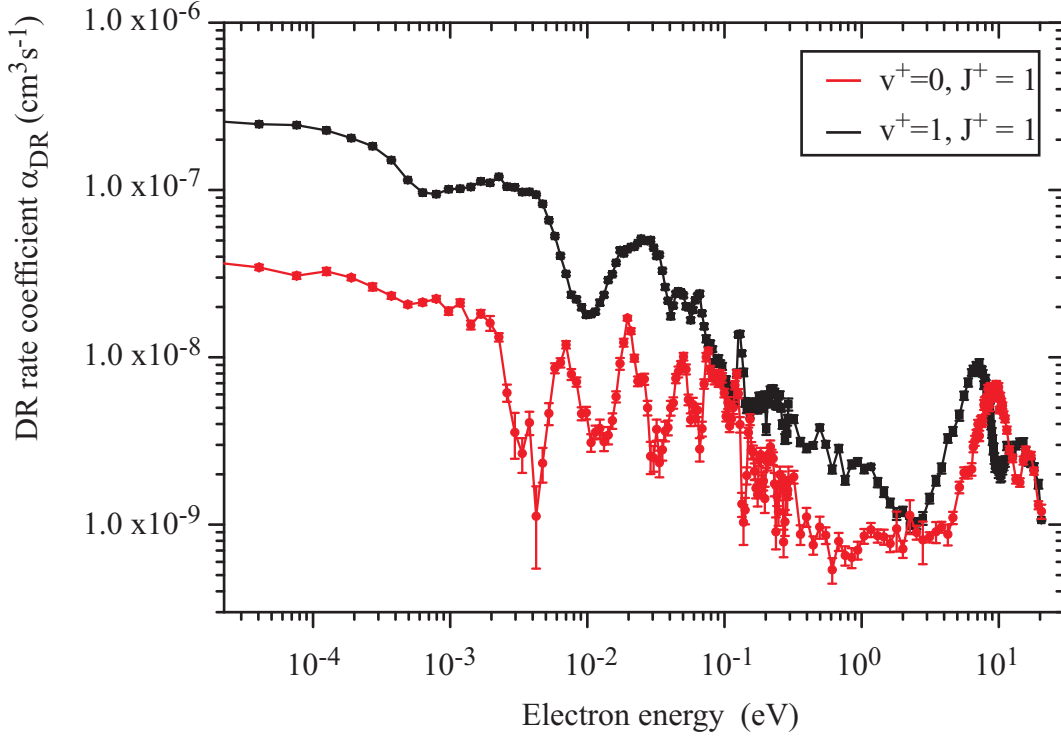
Figure 5.8: Decomposed DR rate coefficients $\alpha_{DR}^{(v^+, J^+=1)}$ for $v^+ = 0$ (red solid line) and $v^+ = 1$ (black solid line) ions in the $J^+ = 1$ rotational state [88].

populations p_{v^+} in order to yield the individual components $\alpha_{DR}^{(v^+, J^+)}(E_d)$ as a function of the detuning energy E_d. Knowing the vibrational state populations p_{v^+} of the stored ions (assume the ones from Table 5.1) and the relative vibrational state contributions of the DR events $((p_{v^+} \cdot \alpha_{DR}^{(v^+, J^+)})/\alpha_{DR}^{(\bar{v}, J^+)})$ deduced by fragment imaging measurements, the individual rates can be decomposed from the recorded total signals $\alpha_{DR}^{(\bar{v}, J^+)}$ at a fixed detuning energy E_d. Subsequently this allows to extract $\alpha_{DR}^{(v^+, J^+)}(E_d)$ from the measured total signals $\alpha_{DR}^{(\bar{v}, J^+)}(E_d)$ as a function of the detuning energy as described in [88].

This procedure has been applied for each rotational state J^+ in order to yield the individual ro-vibrational DR rates $\alpha_{DR}^{(v^+, J^+)}(E_d)$. The absolute DR rate cannot be determined since the ion current of the stored ions was too low for the diagnostic tools at the TSR. Instead the decomposed DR rate coefficients were scaled to $\alpha_{DR}^{(v^+=0, J^+)}$ which itself was normalized to the well measured $v^+ = 0$ HD$^+$ DR rate at 9 eV [10]. The resulting decomposed DR rates for H$_2^+$ ions in the rotationally first excited state ($J^+ = 1$) of $v^+ = 0$ and 1 are compared in Fig. 5.8.

Low-energy H_2^+ DR resonances for selected ionic states

Focusing on the low-energy range where the strongest influence of initial ionic rotational states is expected, the decomposed scaled DR rates ($\tilde{\alpha}_{DR} = \alpha_{DR}^{(v^+, J^+)} \sqrt{E_d}$), of the $v^+ = 0$ and 1 ionic vibrational and the first three excited rotational states ($J^+ = 1, 2, 3$) are presented in Figs. 5.9 and 5.10, respectively. Thereby, the low-energy resonant structures are particularly accentuated by this representation which reduces their comparison to a discussion independent from the general inverse proportionality on the detuning energy associated with the cross section of the direct DR process.

The decomposed DR rates find in agreement with earlier measurements and theoretical predictions [11, 123] an enhancement of the $v^+ = 1$ rate coefficient at low detuning energies compared to the one associated with the ground vibrational state (see also Fig. 5.8). Moreover, these measurements reveal pronounced energy dependent structures which characterize the DR rate of a distinct ro-vibrational state of the H_2^+ ion. Note that the resonant character not only change for different vibrational states, but also show distinct features connected to the ionic *rotational* level. These appear both as a local reduction but also as an enhancement of the DR rate at specific electron energies. Only at selected electron collision energies similar features can be pointed out for different ionic channels. For instance, in the vicinity of $E_d \sim 7$ meV the vibrational ground state ions exhibit a peak-like structure which coincides with a local reduction of the $v^+ = 1$ DR rates for all three rotational states.

The variations of the DR rate coefficients are associated with the formation of intermediate Rydberg states through resonant electron capture by the ion. They are observed with comparable strength and frequency for both the $v^+ = 0$ and 1 ions, suggesting a similar importance of the indirect DR mechanism for both initial ionic states.

Below the electronic ground state $^2\Sigma_g^+$ of the H_2^+ ion an infinite series of Rydberg states converges to the ionization limit. The capture of an electron into one of these Rydberg states is limited by total angular momentum conservation between the continuum and resonant state. This imposes selection rules for the formation of resonances which are determined by $|\Delta J| = |J' - J^+| \leq 2l$ [16], where J' is the rotational excitation of the Rydberg state and l the partial wave of the incident electron. For H_2^+ the contributing partial waves are s and d, i.e. $l = 0, 2$ (see also Sec. 4.3.1), so that the change of the rotational quantum number by the electron capture is restricted to $|\Delta J| \leq 4$ and ΔJ even due to the symmetry, still remaining with a large number of accessible states.

Hence, in Figs. 5.9 and 5.10 only the limits of Rydberg series associated with $\Delta J = 2, 4$ and $\Delta v = |v' - v^+| = 0$ are marked by the lines. There are more Rydberg series corre-
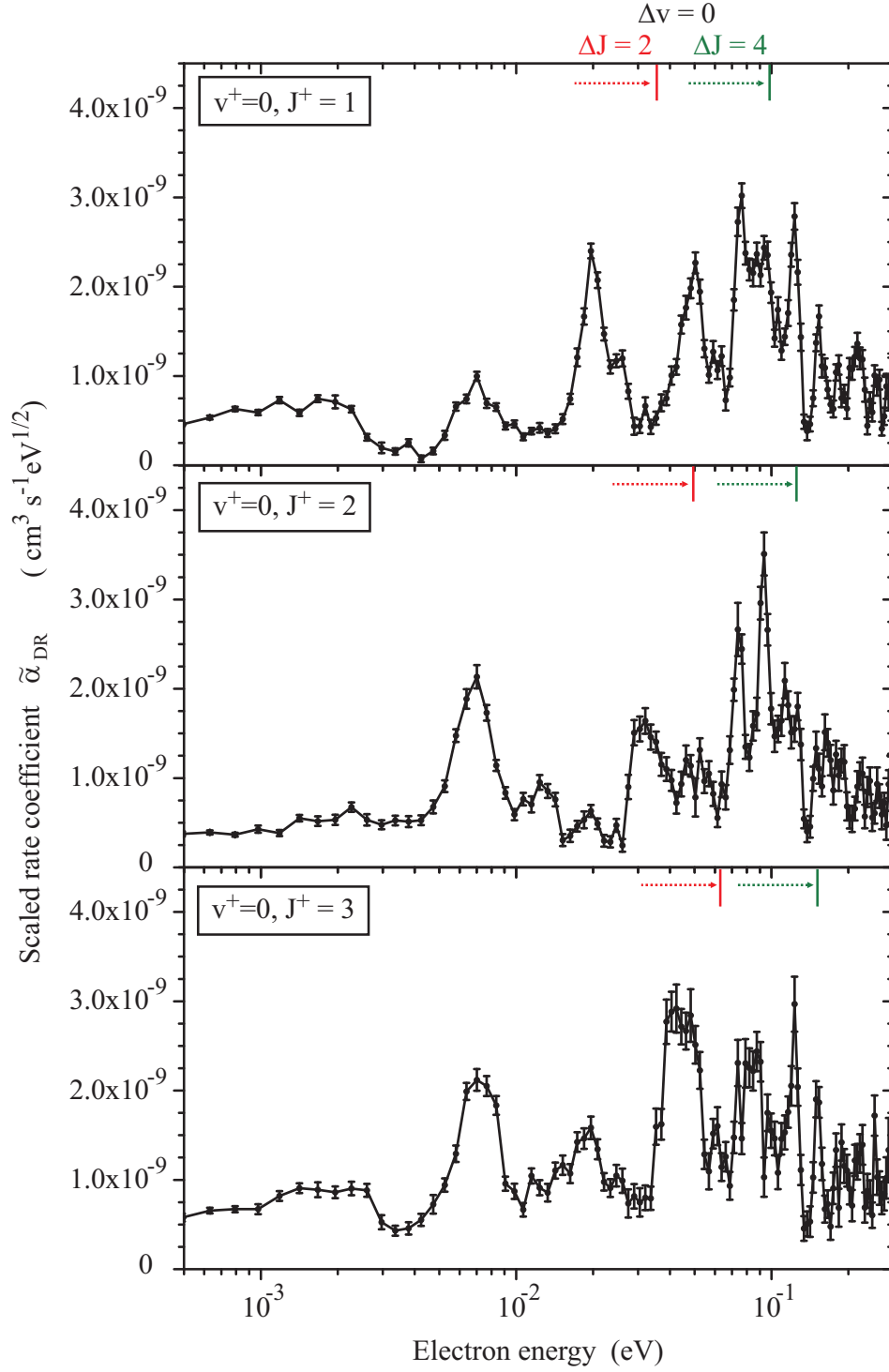
Figure 5.9: The scaled DR rate coefficients $\tilde{\alpha}_{DR}$ are presented for vibrational ground state $(v^+ = 0)$ H_2^+ ions with rotational excitation $J^+ = 1, 2, 3$, respectively, after decomposition from the $(v^+ = 1)$-fraction (Fig. 5.10) as described in [88]. The vertical lines indicate the limit of Rydberg series with $\Delta v = 0$ and $\Delta J = 2$ (red) or 4 (green).

Figure 5.10: The scaled DR rate coefficients $\tilde{\alpha}_{DR}$ are presented for $(v^+ = 1)$ H$_2^+$ ions with rotational excitation $J^+ = 1, 2, 3$, respectively, after decomposition from the $(v^+ = 0)$-fraction (Fig. 5.9) as described in [88]. The vertical lines indicate the limit of Rydberg series with $\Delta v = 0$ and $\Delta J = 2$ (red) or 4 (green).
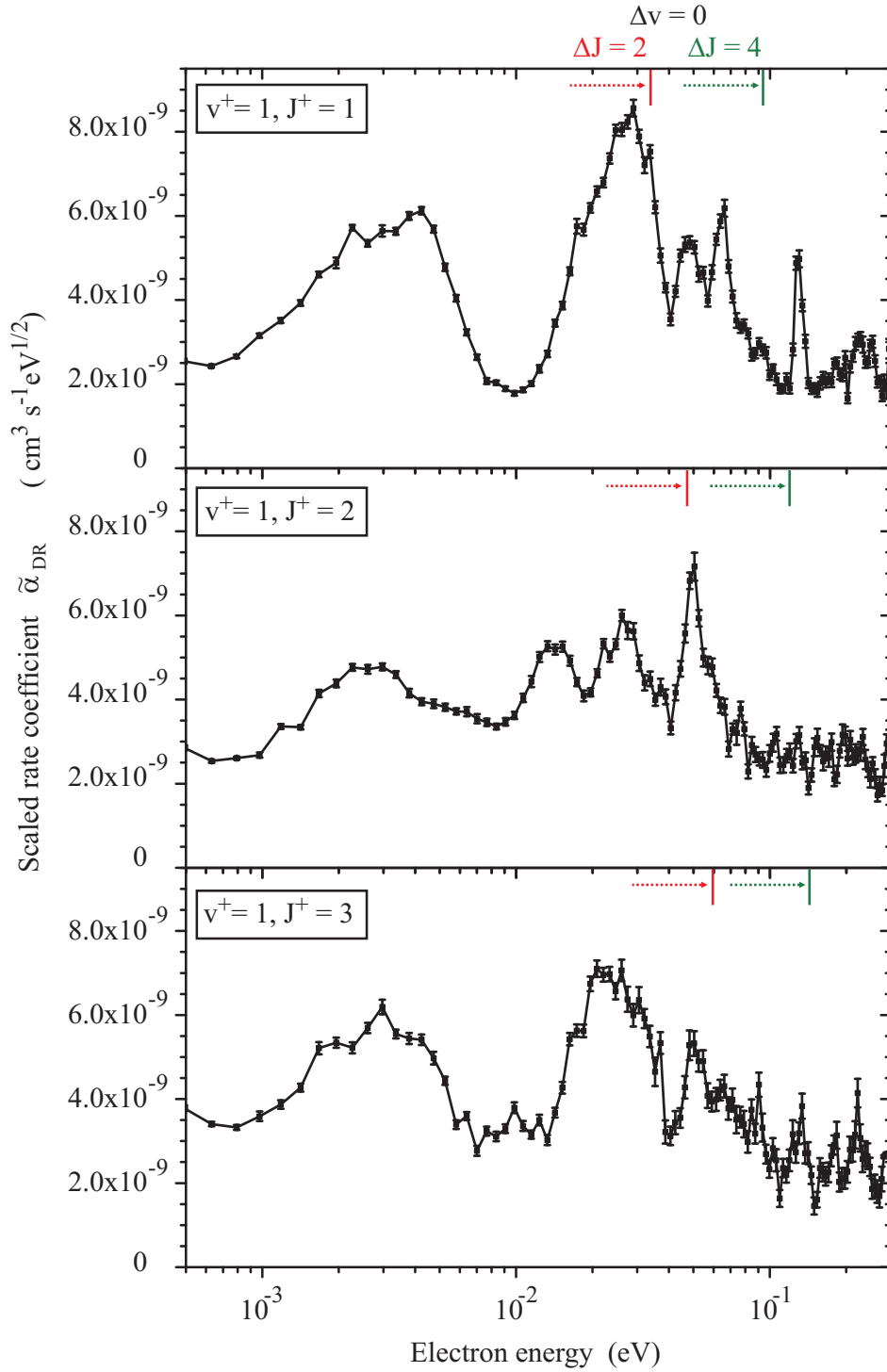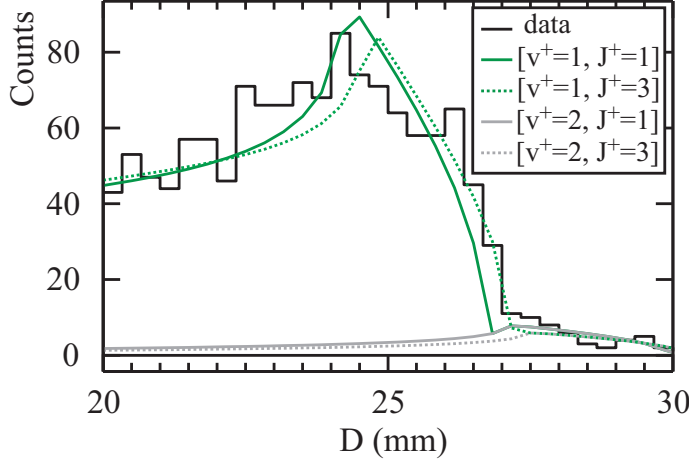
Figure 5.11: The measured transverse distance distribution at 10 meV (Q(1) ($v' = 1$)) is compared to model functions (Eq.(3.10)) assuming ($v^+ = 1, J^+ = 1$) (green solid line) or ($v^+ = 1, J^+ = 3$) (green dotted line) ionic state contributions with a small $v^+ = 2$ background (gray).

sponding to changes in the vibrational state, but the limits are out of the plotted range. The ones shown here indicate the energy range where the electron capture can resonantly form a mono-excited Rydberg state by a change of the rotational quantum number by a value of 2 or 4. They roughly coincide with the most pronounced measured structures in the DR rate coefficient, but for their complete assignment to a distinct Rydberg state the energetic positions of individual intermediate states will have to be considered. Although the initial ionic state is already known this is beyond the scope of this work but can provide in particular in future theoretical calculations a first indication for the energetic location of resonances.

However, it should be noted that the decomposition of the measured DR rates into the individual ro-vibrational contributions is achieved only down to the vibrational level, i.e. in particular the influence of additional rotational states which are partly populated by the selected ionization path cannot be disentangled in the final result. Especially for the Q(1) ionization path also a small $J^+ = 3$ ionic population is created besides $J^+ = 1$ ions, which influences the measurement once $\alpha_{DR}^{(v^+, J^+=3)}$ becomes large. Indeed, fragment imaging measurements at 10 meV indicate a possible $J^+ = 3$ ionic contribution in the recorded DR events from ions produced through the Q(1) ($v' = 1$) transition. In Fig. 5.11 the corresponding data at large transverse distances are compared to model functions associated with a kinetic energy release from either $J^+ = 1$ or 3 ionic states. The comparison suggests a significant $J^+ = 3$ fraction. Its relative contribution cannot be quantified as it will require to include unknown state specific angular distributions in the analysis procedure.

A further detailed comparison to present theoretical calculations as well as to recent experiments at CRYRING [123], which employed a supersonic expansion source together

with vibrational SEC in the storage ring in order to study the H_2^+ DR rates in the lowest ro-vibrational levels, can be found in [88]. Here, the studies will continue on the fragmentation dynamics associated with the electron capture process and focus in particular on the role of selected ro-vibrational states at defined electron collision energies. These will give access to the involved electronic symmetries through the fragment angular distributions towards a complete picture of the resonant electron-ion interaction.

5.2.2   Angular distributions of selected ro-vibrational states

Taking advantage of the selective ion production in LISE the fragmentation dynamics are studied in the following. Similar to the experiments on HD^+, the studies employ the fragment imaging technique and focus mainly on the fragment angular distributions associated with the resonant range of the DR cross section at low relative electron collision energies, i.e. below ~ 130 meV. The aim is to explore on the one hand at a particular collision energy the electronic symmetry associated with a DR resonance and on the other hand compare explicitly the influence of the initial ionic state on the fragment angular distribution. While the fragment angular emission is quantitatively deduced from the transverse distance distribution, additional information on the ionic state contributions are extracted from the measured kinetic energy release, accessible by the complete 3D data. This will allow the identification of small vibrational state fractions in the recorded data which might not be distinguishable from the transverse distance information alone. In fact, at the applied electron collision energies only one final atomic product state configuration is accessible ($H(1s) + H(2)$) so that varying amounts of kinetic energy release can only be caused by ro-vibrational excitations of the H_2^+ ion.

The measurement scheme is adapted to the one employed in the HD^+ experiments except that the electron target acceleration voltage is already detuned as soon as the combined phase-space cooling of the molecular ion beam has been completed, i.e. typically after 0.5 s. H_2^+ ions are prepared through four different REMPI ionization pathways in distinct ro-vibrational ionic state configurations for these experiments (see Table 5.2). Therefore the measurement grid covers a less dense energy range compared to the HD^+ measurement series. The selected electron collision energies focus on pronounced resonant structures appearing in the state specific DR rates at $E_d \sim 11$ meV, 23 meV, 50 meV, 130 meV as well as at zero detuning energy (compare to measured DR rate in Figs. 5.9 and 5.10).

Identification of the ionic states and angular emission analysis

The ro-vibrational ionic state distribution of the stored ions is determined, on the one hand, by the initial population prepared in the REMPI process but can, on the other hand, also be influenced by elastic collisions, mainly with electrons, during the storage of the H_2^+ ions in the TSR. This requires the identification of possible ro-vibrational state contributions through their kinetic energy release in the first analysis step of fragment imaging measurements. Subsequently, an appropriate restriction on the storage time can reduce the influence of minor ro-vibrational state fractions and enhance the focus on the dominant level contribution. For instance, in case of the example presented in Fig. 5.5 at zero detuning energy, the data acquired within the first ~ 2 s agrees with a single state contribution, whereas at larger storage times a significant influence of the $v = 0$ level population induced through vibrational cooling by SEC becomes visible.

With a nearly isotropic angular emission at zero detuning energy the ro-vibrational state contributions can still precisely be inferred from the transverse distance distribution alone. However, at low detuning energies possible additional anisotropic emission interferes with the identification of level contributions. In particular the energetically close vibrational ground state fraction might remain hidden under an anisotropic transverse distance distribution attributed to the first vibrationally excited state. Hence, only the full 3D measurement can disentangle the various contributions through their kinetic energy release, i.e. the measurement of both the transverse distance as well as the fragment impact time differences are required.

At the current fast ion beam velocities the fragment impact time differences at the detector are too short compared to the time resolution. Thus a complete separation of the vibrational state contributions based on the determination of the kinetic energy release cannot be achieved for the analysis of the fragment angular distributions. But the additional time information is used here to identify the contributing ionic state fractions. Employing a restriction on events with short impact time differences, i.e. nearly perpendicular fragmentation to the beam direction, will reduce the influence both of the limited time resolution as well as the angular emission characteristics on the remaining spectra. In this case the transverse distance D approximately reflects the 3D fragment distance D_{3d}, which is proportional to the kinetic energy release (Eq.(3.2)). Thus, exploiting the high transverse distance resolution, even small vibrational state contributions can be identified at distinct transverse distances D. The remaining data are only smeared by the finite overlap positions of the electrons in the electron target, i.e. by the possible different flight distances.
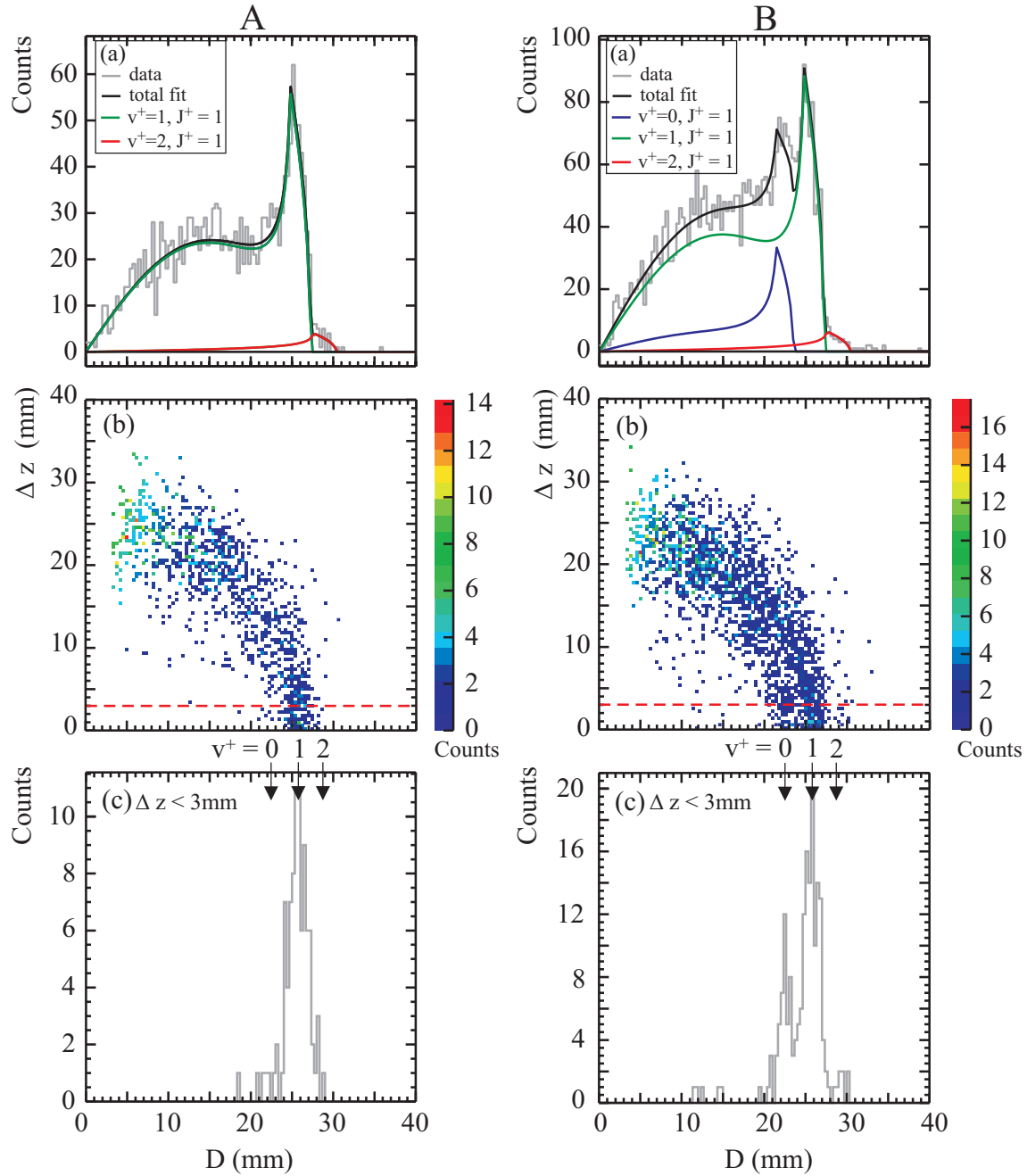
Figure 5.12: The recorded DR events of H$_2^+$ ions (Q(1) ($v' = 1$) ionization path) at $E_d = 50$ meV are compared between early (A; $t < 1$ s) and late storage times t (A; $t > 8$ s). The data are represented both by the 2D information, i.e. the transverse distance distribution (a), and the complete 3D information (b). In window (a) the black solid line represents the total fit result using Eq.(3.10), which is decomposed into the individual ionic fractions (v^+, J^+). In (c) the data are restricted to nearly perpendicular fragmentation events ($\Delta z < 3$ mm).

An example is given in Fig. 5.12 for the measurement of the fragmentation kinematics at 50 meV electron detuning energy with ions produced through a Q(1)($v' = 1$) transition. The kinetic energy release of these events can be read from the radius in the central graph where the fragment impact time differences Δt (corresponding to Δz after conversion into a length scale) are plotted versus the simultaneously measured transverse distances D. After storage times of about 8 s (Fig. 5.12 B), the ions initially created with a dominant population in the $v^+ = 1$ state are partly cooled to the vibrational ground state through SEC. These events are characterized by their lower kinetic energy release and hence recognized in Fig. 5.12 B(b) by their smaller radius. In the transverse distance distribution they are found at shorter distances (Fig. 5.12 B(a) and (c)). Immediately after the injection ($\lesssim 1$ s), on the other hand, only the complete 3D information convincingly reveals that the $v^+ = 0$ contribution is still at a negligible level (Fig. 5.12 A) which allows to attribute the angular dependence fully to ions in the first vibrationally and rotationally excited state; the rotational excitation being inferred from the transverse distance distribution.

As mentioned earlier (p. 103), events at higher transverse distance D, whose energy release exceeds the one for $v^+ = 1$ ions, most likely originate either from the toroidal section or ro-vibrationally excited ions. Their relative contribution remains small and is thus treated as $v^+ = 2$ ionic fractions with a fixed isotropic emission pattern in the analysis.

The outlined procedure allows to trace even small vibrational state fractions and to restrict the data by selection of the storage time period to yield their least influence. The fragment angular emission characteristics can then be determined from the transverse distance distribution of the remaining data, following accordingly the analysis described for HD^+ (Secs. 3.2.2 and 4.2.2). Also here the angular distribution of the H_2^+ fragmentation is represented by Legendre polynomials of even order l. The maximum order is again recognized as $l = 4$ while even higher orders remain on a negligible level and hence set to zero in the final analysis.

In case more than one ionic state fraction have to be considered, the analysis procedure becomes less straight forward since either one can exhibit a distinct angular emission pattern. Then the angular distribution associated with the individual ionic state fractions can only be uniquely disentangled from a step-wise analysis procedure if one of them has been analyzed independently. For instance, in Fig. 5.12 the $v^+ = 0$ fragmentation properties are deduced from the total transverse distance distribution (storage times > 8 s) by treating the $v^+ = 1$ ionic fraction with a fixed angular dependence, which has been obtained independently at earlier storage times. This procedure was generally required to extract the $v^+ = 0$ angular distributions since even small populations of $v^+ = 1$ ions

caused a significant influence due to the larger state specific DR rate (see Fig. 5.8). The $v^+ = 0$ Legendre coefficients could thus often only be deduced by the expense of a larger uncertainty.

Angular emission properties

Utilizing the analysis procedures outlined above, the fragmentation kinematics at specific resonances in the DR cross section of H_2^+ have been studied. The obtained Legendre coefficients characterizing the fragment angular distribution of ions in selected ro-vibrational states are presented in Figs. 5.13 ($v^+ = 1$) and 5.15 ($v^+ = 0$) in comparison with the state specific scaled DR rates $\tilde{\alpha}_{DR}^{(v^+, J^+)}$.

They point out a strong anisotropy with varying contributions from both the 2nd and 4th order Legendre polynomials. Note, that the a_2 coefficients are on average slightly higher than those describing the HD^+ fragmentation in Sec. 4.2.2 while the range of a_4 values mostly comprises the one extracted for HD^+. The deduced Legendre coefficients not only deviate from zero but also exhibit a dependence on the electron detuning energy which they express through a slight increase towards larger energies. Variations on a similar narrow energy scale, which have been found for the HD^+ fragmentation, are not observed but might display by increasing the density of the measurement points.

Moreover, the present data indicate a dependence of the observed angular distribution on the ro-vibrational ionic state. For measurements at the same detuning energy E_d the extracted anisotropy coefficients a_2 and a_4 vary for different vibrational and partly even rotational states of the H_2^+ ions.

Focusing first on the anisotropy results associated with ($v^+ = 1$) - H_2^+ ions (Fig. 5.13), one finds that a dependence on the ionic rotational states is less accentuated at the lowest two measured electron collision energies, i.e. below $\sim$23 meV. In contrast, the state specific Legendre coefficients a_2 and a_4 notably differ from each other in the measurement series at $\sim$50 meV, which is recognizable already in the recorded transverse distance distributions. They are presented separately in Fig. 5.14 together with the fitted model functions. The data obviously comply with the kinetic energy release from the expected dominant vibrational *and* rotational level population, and are neither noticeably influenced by $v^+ = 0$ nor $v^+ = 2$ contributions. The most distinct anisotropy can be associated with $J^+ = 2$ ions, which exhibits Legendre coefficients at least 1.5 times larger as obtained for the angular dependence from the $J^+ = 3$ ionic state. Especially the fragmentation into the forward direction is preferred, suggested by the enhanced number of events recorded at distances below $\sim$20 mm.

Figure 5.13: (a) The scaled DR rate coefficient $\tilde{\alpha}_{DR}^{(v^+=1,J^+)}$ (Fig. 5.10) and the obtained Legendre coefficients a_2 (b) and a_4 (c) as functions of the electron detuning energy for the different rotational states J^+ of $v^+ = 1$ ions. The results are compared to the expected angular dependence of a pure incident d partial-wave in the axial-recoil approximation after convolution with the flattened Maxwellian velocity distribution of the electron beam (dashed lines in (a) and (b); more details in Sec. 5.2.3).
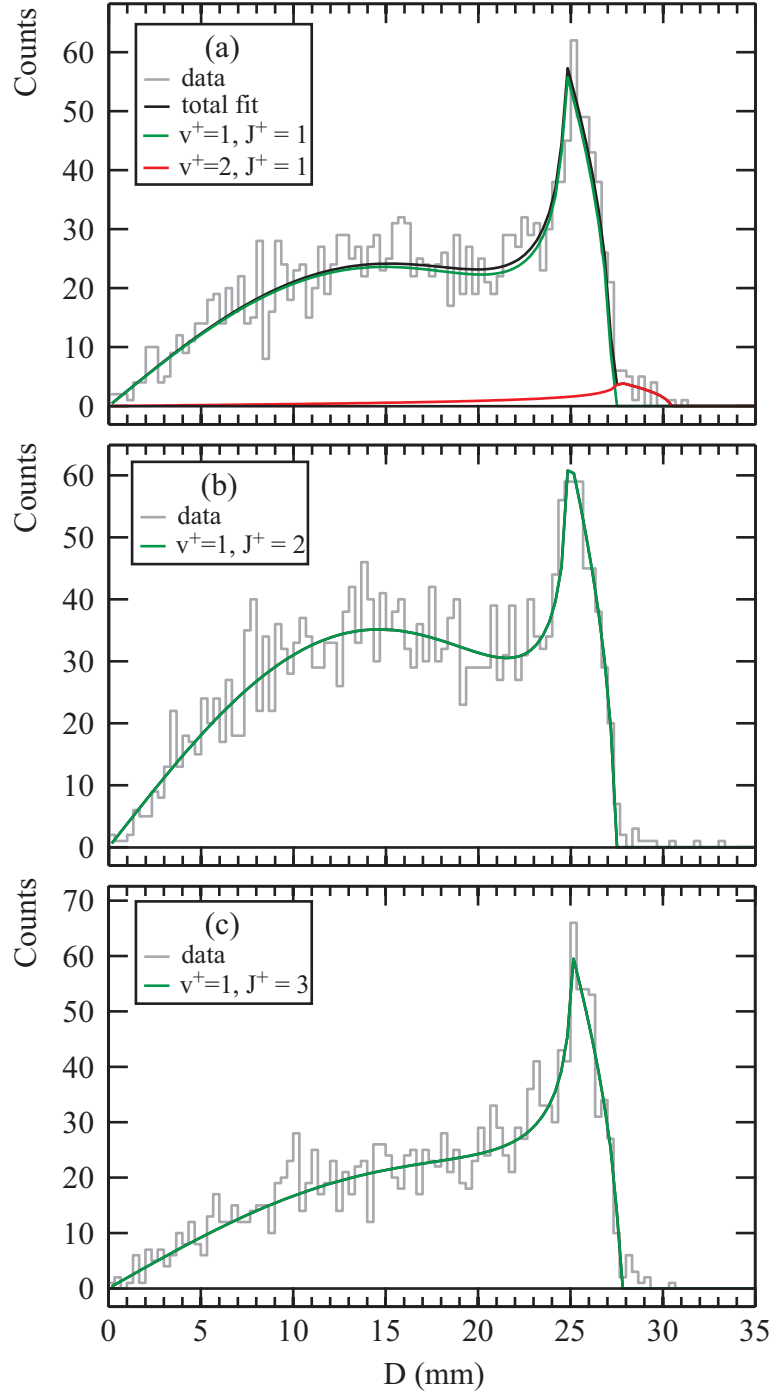
Figure 5.14: The measured transverse distance distributions from DR events at 50 meV are given for different ionic rotational J^+ states in the $v^+ = 1$ vibrational excitation. The green solid lines represent the result of fitted model functions (Eq.(3.10)) for the respective ion state contributions: (a) $[v^+ = 1, J^+ = 1]$ ($[v^+ = 2, J^+ = 1]$ - background contribution; red), (b) $[v^+ = 1, J^+ = 2]$ and (c) $[v^+ = 1, J^+ = 3]$.
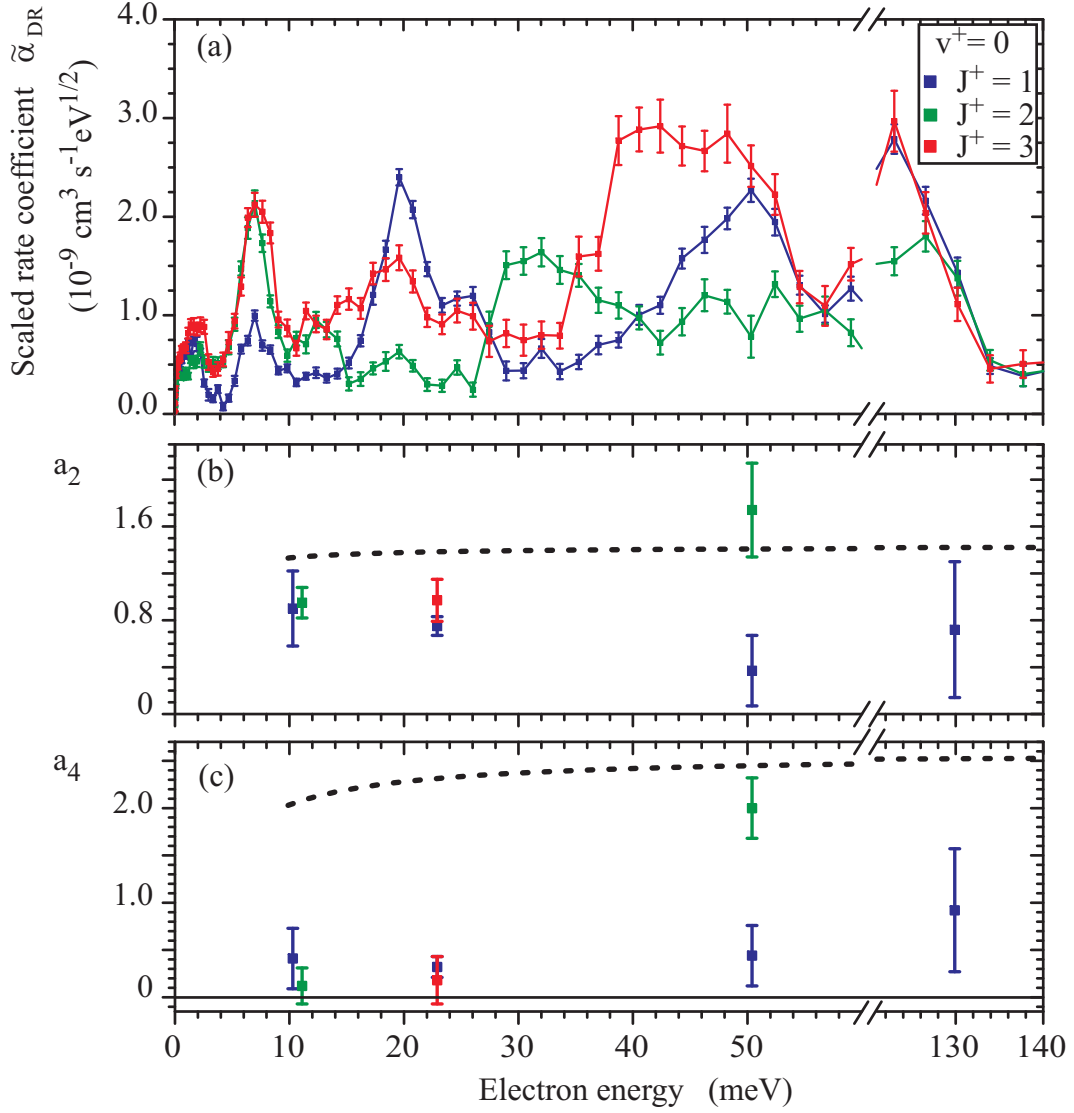
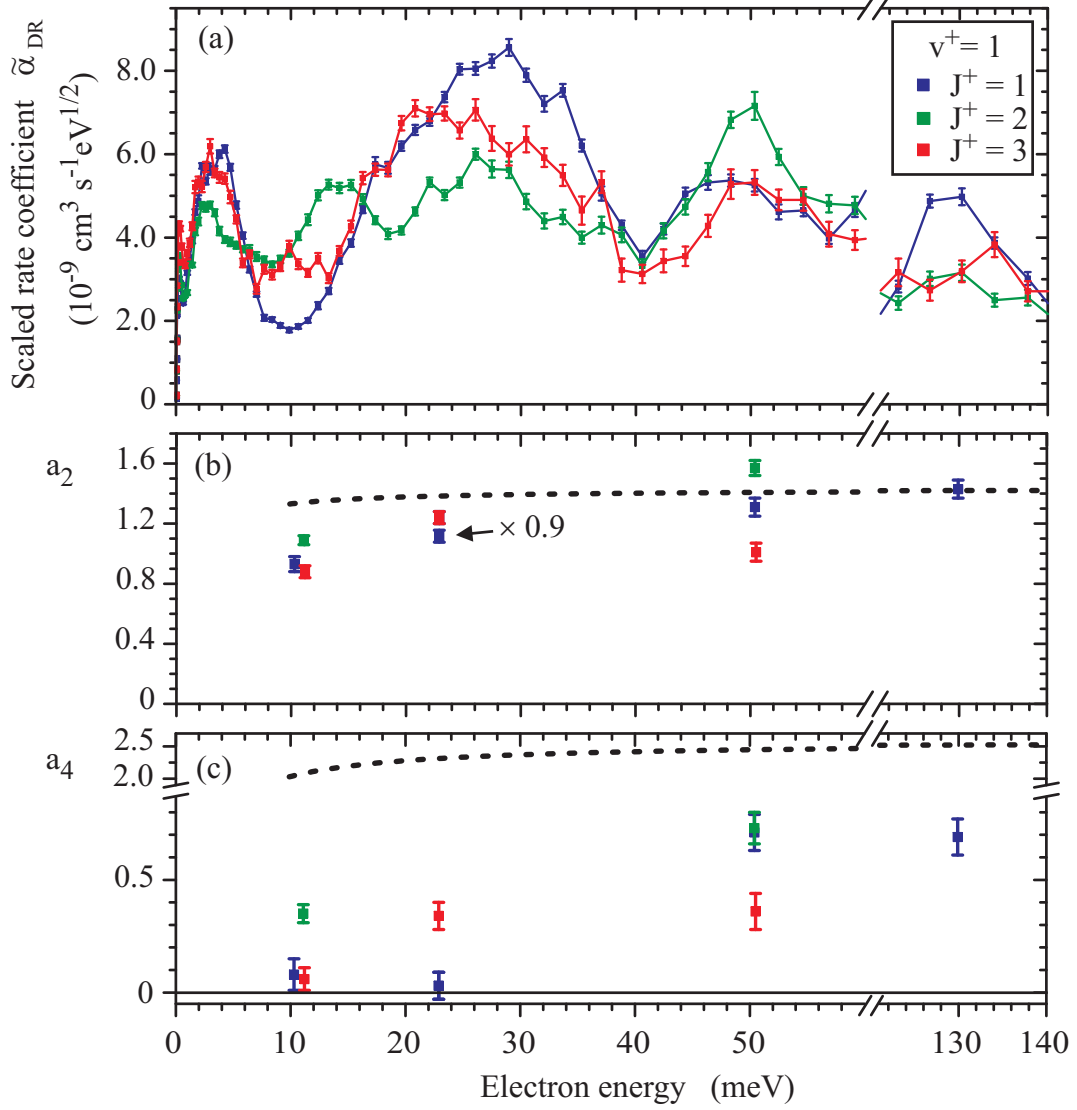Figure 5.15: (a) The scaled DR rate coefficient $\tilde{\alpha}_{DR}^{(v^+=0,J^+)}$ (Fig. 5.9) and the obtained Legendre coefficients a_2 (b) and a_4 (c) as functions of the electron detuning energy for the different rotational states J^+ of $v^+ = 0$ ions. The results are compared to the expected angular dependence of a pure incident d partial-wave in the axial-recoil approximation after convolution with the flattened Maxwellian velocity distribution of the electron beam (dashed lines in (a) and (b); more details in Sec. 5.2.3).

The analysis of $v^+ = 1$ ionic dissociation properties is assisted by the enhanced state specific DR rates in addition to the dominant production in the Q(J)($v' = 1$) ionization path, facilitating their study unaffected from other vibrational contributions. In contrast, $v^+ = 0$ fragment angular distributions are only accessible by properly considering the $v^+ = 1$ fraction in the recorded DR events since the higher $v^+ = 1$ DR rate causes the enhancement of even small $v^+ = 1$ ionic populations.

Except for the measurement at ~ 23 meV, which studied ions produced through Q(1)($v' = 0$) transitions dominantly in ($v^+ = 0$) - states, all results presented in Fig. 5.15 were obtained with stored H$_2^+$ ions initially created in Q(J)($v' = 1$) transitions, i.e. starting with a dominant $v^+ = 1$ ionic population. Consequently, vibrational cooling through SEC had to be employed in order to enhance the $v^+ = 0$ population. Nevertheless, the resulting $v^+ = 0$ contribution to the recorded DR events remains small within the applied storage times compared to the dominant $v^+ = 1$ fraction in the transverse distance distributions. Accordingly the uncertainty on the fitted anisotropy coefficients a_2 and a_4 in Fig. 5.15 are larger. In particular the anisotropy at 50 meV ($J^+ = 2$) is deduced from low statistics of the ($v^+ = 0$) - fraction and gives an estimate only. The data point is shown for the sake of completeness and should not take part in a detailed discussion.

By comparing the extracted $v^+ = 0$ anisotropy coefficients to the ones for $v^+ = 1$ the angular distributions partly reveal a dependence on the vibrational ionic state, for instance compare at 23 meV and 50 meV the values for $J^+ = 1$ ions. A possible rotational state dependence cannot be recognized for the $v^+ = 0$ results and will require smaller uncertainties of the deduced coefficients.

Apart from the state specific differences characterizing the extracted anisotropy coefficients at certain detuning energies, no general trend can be depicted for the rovibrationally resolved fragment angular distributions. For instance, slow rotating ions do not show a higher anisotropy. Also the comparison with the scaled DR rate coefficients does not reveal similar correlations as found in the measurements on HD$^+$. A comparable detailed analysis will require a higher density of the measurement points.

5.2.3 Comparison to model angular distributions

Currently, there are no explicit theoretical calculations available or being performed which yield, similar to the MQDT-results for HD$^+$, predictions on the H$_2^+$ angular distributions by taking into account the specific ro-vibrational ionic states at the applied electron collision energies. Therefore the discussion of the obtained anisotropies will focus on a comparison to model distributions based on the dominant partial wave treatment by

Guberman [59], both in and beyond the axial-recoil approximation. The same possible electronic symmetries of the captured electron will have to be considered therein as in the case of the deuterated hydrogen molecule HD^+ in Sec. 4.3.1, that is expecting a dominant d partial-wave [14] with possible s-wave influence [16, 72]. The discussion will thus follow the one outlined for HD^+ in Secs. 4.3.1 and 4.3.3.

First, the electronic symmetry of the incoming electron is treated in the dominant partial wave model [59] with a pure d-wave and assuming the validity of the axial-recoil approximation. The expected angular dependence associated with the $Y_{2,0}$-spherical harmonic (Eq.(4.7)) is contrasted with the measured anisotropy coefficients in Figs. 5.13 and 5.15 (see previous section) for $v^+ = 1$ and $v^+ = 0$ ions, respectively, after proper convolution over the electron velocity distribution (Eq.(4.10)).

The obtained 4th order Legendre contributions in the H_2^+ angular distributions support the predicted d-wave influence in the DR process of H_2^+. However, their amplitudes significantly deviate from the one expected in case of a pure d-wave treatment ($a_{4,d} = \chi_4(E_d)18/7$), whereas simultaneously the a_2 coefficients are close to the one predicted ($a_{2,d} = \chi_2(E_d)10/7$), both in case of $v^+ = 1$ and $v^+ = 0$ ions (not regarding the value at 50 meV for ($v^+ = 0$, $J^+ = 2$) ions because of the large uncertainty of this particular measurement as discussed on page 120). Furthermore the variations of the observed angular distributions as a function of the electron collision energy as well as for different ionic excitations cannot be explained by this model.

Consequently, in the next step the possible contribution of the incident electron's s partial-wave is considered, closely following the analysis of the HD^+ results within the axial-recoil approximation. Taking into account a superposition $\|c_s Y_{0,0} + c_d Y_{2,0}\|^2$ of s and d partial-waves (Eqs.(4.12)-(4.14)) yields both the relative d-wave amplitudes $|c_d|^2$ as well as the s and d partial-wave phase shifts $\cos \epsilon$ presented in Figs. 5.16 and 5.17 for H_2^+ ions in $v^+ = 1$ and $v^+ = 0$, respectively.

The results for H_2^+ ions in the first excited vibrational state (Fig. 5.16) imply low relative d-wave amplitudes $|c_d|^2$ at the selected electron detuning energies, reaching at maximum a value of $\sim 30\%$, supporting the above conclusions from the pure d-wave approach. The relative phase ϵ between the s and d partial-waves is deduced from both a_2 and a_4 values and displayed in Fig. 5.16(b). Both partial waves are found to contribute to the DR process through a coherent sum with a nearly constant relative phase of $\epsilon = \pi/3$ at the studied energies, i.e. suggest interfering s and d partial-waves. This is also corroborated by the ratio a_4/a_2, which deviates from an incoherent superposition ($\tilde{a}_4/\tilde{a}_2 = 18/10$) reflected by the dashed line in Fig. 5.16(c). The possible dependence of the ionic rotational state
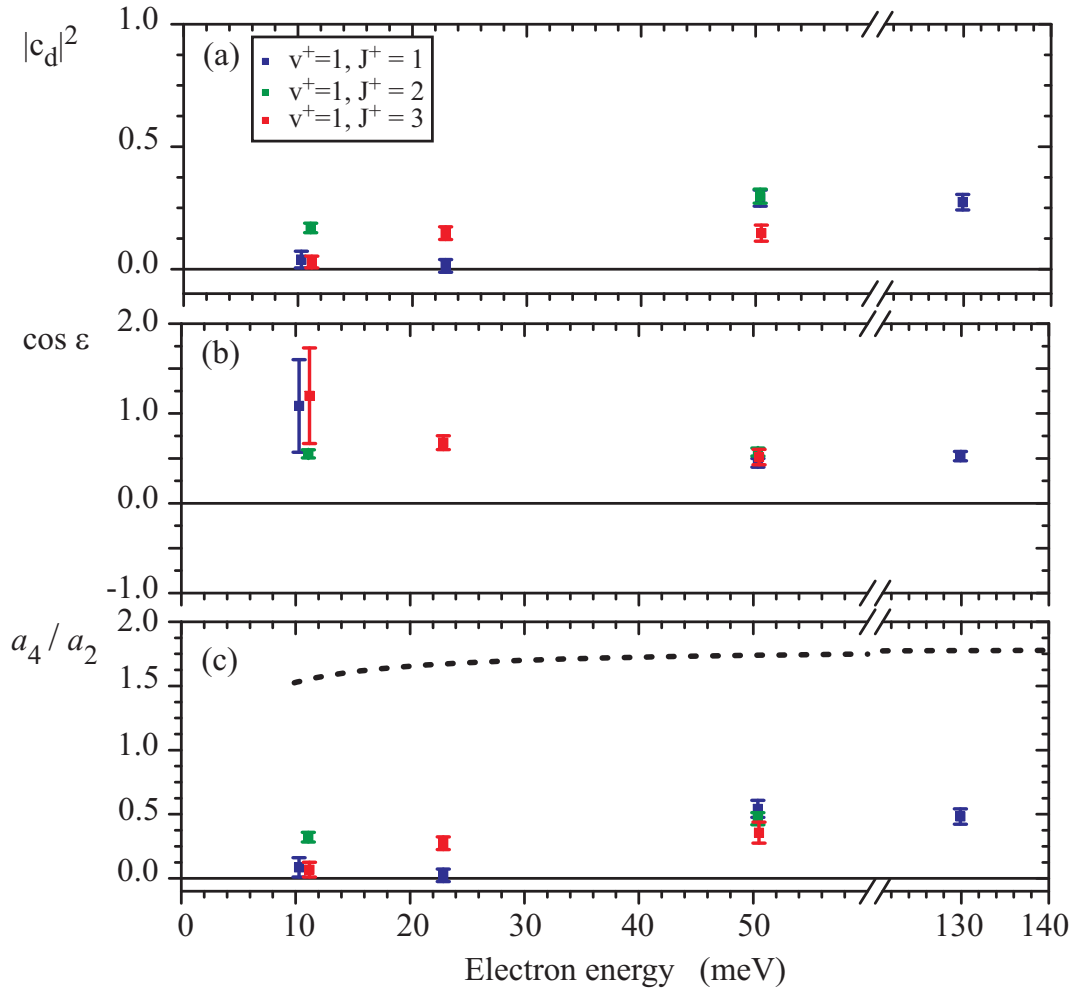
Figure 5.16: Similarly to Fig. 5.17, the (a) squared d-wave contribution $|c_d|^2$, (b) the s and d relative phase represented by $\cos \epsilon$ and (c) the ratio a_4/a_2 are given for the measured results of $v^+ = 1$ H_2^+ ions assuming interfering s and d partial-waves. The a_4/a_2 ratio is compared to the case of incoherent superposition of both symmetries after convolution with the flattened Maxwellian velocity distribution of the electron beam (dashed line).

in the angular distribution can mainly be attributed to variations in the relative d-wave amplitude $|c_d|^2$. However, J^+-state dependent differences are only found on the level of ± 0.15 in the relative d-wave amplitude.

Despite the large uncertainty, which hinders a rotationally resolved discussion, the $v^+ = 0$ results (Figs. 5.17) exhibit similar to $v^+ = 1$ ionic states mostly low relative d-wave amplitudes $|c_d|^2$. The relative phase shift ϵ, on the other hand, approaches $\pi/2$ and suggests a possible incoherent superposition at higher detuning energies, in fact similar to the results on $(v^+ = 0)$- HD^+ (Fig. 4.16).
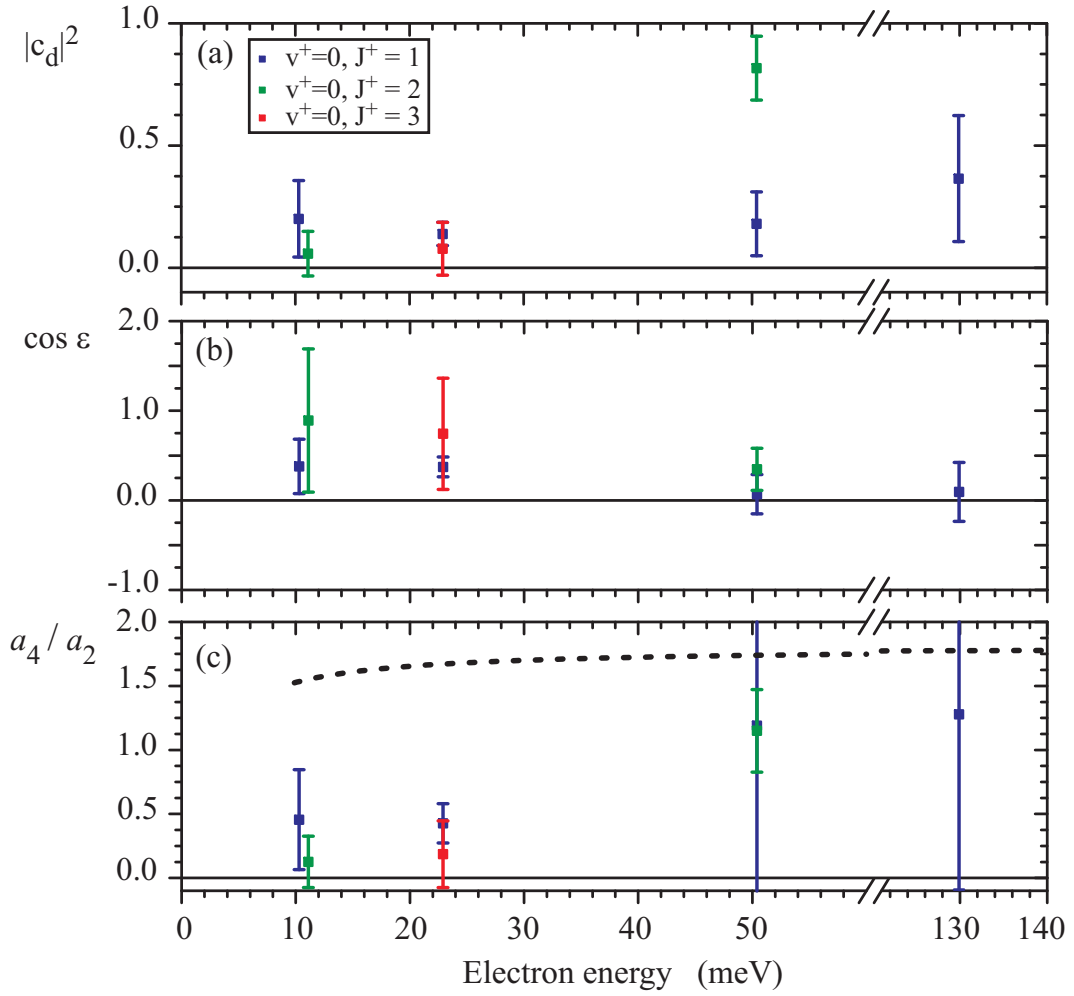
Figure 5.17: For interfering s and d partial-waves (a) the squared d-wave contribution $|c_d|^2$, (b) the s and d relative phase represented by $\cos \epsilon$ and (c) the ratio a_4/a_2 are given for the measured results of H_2^+ ions in the vibrational ground state ($v^+ = 0$). The a_4/a_2 ratio is compared to the case of incoherent superposition of both symmetries reflected by $\tilde{a}_4/\tilde{a}_2 = 9/5$ after considering the anisotropic velocity distribution of the electron beam (dashed line).

Relying on the validity of the axial-recoil approximation, these results do not support the predicted dominant role of the d-wave in the electron capture process and find instead rather large relative s-wave amplitudes. However, the observed reduction of the anisotropy attributed to an isotropic s-wave contribution can also hint, similarly as for HD^+, at the breakdown of the axial-recoil approximation. Estimations from a semiclassical model in Sec. 4.3.3 have suggested already for HD^+ that even intermediate resonances in the first rotationally excited state can exhibit a rotational frequency sufficient to significantly

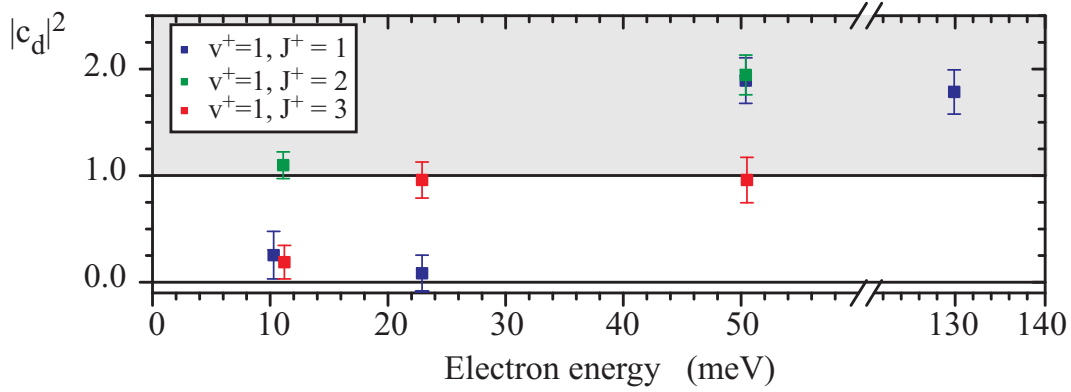Figure 5.18: The relative d-wave amplitudes $|c_d|^2$ deduced from the measured a_4 coefficients according to Eqs.(4.14) and (4.24) are presented, considering the attenuation $\gamma_4(\omega_{J'=1}\tau)$ to be caused by rotation of the molecule in a $J' = 1$ intermediate state (see Fig. 4.19(a)). Note, values of $|c_d|^2 > 1$ (gray shaded area) are artificial and indicate that the applied γ_4 is too small (attenuation is estimated too strong).

influence the observed angular distributions. Similarly strong attenuation factors γ_l are also found for H_2^+ at a $(J' = 1)$-resonance lifetime of $\tau_r \approx 0.2$ ps (see dashed line in Fig. 4.19(a) (Sec. 4.3.3)). In fact, a reduction of the initial angular dependence by a factor of ~ 3.7 and ~ 6.5 can be expected according to this model and is nearly independent of the rotational excitation of the intermediate resonance for the a_2 and the a_4 coefficients, respectively (negligible difference between $v^+ = 0$ and 1). Applied to a pure d-wave induced fragmentation this will imply that *both* initial Legendre coefficients ($\tilde{a}_2 = 10/7$ and $\tilde{a}_4 = 18/7$) reduce to almost the same value of ≈ 0.4 as illustrated in Fig. 4.19(b) (Sec. 4.3.3). This is contrary to the experimentally deduced values shown in Figs. 5.13 and 5.15 reasoning that the measured anisotropy coefficients do not comply with a pure d-wave influence, even in a breakdown of the axial-recoil approximation according to this model.

On the other hand, applying the suggested attenuation factors γ_l will yield corrected relative d-wave amplitudes $|c_d|^2$ from the measured a_4 anisotropy coefficients through $7a_4/(18\gamma_4 \cdot \chi_4)$ (use Eqs.(4.14) and (4.24)). The results are presented in Fig. 5.18 for $v^+ = 1$ ions and suggest in some cases pure d-wave couplings. This is in contradiction to the just drawn conclusion since one also has to consider the according attenuation factor on the obtained a_2 coefficients, yielding in fact too large a_2 values ($> 10/7$) which are *not* in agreement with a pure d-wave (multiply the results shown in Fig. 5.13(b) by ~ 3.7 and compare to the dashed line). In fact, the corrected a_2 data even exceed

the maximum allowed value of ≈ 3 expected for interfering s and d partial-waves (see Fig. 4.15 in Sec. 4.3.1). Moreover, relative d-wave amplitudes exceeding unity in Fig. 5.18 due to the applied factor γ_4 do not make sense from a physics point of view (note that also for HD$^+$ the corrected d-wave amplitude yielded values larger than one). These findings suggest instead that the applied attenuation factor γ_l overestimates the effects of a rotating molecule on the fragment angular distribution, pointing either at the possible formation of resonances in the rotational ground state, which cannot be treated at all by the semiclassical model, or at shorter resonance lifetimes than assumed, for instance caused by dissociation upon the direct DR pathway.

Nevertheless, one can conclude that a pure d-wave coupling is excluded from the obtained anisotropy coefficients, even extending the theoretical approach beyond the axial-recoil approximation. The in general larger measured a_2 coefficients compared to a_4 suggest instead interfering d *and* s partial-waves with a relative phase $\cos \epsilon > 0$. In view of this theoretical treatment, ionic state dependent partial wave couplings might thus be responsible for the observed (v^+, J^+)-dependent fragment angular distributions but one cannot exclude additional influences originating from a breakdown of the axial-recoil approximation because of molecular rotation or different lifetimes of intermediate resonances. Latter effects will only be disentangled in a full theoretical treatment, but is probably responsible only for at most part of the observed state dependence.

5.2.4 Comparison to HD$^+$ fragmentation dynamics

The dynamics of DR induced fragmentation have been studied both for the hydrogen molecular ion H$_2^+$ and its deuterated relative HD$^+$ in the vicinity of low-energy ro-vibrational Feshbach resonances. The fragment angular distributions observed for rotationally averaged HD$^+$ ions revealed significant variations as a function of energy (compare Fig. 4.11 in Sec. 4.2.2). Here the role of the initial ro-vibrational ionic state in the fragment angular distribution of the DR process was not individually accessible, but the simultaneously obtained likewise varying rotational state contributions raised the question of possible influences by the ionic state.

Utilizing the ro-vibrational state selectivity in the experiments on H$_2^+$ the obtained fragment angular distributions indeed find J^+ dependent anisotropies, in particular at ~ 50 meV. They are described by contributions from Legendre polynomials both of 2nd and 4th order. On average, the deduced a_2 coefficients are slightly larger compared to those for HD$^+$, whereas the a_4 values remain within a similar parameter range as summarized in Figs. 5.19 and 5.20. However, the individual fragment angular distributions change

Figure 5.19: The obtained Legendre coefficients a_2 are compared as a function of energy between the results of (a) the rotationally averaged ($v^+ = 0$) HD^+ ions and the rotationally selected (b) ($v^+ = 1$) and (c) ($v^+ = 0$) H_2^+ ions.

only slowly between neighboring rotational states. To yield variations in the rotationally averaged fragment angular distributions as observed for HD^+ will require, among other possibilities, an energy-dependent enhancement of a single state-specific DR rate, or possibly the preferred d partial-wave coupling of all contributing ionic states in the resonant electron capture process at a defined energy.

Studying the partial wave couplings through the fragment angular distributions has generally indicated only a small relative d-wave amplitude, both for the rotationally averaged HD^+ as well as the ro-vibrationally resolved H_2^+ DR experiments. This contrasts with the predicted dominance of the d-wave in the DR process. Rather, the measurement results stress the importance of an interference between both s and d partial-waves, even in case of a breakdown of the assumed axial-recoil approximation. However, in order to derive the
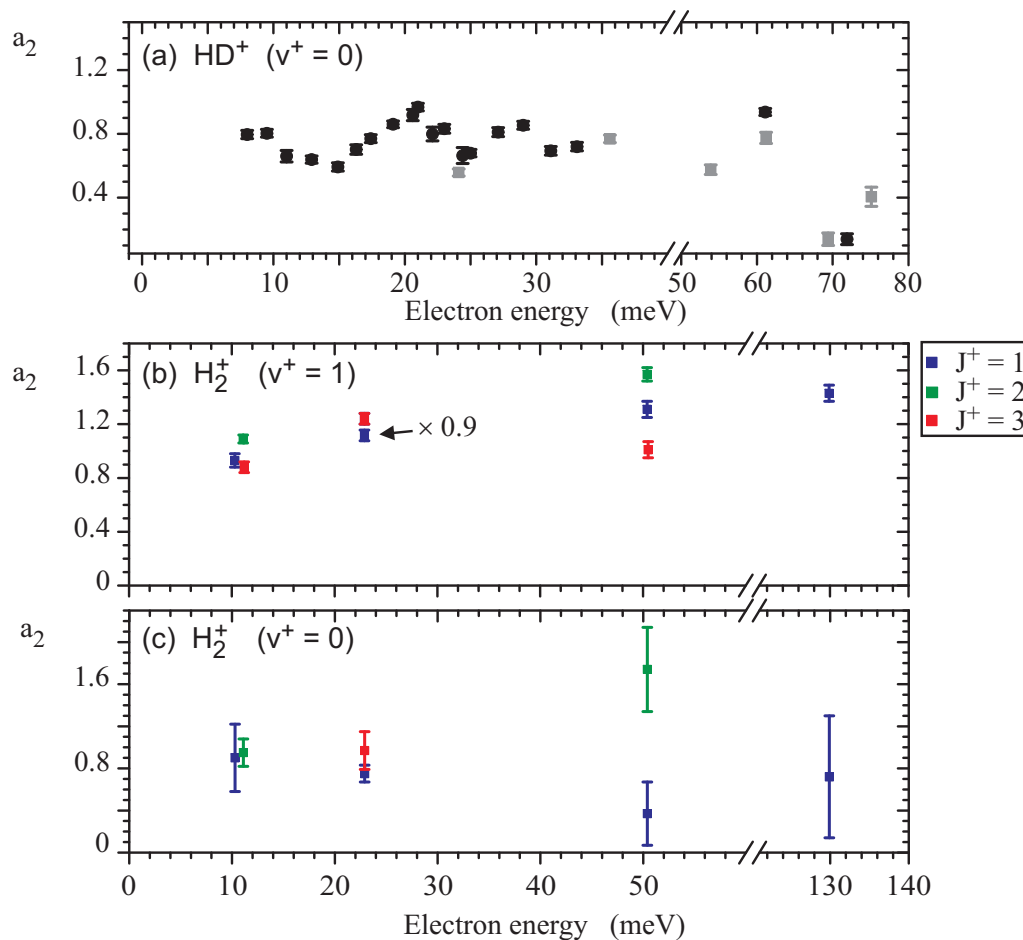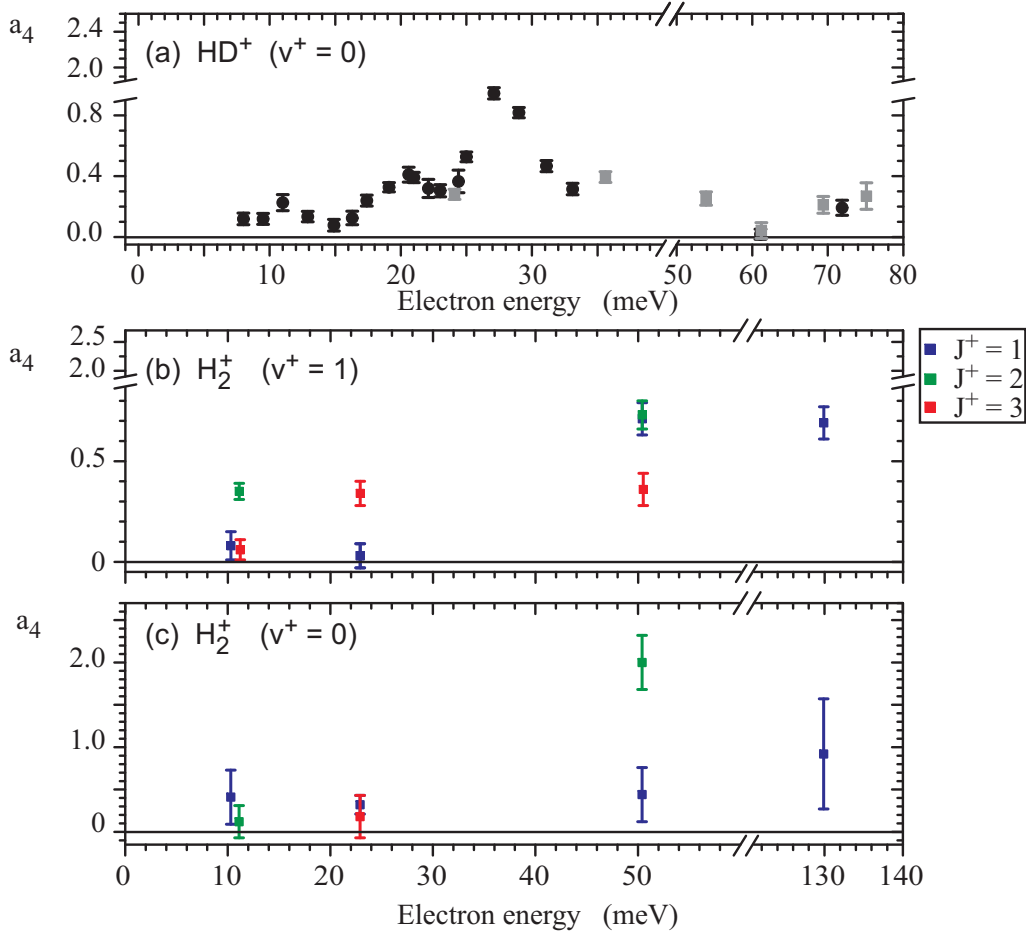
Figure 5.20: The obtained Legendre coefficients a_4 are compared as a function of energy between the results of (a) the rotationally averaged ($v^+ = 0$) HD$^+$ ions and the rotationally selected (b) ($v^+ = 1$) and (c) ($v^+ = 0$)- H$_2^+$ ions.

explicit superposition of the partial waves, one will need to consider a treatment beyond the axial-recoil approximation including a good knowledge on the resonance lifetimes.

5.3 Conclusions

Utilizing the state selective H$_2^+$ ion production in LISE, for the first time the role of ro-vibrationally *excited* ionic states in the DR process has been individually studied in high resolution twin-electron-beam experiments at the TSR. Focusing on the low-energy electron collision energy range, where ro-vibrational Feshbach resonances dominate the DR cross section, both event-by-event counting and fragment imaging experiments were

carried out.

The obtained state-specific DR rate coefficients of H_2^+ ions in the lowest two vibrational ($v^+ = 0$ and 1) and their first three excited rotational states ($J^+ = 1, 2$ and 3) were found to be characterized by unique resonant structures.

The fragmentation dynamics at selected resonances of distinct ionic states were addressed independently in 2D and 3D fragment imaging experiments. These measurements deduced fragmentation anisotropies of 2nd and 4th order, consistently with the rotationally averaged HD^+ results and suggesting interfering s and d partial-waves of the incident electron. Furthermore, at selected energies small but significant changes of the anisotropy indicate a state-specific angular dependence in the DR process.

6

Summary & Outlook

6.1 Summary

In the presented work, the fragmentation of positively charged molecular hydrogen ions was investigated in resonant slow electron collisions in the process denoted as dissociative recombination. Provided either with vibrationally cold HD^+ molecules or with H_2^+ ions in selected vibrational and even rotational excitations, the experimental studies could for the first time particularly focus on the product kinematics of this electron induced fragmentation reaction with well-directed incident electrons at energies below $\sim$100 meV. These measurements became possible by combining 2D and 3D fragment imaging with a newly introduced twin-electron-beam arrangement at the heavy-ion storage ring TSR. Together with a photocathode electron source, which created nearly unidirectional, cold electron beams, the product kinematics could be studied from the measured fragment distances at high resolution and stable ion beam conditions, probing the DR process down to a few meV incident electron energy.

The DR process of the hydrogen molecular ion is characterized at low electron collision energies by pronounced ro-vibrational Feshbach resonances which arise from a competition of dissociation routes following the resonant energy exchange with the nuclear motion in contrast to the one with the electronic system alone. With only one final state accessed at these energies, the hydrogen molecular system is particularly suited for the study of the associated fragmentation dynamics. From the obtained fragment distance distributions both the energy release as well as the product angular distributions could precisely be inferred. These determine the contributing initial ro-vibrational ionic levels and directly reflect the electronic symmetries involved in the resonance formation as long as the fragmentation can be assumed to occur fast enough compared to the rotation (axial-recoil

approximation).

Applying the twin-merged beam technique, the DR product kinematics for the deuterated hydrogen molecular ion HD^+ were measured on a dense grid of energies between 10 and 80 meV in the vicinity of these resonances. As a function of the incident electron energy, fractions of the recombination signal stemming from fast and slow rotating molecular ions were identified from the energy release of the recorded DR events, revealing variations of their amplitudes on a similarly narrow energy scale as the rotationally averaged HD^+ DR rate coefficient. These variations emphasize the sensitivity of the HD^+ DR process on the initial ro-vibrational state.

On the same measurement grid significant anisotropies were found in the observed fragment angular distributions. Described by a superposition of even-order Legendre polynomials they required contributions up to the order of 4, which, in fact, was observed for the first time in DR experiments. Reflecting these anisotropies, the a_2 and a_4 Legendre coefficients change in size even within small energy steps of only 2 meV and vary on a likewise narrow energy scale in partial correlation with the DR rate coefficient. While 4th order anisotropies are expected from the role of the incident electron's d partial-wave in the entrance channel leading to DR, their amplitudes were considerably smaller compared to those for the predicted large dominance of this d-wave coupling. Instead a rather large contribution of the interfering s partial-wave was deduced from the measurements by comparing the results to model distributions based on the axial-recoil approximation. A possible breakdown of the axial-recoil approximation assumed in this step was considered, with estimates indicating that even for slowly rotating resonant states this approximation, applied so far in theoretical treatments of DR product angular dependences, is not necessarily satisfied. In fact, deviations from its underlying requirements can cause significant reductions of the observed anisotropies influencing the partial-wave analysis.

The individual roles of the initial ro-vibrational states in the electron-molecule interaction of the DR process became accessible for the first time with H_2^+ ions in defined excitations. In a collaborative experimental effort applying the new experimental technique, H_2^+ molecules in selected vibrationally and rotationally excited states were produced by a state selective laser ion source (LISE) recently developed at the University of Louvain-La-Neuve, Belgium. The measurements mainly focused on the low-energy ro-vibrational Feshbach resonances, where the strongest influence from the initial ionic state is expected. Taking advantage of the high resolution in the twin-merged beam setup the state-specific DR rates were obtained for ions in the lowest two vibrational and first three excited rotational states independently. Each set revealed narrow characteristic patterns down to the

limit of the energy resolution, which reflect the resonant electron capture by ions in defined initial states. Selecting from the state-specific structures particular resonances, the associated fragmentation dynamics were studied. At energies between 10 and 130 meV the deduced anisotropies were characterized by 2nd and 4th order Legendre polynomials with contributions varying as a function of energy. They additionally reflected a small but significant change of the fragment angular distributions for different initial ro-vibrational ionic excitations. The size of the anisotropy is comparable to the one deduced for rotationally averaged HD^+ and likewise suggests the interference of s and d partial-waves instead of a pure d-wave coupling of the incident electron.

The results revealed a much more detailed dynamical picture of the interplay between electrons and molecular ions in low-energy DR processes than previously obtained. They open up a new observational window on the low-energy ro-vibrational Feshbach resonances and for future theoretical approaches provide a wide range of additional aspects to be considered on the way towards a complete picture of molecular fragmentation by cold electrons.

6.2 Future goals

Having demonstrated that the combination of high resolution fragment imaging with the twin-merged-beam storage ring technique presents a versatile experimental tool in molecular fragmentation studies, the doorway to elucidate neutral product kinematics also of other molecular systems at low impact energies has been opened up. Several improvements can still be considered on the experimental side to promote this method to become a more frequently applied observational window in DR research.

For instance, the frame-taking rate of the camera system is currently the main factor limiting the collection of high statistics within a short measurement time. Dynamical aspects of the fragmentation process can thus currently be scanned over only a small energy range, restricted by the number of measurement points that can be realized under practical aspects within an experimental period. However, state-of-the-art 2D fragment imaging systems with ~10 - 20 times higher acquisition rates have become available meanwhile and provide new possibilities.

The present detector has the advantage of recording also 3D fragmentation patterns. Improvements of the system, in particular by lowering the noise level and understanding the limiting detector properties discussed as "rate effects" on page 47, are currently planned so that future experiments can benefit from better time resolution in the recorded 3D

information.

In the electron target the effective overlap length of the electrons can be shortened through changes of the electron beam guiding scheme so that not only the uncertainty in the analysis procedure reduces, but also the sensitivity on the kinetic energy release increases. These improvements will make it possible to revisit the fragmentation dynamics in low-energy DR of the hydrogen molecule. For instance, employing a denser measurement grid for the DR of state-selected H_2^+ ions can elucidate the energy and ionic-state dependent role of the participating electronic symmetries, which in the current experiments could be sampled only at distinct electron energies. Furthermore, utilizing a buffer gas cooled radio-frequency multipole ion trap [124] for the HD^+ production can, at least within a short storage-time window, provide ions dominantly in the ro-vibrational ground state which were not yet available in the present experiments.

Gaining a good control over the collision processes of these "simplest" molecular ions will certainly encourage the extension of the studies towards heavier (multi-electron) as well as polyatomic molecules. 3D fragment imaging will then be an indispensable tool in order to uniquely determine relative fragment positions for the study of the fragmentation dynamics. In fact, the present detection system has been developed to measure impact time differences and positions for an in principle unlimited number of fragments, thus well suited for the study of polyatomic molecules. Supplementary information can even be expected from a presently installed new detection system at the BAMBI beamline, an energy sensitive multi-stripe detector (EMU), which will yield event-by-event access to the individual fragment masses and thus the final branching channels in DR reactions.

Together with new ion sources and acceleration schemes currently investigated at the facility of the Max-Planck-Institut für Kernphysik in Heidelberg, the path towards the study of complex molecules such as H_3O^+, HCO^+, $HCNH^+$ or NH_4^+ has been paved and promises to provide new insights to their fragmentation processes.

Appendix

A Transverse distance distribution

Assuming the dissociation of a DR event at a distinct distance s from the detector, the probability distribution $F_s(D)$ for the expected transverse distances D is described by (Eq.(3.7) [79])

$$F_s(D) = \frac{D}{\delta_n^2 s \sqrt{s^2 - (D/\delta_n)}} W(\theta) \tag{1}$$

with the maximum laboratory emission angle δ_n for a defined initial-to-final-state channel n (Eq.(3.6)) and the angular distribution $W(\theta)$ expressed through a sum of Legendre polynomials $P_l(\cos\theta)$ with coefficients a_l of order l:

$$W(\theta) = \sum_l a_l P_l(\cos\theta) . \tag{2}$$

The finite overlap of the electron beam in the electron target requires to integrate $F_s(D)$ over the interaction length L, assuming an equal dissociation probability between the minimum s_1 and maximum s_2 flight distance ($L = s_2 - s_1$). This is done for each polynomial $P_l(\cos\theta)$ (here only even orders) and initial-to-final-state channel $n = (v^+, J^+, n_A, n_B)$ and yields the total model function of the transverse distance distribution applied in the fitting procedures:

$$F(D) = \sum_{v^+, J^+, n_A, n_B} \sum_l b_{v^+, J^+, n_A, n_B} \, a_{l; v^+, J^+, n_A, n_B} \, F_{l; v^+, J^+, n_A, n_B}(D) \tag{3}$$

(equivalent to Eq.(3.10)) with b_{v^+, J^+, n_A, n_B} describing the relative contribution of the DR channel (v^+, J^+, n_A, n_B). In this appendix the computed terms $F_{l;n}(D)$ used in the analysis for the 0th, 2nd and 4th order Legendre polynomial are given (Γ_i ($i = 1, 2$) - defined as $\sqrt{s_i^2 - (D/\delta_n)^2}$):

Expected distribution $F_{0,n}$ for isotropic angular dependence ($l = 0$; $P_0(\cos\theta) = 1$):

$$F_{0,n}(D) = \begin{cases} \dfrac{1}{\delta_n L} \left(\arccos\dfrac{D}{\delta_n\, s_2} - \arccos\dfrac{D}{\delta_n\, s_1} \right) \\[2mm] \qquad\quad \text{for } 0 \le D \le \delta_n\, s_1 \\[4mm] \dfrac{1}{\delta_n L} \arccos\dfrac{D}{\delta_n\, s_2} \\[2mm] \qquad\quad \text{for } \delta_n\, s_1 \le D \le \delta_n\, s_2 \\[4mm] 0 \qquad\qquad \text{otherwise} \end{cases} \tag{4}$$

Appendix

Expected distribution $F_{2,n}$ for 2nd order Legendre polynomial
$(l = 2;\ P_2(\cos^2\theta) = \frac{1}{2}\cdot(3\cos^2\theta - 1))$:

$$
F_{2,n}(D) = \begin{cases} \dfrac{3\,D}{4\,L\,\delta_n^2}\left(\dfrac{\Gamma_1}{s_1^2} - \dfrac{\Gamma_2}{s_2^2}\right) + \dfrac{1}{4\,L\,\delta_n}\left(\arccos\dfrac{D}{\delta_n\,s_2} - \arccos\dfrac{D}{\delta_n\,s_1}\right) \\[2mm] \qquad\qquad \text{for } 0\ \leq\ D\ \leq \delta_n\,s_1 \\[4mm] -\dfrac{3\,D\,\Gamma_2}{4\,L\,\delta_n^2\,s_2^2} + \dfrac{1}{4\,L\,\delta_n}\ \arccos\dfrac{D}{\delta_n\,s_2} \\[2mm] \qquad\qquad \text{for } \delta_n\,s_1\ \leq\ D\ \leq \delta_n\,s_2 \\[4mm] 0 \qquad\qquad \text{otherwise} \end{cases}
\tag{5}
$$

Expected distribution $F_{4,n}$ for 4th order Legendre polynomial
$(l = 4;\ P_4(\cos\theta) = \frac{1}{8}\cdot(35\cos^4\theta - 30\cos^2\theta + 3))$:

$$
F_{4,n}(D) = \begin{cases} \dfrac{35\,D}{32\,L\,\delta_n^2}\left(\dfrac{\Gamma_1^3}{s_1^4} - \dfrac{\Gamma_2^3}{s_2^4}\right) + \dfrac{15\,D}{64\,L\,\delta_n^2}\left(\dfrac{\Gamma_2}{s_2^2} - \dfrac{\Gamma_1}{s_1^2}\right) + \dfrac{9}{64\,L\,\delta_n}\left(\arccos\dfrac{D}{\delta_n\,s_2} - \arccos\dfrac{D}{\delta_n\,s_1}\right) \\[2mm] \qquad\qquad \text{for } 0\ \leq\ D\ \leq \delta_n\,s_1 \\[4mm] -\dfrac{35\,D\,\Gamma_2^3}{32\,L\,\delta_n^2\,s_2^4} + \dfrac{15\,D\,\Gamma_2}{64\,L\,\delta_n^2\,s_2^2} + \dfrac{9}{64\,L\,\delta_n}\ \arccos\dfrac{D}{\delta_n\,s_2} \\[2mm] \qquad\qquad \text{for } \delta_n\,s_1\ \leq\ D\ \leq \delta_n\,s_2 \\[4mm] 0 \qquad\qquad \text{otherwise} \end{cases}
$$

$$\tag{6}$$

B Electron energy distribution

The convolution of the DR angular dependence over the electron velocity distribution is performed in Sec. 4.3.1 in energy space, that is as a function of the electron energy E and the angle β between the incident electron and the ion beam direction (Fig. 4.13). The transformation of the generally given electron velocity distribution into a dependence on E and β is outlined in the following:

The flattened double Maxwellian electron velocity distribution $f(\vec{v_e}, v_d)$ at a given detuning electron velocity v_d is described by:

$$f(\vec{v_e}, v_d) = \frac{m_e}{2\pi k T_\perp} \left(\frac{m_e}{2\pi k T_\parallel}\right)^{1/2} e^{\left(-\frac{m_e v_\perp^2}{2kT_\perp} - \frac{m_e(v_\parallel - v_d)^2}{2kT_\parallel}\right)} \tag{7}$$

with

$$\vec{v_e} = \left(v_\perp, v_\parallel\right) \tag{8}$$

and longitudinal $T_\parallel$ as well as transversal $T_\perp$ electron temperatures (m_e - electron mass; k - Boltzman constant). In the first step, expression (7) is rephrased into:

$$f(\vec{v_e}, v_d) = \frac{1}{(2\pi)^{3/2}\sigma_\perp^2 \cdot \sigma_\parallel} e^{\left(-\frac{v_\perp^2}{2\sigma_\perp^2} - \frac{(v_\parallel - v_d)^2}{2\sigma_\parallel^2}\right)} \tag{9}$$

with

$$\sigma_i = \sqrt{\frac{k \cdot T_i}{m_e}} \ . \tag{10}$$

Defining

$$v_e \equiv \|\vec{v_e}\| \quad \text{and}$$

$$v_\parallel = v_e \cdot \cos\beta = v_e \cdot x \ ; \ v_\perp = v_e \sqrt{1 - x^2}$$

subsequently yields

$$f(\vec{v_e}, v_d) = A \cdot e^{\left(-\frac{v_e^2 \cdot (1 - x^2)}{2\sigma_\perp^2} - \frac{(x \cdot v_e - v_d)^2}{2\sigma_\parallel^2}\right)} \tag{11}$$

with the parameter

$$A \equiv \frac{1}{(2\pi)^{3/2}\sigma_\perp^2 \cdot \sigma_\parallel} = \frac{m_e^{3/2}}{(2\,\pi)^{3/2}\,k \cdot T_\perp\,\sqrt{kT_\parallel}} \ . \tag{12}$$

Finally, after introducing the parameter ξ which describes the ratio between the longitudinal and transversal electron temperatures

$$\xi = 1 - \frac{T_{\parallel}}{T_{\perp}} = 1 - \frac{\sigma_{\parallel}^2}{\sigma_{\perp}^2} \text{ and } v = \sqrt{\frac{2E}{m_e}} \tag{13}$$

one arrives at the expression for the electron energy distribution used in Eq.(4.10) :

$$\Rightarrow f(E,x) = A \cdot e^{-\frac{E - (E_d/\xi)}{k \cdot T_{\perp}}} \cdot e^{-\frac{(x\,\xi\,\sqrt{E} - \sqrt{E_d})^2}{\xi \cdot k \cdot T_{\parallel}}} . \tag{14}$$

References

[1] H. Sato, *Photodissociation of Simple Molecules in the Gas Phase*, Chem. Rev. **101** (2001), 2687.

[2] H. Hotop, M.-W. Ruf, M. Allan, and I. I. Fabrikant, *Resonance and threshold phenomena in low-energy electron collisions with molecules and clusters*, Adv. At. Mol. Opt. Phys. **49** (2003), 85.

[3] D. R. Bates, *Dissociative Recombination*, Phys. Rev. **78** (1950), 492.

[4] S. L. Guberman, *Mechanism for the Green Glow of the Upper Ionosphere*, Science **278** (1997), 1276.

[5] E. Herbst and W. Klemperer, *The formation and depletion of molecules in dense interstellar clouds*, Astrophys. J. **185** (1973), 505.

[6] J. Woodall, M. Agúndez, A. J. Markwick-Kemper, and T. J. Millar, *The UMIST database for astrochemistry 2006*, Astron. Astrophys. **466** (2007), 1197.

[7] A. Bultel, B. G. Cheron, A. Bourdon, O. Motapon, and I. F. Schneider, *Collisional-radiative model in air for earth re-entry problems*, Phys. Plasmas **13** (2006), 043502.

[8] M. Larsson, *Dissociative recombination with ion storage rings*, Annu. Rev. Phys. Chem. **48** (1997), 151.

[9] L. H. Andersen, P. J. Johnson, D. Kella, H. B. Pedersen, and L. Vejby-Christensen, *Dissociative-recombination and excitation measurements with H_2^+ and HD^+*, Phys. Rev. A **55** (1997), 2799.

[10] Z. Amitay, A. Baer, M. Dahan, L. Knoll, M. Lange, J. Levin, I. F. Schneider, D. Schwalm, A. Suzor-Weiner, Z. Vager, R. Wester, A. Wolf, D. Zajfman, *Dissociative recombination of HD^+ in selected vibrational quantum states*, Science **281** (1998), 75.

[11] S. Krohn, Z. Amitay, A. Baer, D. Zajfman, M. Lange, L. Knoll, J. Levin, D. Schwalm, R. Wester, and A. Wolf, *Electron-induced vibrational deexcitation of H_2^+*, Phys. Rev. A **62** (2000), 032713.

[12] M. Saito, Y. Haruyama, T. Tanabe, I. Katayama, K. Chida, T. Watanabe, Y. Arakaki, I. Nomura, T. Honma, K. Noda, and K. Hosono, *Vibrational cooling of H_2^+ and D_2^+ in a storage ring studied by means of two-dimensional fragment imaging*, Phys. Rev. A **61** (2000), 062707.

[13] A. Al-Khalili, S. Rosén, H. Danared, A. Derkatch, A. Källberg, M. Larsson, A. Le Padellec, A. Neau, J. Semaniak, R. Thomas, M. af Ugglas, L. Vikor, W. Zong, W. van der Zande, X. Urbain, M. Jensen, R. C. Bilodeau, O. Heber, H. B. Pedersen, C. Safvan, L. H. Andersen, M. Lange, J. Levin, G. Gwinner, L. Knoll, M. Scheffel, D. Schwalm, R. Wester, D. Zajfman, A. Wolf, *Absolute high-resolution rate coefficients for dissociative recombination of electrons with HD^+: Comparison of results from three heavy-ion storage rings*, Phys. Rev. A **68** (2003), 042702.

[14] A. Giusti-Suzor, J. N. Bardsley and C. Derkits, *Dissociative recombination in low-energy e-H_2^+ collisions*, Phys. Rev. A **28** (1983), 682.

[15] H. Takagi, *Rotational effects in the dissociative recombination process of H_2^+ + e*, J. Phys. B **26** (1993), 4815.

[16] I. F. Schneider, C. Strömholm, L. Carata, X. Urbain, M. Larsson, A. Suzor-Weiner, *Rotational effects in HD^+ dissociative recombination: theoretical study of resonant mechanisms and comparison with ion storage ring experiments*, J. Phys. B. **30** (1997), 2687.

[17] H. Buhr, *Electron collisions and internal excitation in stored molecular ion beams*, Ph.D. thesis, Ruperto-Carola University of Heidelberg, Germany, 2006.

[18] S. Novotny, H. Rubinstein, H. Buhr, O. Novotný, J. Hoffmann, M. B. Mendes, D. A. Orlov, C. Krantz, M. H. Berg, M. Froese, A. S. Jaroshevich, B. Jordon-Thaden, M. Lange, M. Lestinsky, A. Petrignani, I. F. Schneider, D. Shafir, F. O. Waffeu Tamo, D. Zajfman, D. Schwalm and A. Wolf, *Anisotropy and molecular rotation in resonant low-energy dissociative recombination*, Phys. Rev. Lett. (2008), accepted.

[19] S. Novotny, H. Rubinstein, H. Buhr, O. Novotný, J. Hoffmann, M. B. Mendes, D. A. Orlov, M. H. Berg, A. S. Jaroshevich, B. Jordon-Thaden, C. Krantz, M. Lange, M. Lestinsky, A. Petrignani, I. F. Schneider, D. Shafir, F. O. Waffeu Tamo, D. Zajfman, D. Schwalm and A. Wolf, *Anisotropic fragmentation in low-energy dissociative recombination*, J. Phys.: Conf. Ser., submitted.

[20] M. Born, R. Oppenheimer, *Zur Quantentheorie der Molekeln*, Annalen der Physik **389** (1927), 457.

[21] B. H. Bransden and C. J. Joachain, *Physics of atoms and molecules, 2nd edition*, Prentice Hall, 2003.

[22] G. Herzberg, *Molecular Spectra and Molecular Structure, I. Spectra of Diatomic Molecules*, Van Nostrand Reinhold, New York, 1950.

[23] H. B. Pedersen, S. Altevogt, B. Jordon-Thaden, O. Heber, M. L. Rappaport, D. Schwalm, J. Ullrich, D. Zajfman, R. Treusch, N. Guerassimova, M. Martins, J.-T. Hoeft, M. Wellhöfer, and A. Wolf, *Crossed Beam Photodissociation Imaging of HeH$^+$ with Vacuum Ultraviolet Free-Electron Laser Pulses*, Phys. Rev. Lett. **98** (2007), 223202.

[24] Å. Larson, N. Djurić, W. Zong, C. H. Greene, A. E. Orel, A. Al-Khalili, A. M. Derkatch, A. Le Padellec, A. Neau, S. Rosén, W. Shi, L. Vikor, H. Danared, M. af Ugglas, M. Larsson, and G. H. Dunn, *Resonant ion-pair formation in electron collisions with HD$^+$ and OH$^+$*, Phys. Rev. A **62** (2000), 042707.

[25] J. Hoffmann, *title not yet known*, Ph.D. thesis, Ruperto-Carola University of Heidelberg, Germany, to be published.

[26] D. R. Bates, *Electron Recombination in Helium*, Phys. Rev. **77** (1950), 718.

[27] A. Giusti, *A multichannel quantum defect approach to dissociative recombination*, J. Phys. B **13** (1980), 3867.

[28] J. N. Bardsley, *The theory of dissociative recombination*, J. Phys. B **1** (1968), 365.

[29] L. J. Butler and D. M. Neumarkn, *Photodissociation dynamics*, J. Phys. Chem. **100** (1996), 12801.

[30] S. M. Altevogt, *Fast-beam photodissociation imaging of molecular ions*, Ph.D. thesis, Ruperto-Carola University of Heidelberg, Germany, 2007.

[31] J. Cooper and R. N. Zare, *Angular Distribution of Photoelectrons*, J. Chem. Phys. **48** (1968), 942.

[32] R. N. Zare, *Photoejection dynamics [1]*, Mol. Photochem. **4** (1972), 1.

References

[33] S. Yang and R. Bersohn, *Theory of the angular distribution of molecular photofragments*, J. Chem. Phys. **61** (1974), 4400.

[34] J. N. Bardsley and F. Mandl, *Resonant scattering of electrons by molecules*, Rep. Prog. Phys. **31** (1968), 471.

[35] G. J. Schulz, *Resonances in Electron Impact on Diatomic Molecules*, Rev. Mod. Phys. **45** (1973), 423.

[36] O. Heber, R. Golser, H. Gnaser, D. Berkovits, Y. Toker, M. Eritt, M. L. Rappaport, and D. Zajfman, *Lifetimes of the negative molecular hydrogen ions: H_2^-, D_2^-, and HD^-*, Phys. Rev. A **73** (2006), 060501.

[37] B. Boudaiffa, P. Cloutier, D. Hunting, M. A. Huels, and L. Sanche, *Resonant Formation of DNA Strand Breaks by Low-Energy (3 to 20 eV) Electrons*, Science **287** (2000), no. 5458, 1658.

[38] F. Martin, P. D. Burrow, Z. Cai, P. Cloutier, D. Hunting and L. Sanche, *DNA Strand Breaks Induced by 0–4 eV Electrons: The Role of Shape Resonances*, Phys. Rev. Lett. **93** (2004), 068101.

[39] G. H. Dunn, *Anisotropies in angular distributions of molecular dissociation products*, Phys. Rev. Lett. **8** (1962), 63.

[40] R. N. Zare, *Dissociation of H_2^+ by electron impact: calculated angular distribution*, J. Chem. Phys. **47** (1967), 204.

[41] T. F. O'Malley and H. S. Taylor, *Angular dependence of scattering products in electron-molecule resonant excitation and in dissociative attachment*, Phys. Rev. **176** (1968), 207.

[42] NIST Chemistry WebBook, http://webbook.nist.gov/chemistry/.

[43] C. Jonah, *Effect of rotation and thermal velocity on the anisotropy in photodissociation spectroscopy*, J. Chem. Phys. **55** (1971), 1915.

[44] R. J. Van Brunt, *Breakdown of the dipole-Born approximation for predicting angular distributions of dissociation fragments*, J. Chem. Phys. **60** (1973), 3064.

[45] A. V. Demyanenko, A. B. Potter, V. Dribinski, and H. Reisler, *NO angular distributions in the photodissociation of $(NO)_2$ at 213 nm: deviations from axial recoil*, J. Chem. Phys. **117** (2002), 2568.

[46] E. Wrede, E. R. Wouters, M. Beckert, R. N. Dixon, Michael and N. R. Ashfold, *Quasiclassical and quantum mechanical modeling of the breakdown of the axial recoil approximation observed in the near threshold photolysis of IBr and Br_2*, J. Chem. Phys. **116** (2002), 6064.

[47] H. Kim, K. S. Dooley, S. W. North, G. E. Hall, and P. L. Houston, *Anisotropy of photofragment recoil as a function of dissociation lifetime, excitation frequency, rotational level, and rotational constant*, J. Chem. Phys. **125** (2006), 133316.

[48] T. F. O'Malley, *Theory of Dissociative Attachment*, Phys. Rev. **150** (1966), 14.

[49] M. Tronc, C. Schermann, R. I. Hall, and F. Fiquet-Fayard, *Differential cross sections and angular distributions of H^- from dissociative electron attachment to H_2 between 3.75 eV and 13 eV*, J. Phys. B **10** (1977), 305.

[50] S. Trajmar and R. I. Hall, *Dissociative electron attachment in H_2O and D_2O: energy and angular distribution of H^- and D^- fragments*, J. Phys. B **7** (1974), L458.

[51] R. Azria, Y. L. Coat, G. Lefevre, and D. Simon, *Dissociative electron attachment on H_2S: energy and angular distributions of H^- ions*, J. Phys. B **12** (1979), 679.

[52] D. J. Haxton, C. W. McCurdy, and T. N. Rescigno, *Angular dependence of dissociative electron attachment to polyatomic molecules: Application to the $^2B_1$ metastable state of the H_2O and H_2S anions*, Phys. Rev. A **73** (2006), 062724.

[53] V. S. Prabhudesai, D. Nandi, and E. Krishnakumar, *On the presence of the $^4\Sigma_u^-$; resonance in dissociative electron attachment to O_2*, J. Phys. B **39** (2006), L277.

[54] R. J. Van Brunt and L. J. Kieffer, *Angular Distribution of O^- from Dissociative Electron Attachment to O_2*, Phys. Rev. A **2** (1970), 1899.

[55] D. Zajfman, Z. Amitay, C. Broude, P. Forck, B. Seidel, M. Grieser, D. Habs, D. Schwalm and A. Wolf, *Measurement of Branching Ratios for the Dissociative Recombination of Cold HD^+ using Fragment Imaging*, Phys. Rev. Lett. **75** (1995), 814.

[56] Z. Amitay, D. Zajfman, P. Forck, U. Hechtfischer, B. Seidel, M. Grieser, D. Habs, R. Repnow, D. Schwalm and A. Wolf, *Dissociative recombination of CH^+: Cross section and final states*, Phys. Rev. A **54** (1996), 4032.

References

[57] J. Semaniak, S. Rosén, G. Sundström, C. Strömholm, S. Datz, H. Danared, M. af Ugglas, M. Larsson, W. J. van der Zande, Z. Amitay, U. Hechtfischer, M. Grieser, R. Repnow, M. Schmidt, D. Schwalm, R. Wester, A. Wolf, and D. Zajfman , *Product-state distributions in dissociative recombination of $^3HeD^+$ and $^4HeH^+$*, Phys. Rev. A **54** (1996), R4617.

[58] F. Hellberg, S. Rosén, R. Thomas, A. Neau, M. Larsson, A. Petrignani, and W. J. van der Zande, *Dissociative recombination of NO^+: Dynamics of the $X^1\Sigma^+$ and a $^3\Sigma^+$ electronic states*, J. Chem. Phys. **118** (2003), 6250.

[59] S. L. Guberman, *Product angular distributions in dissociative recombination*, J. Chem. Phys. **120** (2004), 9509.

[60] _____, *Dissociative recombination angular distributions*, J. Phys.: Conf. Ser. **4** (2005), 58.

[61] A. Messiah, *Quantum Mechanics Volume II*, North-Holland Publishing Company, 1970, p. 426.

[62] A. Petrignani, F. Hellberg, R. D. Thomas, M. Larsson, P. C. Cosby, W. J. van der Zande, *Electron energy-dependent product state distributions in the dissociative recombination of O_2^+*, J. Chem. Phys. **122** (2005), 234311.

[63] Z. Amitay, D. Zajfman and P. Forck, *Rotational and vibrational lifetime of isotropically asymmetrized homonuclear diatomic molecular ions*, Phys. Rev. A **50** (1994), 2304.

[64] M. I. Chibisov, J. B. A. Mitchell, P. J. T. Van der Donk, F. B. Yousif, and T. J. Morgan, *Dissociative recombination of vibrationally excited H_2^+ ions: High-Rydberg-state formation*, Phys. Rev. A **56** (1997), 443.

[65] G. G. Balint-Kurti, R. E. Moss, I. A. Sadler, and M. Shapiro, *Calculations of vibration-rotation energy levels of HD^+*, Phys. Rev. A **41** (1990), 4913.

[66] S. L. Guberman, *The doubly excited autoionizing states of H_2*, J. Chem. Phys. **78** (1983), 1404.

[67] P. Forck, M. Grieser, D. Habs, A. Lampert, R. Repnow, D. Schwalm, A. Wolf, and D. Zajfman, *Dissociative recombination of cold HD^+ at the Test Storage Ring*, Phys. Rev. Lett. **70** (1993), 426.

[68] S. Krohn, *Inelastic collisions and recombination between electrons and molecular ions*, Ph.D. thesis, Ruperto-Carola University of Heidelberg, Germany, 2001.

[69] S. L. Guberman and A. Giusti-Suzor, *The generation of $O(^1S)$ from the dissociative recombination of O_2^+*, J. Chem. Phys. **95** (1991), 2602.

[70] L. Carata, I. F. Schneider, and A. Suzor-Weiner, *The role of Rydberg states in dissociative recombination, as revealed by storage ring experiments*, Phil. Trans. R. Soc. Lond. A **355** (1997), 1677.

[71] J. Tennyson and C. J. Noble, *Low-energy electron-H_2^+ collisions: variation of resonance parameters with internuclear separation*, J. Phys. B **18** (1985), 155.

[72] I. F. Schneider, O. Dulieu and A. Giusti-Suzor, *The role of Rydberg states in H_2^+ dissociative recombination with slow electrons*, J. Phys. B. **24** (1991), L289.

[73] D. Zajfman, S. Krohn, M. Lange, H. Kreckel, L. Lammich, D. Strasser, D. Schwalm, X. Urbain, A. Wolf, *Physics with molecular ions in storage rings*, Nucl. Instr. and Meth. in Phys. Res. B **205** (2003), 360.

[74] D. Zajfman, D. Schwalm and A. Wolf, *Multiparticle imaging of fast molecular ion beams*, Many-Particle Quantum Dynamics in Atomic and Molecular Fragmentation (J. Ullrich, V.P. Shevelko, ed.), Springer, 2003, p. 59.

[75] M.N.R. Ashfold, N. H. Nahler, A. J. Orr-Ewing, O. P. J. Vieuxmaire, R. L. Toomes, T. N. Kitsopoulos, I. A. Garcia, D. A. Chestakov, S. Wu and D. H. Parker, *Imaging the dynamics of gas phase reactions*, Phys. Chem. Chem. Phys., **8** (2006), 26.

[76] A. Wolf, D. Schwalm and D. Zajfman, *Fragment-imaging studies of dissociative recombination*, Many-Particle Quantum Dynamics in Atomic and Molecular Fragmentation (J. Ullrich, V.P. Shevelko, ed.), Springer, 2003, p. 485.

[77] J. Ullrich, R. Moshammer, A. Dorn, R. Dorner, L. Ph. H. Schmidt, and H. Schmidt-Bocking, *Recoil-ion and electron momentum spectroscopy: reaction-microscopes*, Rep. Prog. Phys. **66** (2003), 1463.

[78] L. Lammich, *Fragmentation Studies with Stored Beams of Small Polyatomic Ions*, Ph.D. thesis, Ruperto-Carola University of Heidelberg, Germany, 2004.

[79] B. Seidel, *Analyse von Fragmentverteilungen bei der dissoziativen Rekombination von HD^+ - und CH^+ - Molekülionen*, Diplomarbeit, Ruperto-Carola Universität Heidelberg, 1996.

References

[80] Z. Amitay, A.Baer, M. Dahan, J. Levin, Z. Vager, D. Zajfman, L. Knoll, M. Lange, D. Schwalm, R. Wester, A. Wolf, I. F. Schneider and A. Suzor-Weiner, *Dissociative recombination of vibrationally excited HD^+: State-selective experimental investigation*, Phys. Rev. A **60** (1999), 3769.

[81] D. Habs, W. Baumann, J. Berger, P. Blatt, A. Faulstich, P. Krause, G. Kilgus, R. Neumann, W. Petrich, R. Stockstad, D. Schwalm, E. Szmola, K. Welti, A. Wolf, S. Zwickler, E. Jaeschke, D. Krämer, G. Bisoffi, M. Blum, A. Friedrich, C. Geyer, M. Grieser, H. W. Heyng, B. Holzer, R. Ihde, M. Jung, K. Matl, W. Ott, B. Povh, R. Repnow, M. Steck, E. Steffens, D. Dutta, T. Kühl, D. Marx, S. Schröder, M. Gerhard, R. Grieser, G. Huber, R. Klein, M. Krieg, N. Schmidt, R. Schuch, J. F. Babb, L. Spruch, W. Arnold and A. Noda, *First experiments with the Heideleberg test storage ring TSR*, Nucl. Instrum. Methods B **43** (1989), 390.

[82] M. Lestinsky, E. Lindroth, D. A. Orlov, E. W. Schmidt, S. Schippers, S. Böhm, C. Brandau, F. Sprenger, A. S. Terekhov, A. Müller, and A. Wolf, *Screened radiative corrections from hyperfine-split dielectronic resonances in lithiumlike scandium*, Phys. Rev. Lett. **100** (2008), 033001.

[83] I. Nevo, S. Novotny, H. Buhr, V. Andrianarijaona, S. Altevogt, O. Heber, J. Hoffmann, H. Kreckel, L. Lammich, M. Lestinsky, H. B. Pedersen, D. Schwalm, A. Wolf and D. Zajfman, *Three-body kinematical correlation in the dissociative recombination of CH_2^+ by three-dimensional imaging*, Phys. Rev. A **76** (2007), 022713.

[84] O. Novotný, O. Motapon, M. H. Berg, D. Bing, H. Buhr, H. Fadil, J. Hoffmann, A. S. Jaroshevich, B. Jordon-Thaden, C. Krantz, M. Lange, M. Lestinsky, M. B. Mendes, S. Novotny, A. Petrignani, D. A. Orlov, I. F. Schneider, A. E. Orel and A. Wolf, *Dissociative recombination of CF^+: experiment and theory*, J. Phys.: Conf. Ser., submitted.

[85] M. Grieser, H. Deitinghoff, D. Habs, R. von Hahn, E. Jaeschke, C.-M. Kleffner, V. Kössler, S. Papureanu, R. Repnow, M.-H. Rhee, D. Schwalm and A. Schempp, *Upgrading of the Heidelberg accelerator facility with a new high current injector*, Nucl. Instrum. Methods A **328** (1993), 160.

[86] M. Schnell, *Designstudie eines frequenzvariablen 4-Rod-Beschleunigers als Molekülioneninjektor für den Heidelberger Speicherring*, Diplomarbeit, Ruperto-Carola Universität Heidelberg, 2004.

[87] R. von Hahn, M. Grieser, D. Habs, E. Jaeschke, C.-M. Kleffner, J. Liebermann, S. Papureanu, R. Repnow, D. Schwalm and M. Stampfer, *Development of seven-gap resonators for the Heidelberg high current injector*, Nucl. Instrum. Methods A **328** (1993), 270.

[88] N. de Ruette, *Sélectivité rovibrationnelle de l'ionisation de H_2 en champ laser intense*, Ph.D. thesis, Université Catholique de Louvain, Belgium, 2007.

[89] H. Poth, *Electron cooling: theory, experiment, application*, Phys. Rep. **196** (1990), 135.

[90] M. Beutelspacher, M. Grieser, D. Schwalm, and A. Wolf, *Longitudinal and transverse electron cooling experiments at the Heidelberg heavy ion storage ring TSR*, Nucl. Instr. Meth. A **441** (2000), 110.

[91] H. Danared, G. Andler, L. Bagge, C. J. Herrlander, J. Hilke, J. Jeansson, A. Källberg, A. Nilsson, A. Paál, K. G. Rensfelt, U. Rosengård, J. Starker, and M. af Ugglas, *Electron Cooling with an Ultracold Electron Beam*, Phys. Rev. Lett. **72** (1994), 3775.

[92] F. Sprenger, *Production of cold electron beams for collision experiments with stored ions*, Ph.D. thesis, Ruperto-Carola University of Heidelberg, Germany, 2003.

[93] F. Sprenger, M. Lestinsky, D.A. Orlov, D. Schwalm, and A. Wolf, *The high resolution electron-ion collision facility at TSR*, Nucl. Inst. Meth. A **532** (2004), 298.

[94] M. Lestinsky, *High-resolution electron collision spectroscopy with multicharged ions in merged beams*, Ph.D. thesis, Ruperto-Carola University of Heidelberg, Germany, 2007.

[95] U. Weigel, *Cold intense electron beams from Gallium Arsenide photocathodes*, Ph.D. thesis, Ruperto-Carola University of Heidelberg, Germany, 2003.

[96] D. A. Orlov, U. Weigel, D. Schwalm, A.S. Terekhov, and A. Wolf, *Cold intense electron beams from LN_2-cooled GaAs-Photocathodes*, Nucl. Instrum. Methods A **532** (2004), 418.

[97] D. A. Orlov, F. Sprenger, M. Lestinsky, U. Weigel, A. S. Terekhov, D. Schwalm and A. Wolf, *Photocathodes as electron sources for high resolution merged beam experiments*, J. Phys.: Conf. Ser. **4** (2005), 290.

References

[98] S. Novotny, *Fast-beam molecular fragmentation imaging using a high-speed gated camera system*, Diplomarbeit, Ruperto-Carola University of Heidelberg, Germany, 2004.

[99] M. B. Mendes, *Hochauflösende dreidimensionale Fragmentabbildung bei Speicherringexperimenten mit Molekülionen*, Diplomarbeit, Ruperto-Carola Universität Heidelberg, 2007.

[100] D. Strasser, X. Urbain, H. B. Pedersen, N. Altstein, O.Heber, R. Wester, K. G. Bhushan and D. Zajfman, *An innovative approach to multiparticle three-dimensional imaging*, Rev. Sci. Inst. **71** (2000), 3092.

[101] J. L. Wiza, *Microchannel plate detectors*, Nucl. Instr. Meth. **162** (1979), 587.

[102] C. L. Melcher, J. S. Schweitzer, C. A. Peterson, R. A. Manente, and H. Suzuki, *Crystal Growth and Scintillations Properties of the rare Earth Oxyorthosilicates*, Proc. Int. Conf. on Inorganic Scintillators and their Applications, SCINT95, Delf University Press, 1996, p. 309.

[103] LaVision GmbH, Göttingen, Germany, *http://www.lavision.de/*.

[104] ROOT, http://root.cern.ch.

[105] W. H. Press, S. A. Teukolsky, W. T. Veterrling, B. P. Flannery, *Numerical Recipies in FORTRAN*, Cambridge university press, 1992.

[106] H. Rubinstein, *Measurement of angular distributions in dissociative recombination of HD^+ molecular ions*, Master's thesis, Weizmann Institute of Science, Rehovot, Israel, 2007.

[107] A. Lampert, A. Wolf, D. Habs, J. Kenntner, G. Kilgus, D. Schwalm, M. S. Pindzola, and N. R. Badnell, *High-resolution measurement of the dielectronic recombination of fluorinelike selenium ions*, Phys. Rev. A **53** (1996), 1413.

[108] G. Hunter, A.W. Yau, and H.O. Pritchard, *Rotation-vibration level energies of the hydrogen and deuterium molecule-ions*, Atomic Data and Nuclear Data Tables **14** (1974), 11.

[109] D. Shafir, et al., *to be published*.

[110] T. Tanabe, H. Takagi, I. Katayama, K. Chida, T. Watanabe, Y. Arakaki, Y. Haruyama, M. Saito, I. Nomura, T. Honma, K. Noda, and K. Hosono, *Evidence of Superelastic Electron Collisions from H_2^+ Studied by Dissociative Recombination Using an Ultracold Electron Beam from a Cooler Ring*, Phys. Rev. Lett. **83** (1999), 2163.

[111] H. Buhr, H. B. Pedersen, S. Altevogt, V. M. Andrianarijaona, H. Kreckel, L. Lammich, S. Novotny, D. Strasser, J. Hoffmann, M. Lange, M. Lestinsky, M. B. Mendes, M. Motsch, O. Novotný, D. Schwalm, X. Urbain, D. Zajfman, and A. Wolf, *Inelastic electron collisions of the isotopically symmetric helium dimer ion $^4He_2^+$ in a storage ring*, Phys. Rev. A **77** (2008), 032719.

[112] V. Ngassam, O. Motapon, A. Florescu, L. Pichl, I. F. Schneider, and A. Suzor-Weiner, *Vibrational relaxation and dissociative recombination of H_2^+ induced by slow electrons*, Phys. Rev. A **68** (2003), 032704.

[113] O. Novotný *et al.*, *Storage ring experiments on dissociative recombination of CF^+*, to be published.

[114] F. O. Waffeu Tamo, *Recombinaison dissociative dans les plasmas d'intérêt atmosphérique et énergétique*, Ph.D. thesis, University of Le Havre, France, not yet published.

[115] A. Messiah, *Quantum Mechanics Volume II*, North-Holland Publishing Company, 1970, pp. 1074–1075.

[116] G. V. Golubkov, M. G. Golubkov, and G. K. Ivanov, *Rotation in the dissociative-recombination reaction of electrons and ion of molecular hydrogen*, Engl. transl.: Sov. Phys.-JETP **81** (1995), 56.

[117] T. Tanabe, I. Katayama, H. Kamegaya, K. Chida, Y. Arakaki, T. Watanabe, M. Yoshizawa, M. Saito, Y. Haruyama, K. Hosono, K. Hatanaka, T. Honma, K. Noda, S. Ohtani, and H. Takagi, *Dissociative recombination of HD^+ with an ultracold electron beam in a cooler ring*, Phys. Rev. Lett. **75** (1995), 1066.

[118] I. F. Schneider, 2008, private communication.

[119] D. Teillet-Billy and J. P. Gauyacq, *Angular dependence of dissociative attachment to polar molecules*, J. Phys. B **17** (1984), 3329.

References

[120] B. Valcu, I. F. Schneider, M. Raoult, C. Strömholm, M. Larsson and A. Suzor-Weiner, *Rotational effects in low energy dissociative recombination of diatomic ions* , Eur. Phys. J. D **1** (1998), 71.

[121] R. Wester, F. Albrecht, M. Grieser, L. Knoll, R. Repnow, D. Schwalm, A. Wolf, A. Baer, J. Levin, Z. Vager, and D. Zajfman,, *Coulomb explosion imaging at the heavy ion storage ring TSR*, Nucl. Instr. Meth. A **413** (1998), 379.

[122] B. J. McCall, A. J. Huneycutt, R. J. Saykally, N. Djuric, G. H. Dunn, J. Semaniak, O. Novotny, A. Al-Khalili, A. Ehlerding, F. Hellberg, S. Kalhori, A. Neau, R. D. Thomas, A. Paal, F. Österdahl, and M. Larsson, *Dissociative recombination of rotationally cold H_3^+*, Phys. Rev. A **70** (2004), 052716.

[123] V. Zhaunerchyk, A. Al-Khalili, R. D. Thomas, W. D. Geppert, V. Bednarska, A. Petrignani, A. Ehlerding, M. Hamberg, M. Larsson, S. Rosen, and W. J. van der Zande, *Rotational State Effects in the Dissociative Recombination of H_2^+*, Phys. Rev. Lett. **99** (2007), 013201.

[124] H. Kreckel, M. Motsch, J. Mikosch, J. Glosik, R. Plasil, S. Altevogt, V. Andrianarijaona, H. Buhr, J. Hoffmann, L. Lammich, M. Lestinsky, I. Nevo, S. Novotny, D. A. Orlov, H. B. Pedersen, F. Sprenger, A. S. Terekhov, J. Toker, R. Wester, D. Gerlich, D. Schwalm, A. Wolf, and D. Zajfman, *High-Resolution Dissociative Recombination of Cold H_3^+ and First Evidence for Nuclear Spin Effects*, Phys. Rev. Lett. **95** (2005), 263201.

[125] F. von Busch and G. H. Dunn, *Photodissociation of H_2^+ and D_2^+: Experiment*, Phys. Rev. A **5** (1972), 1726.

[126] H. Hus, F. Yousif, C. Noren, A. Sen, and J. B. A. Mitchell , *Dissociative recombination of electrons with H_2^+ in low vibrational states*, Phys. Rev. Lett. **60** (1988), 1006.

[127] P. M. Dehmer S. T. Pratt and J. L. Dehmer, *Photoionization of excited molecular states. H_2 $C\,^1\Pi_u$*, Chem. Phys. Lett. **105** (1984), 28.

[128] M. A. O'Halloran, S. T. Pratt, P. M. Dehmer, and J. L. Dehmer, *Photoionization dynamics of H_2 $C\,^1\Pi_u$: Vibrational and rotational branching ratios*, J. Chem. Phys. **87** (1987), 3288.

[129] S. N. Dixit and V. McKoy, *Ionic rotational selection rules for (n + 1) resonant enhanced multiphoton ionization*, Chem. Phys. Lett. **128** (1986), 49.

[130] S. T. Pratt, P. M. Dehmer, and J. L. Dehmer, *Photoionization dynamics of excited molecular states. Photoelectron angular distributions and rotational and vibrational branching ratios for H_2 $C\,^1\Pi_u$, $v = 0 - 4$*, J. Chem. Phys. **85** (1986), 3379.

[131] X. Urbain, 2008, private communication.

Danksagung

Die letzten beiden Seiten gebühren all denjenigen, die mich in den vergangenen Jahren bei der Entstehung dieser Doktorarbeit auf die vielfältigste Art und Weise unterstützt haben und somit einen großen Anteil daran tragen, daß ich die vorliegenden Ergebnisse auf den vielen Seiten zuvor präsentieren konnte.

Zuallererst möchte ich mich an dieser Stelle ganz herzlich bei Andreas Wolf für seinen großen Einsatz bei der Betreuung meiner Arbeit in den vergangenen Jahren bedanken. Sei es durch neue Ideen und Anregungung in hilfreichen Diskussionen, sein immer offenes Ohr für Fragen oder das Lösen so manch ausweglos erscheinender Situation bei Strahlzeiten, er war immer mit großem Engagement zur Stelle.

Ein herzlicher Dank geht auch an Dirk Schwalm und Daniel Zajfman für die Möglichkeit, zum einen in ihrer Arbeitsgruppe forschen zu können, aber auch insbesondere für ihre vielen Ratschläge und kritischen Diskussionen aus denen immer wieder interessante Ideen hervorgingen. Vielen Dank auch an Herrn Prof. Thomas Stöhlker für die Bereitschaft, das Zweitgutachten dieser Arbeit zu übernehmen.

Diese Zeilen geben mir auch die Möglichkeit mich bei allen ehemaligen und noch aktiven Mitgliedern der Molekülphysik Gruppe für ihren Einsatz vor, während und zwischen den vielen Strahlzeiten zu bedanken. Besonders sei hier die "BAMBI-Crew" um Henrik Buhr, Mario Mendes und Oldrich Novotný erwähnt, die in der Vorbereitung und der Durchführung von Experimenten mit den Detektoren nicht wegzudenken war. Am Target wäre so manch ein Elektronenstrahl verloren gegangen hätten nicht Jens Hoffmann, Claude Krantz, Michael Lestinsky und Dima Orlov rund um die Uhr unermüdlichen Einsatz gezeigt. Ein Dank richtet sich aber auch an alle anderen der Gruppe für viele Diskussionen, die neuen Kochvorschläge beim "Friday-Lunchclub", die Laufgesellschaft bis auf den Königsstuhl und nicht zuletzt für ihre Bereitschaft lange Tag- und Nachtschichten zu übernehmen: Simon Altevogt, Dennis Bing, Max Berg, Mike Froese, Brandon Jordan-Thaden, Holger Kreckel, Michael Lange, Annemieke Petrignani, Sascha Reinhardt, Andrey Shornikov, Tobias Sorg und Jule Stützel.

Sehr geschätzt habe ich auch in dieser Zeit die Zusammenarbeit mit unterschiedlichen Gruppen aus Israel, Frankreich, USA und Belgien. Vom Weizmann Institut aus Israel waren oftmals Iftach Nevo, Hillel Rubinstein und Dror Shafir bei den Experimenten und besonders bei deren Auswertung mit dabei und brachten so neue Ideen mit an den TSR. Ein "merci beaucoup" und ein "thank you" gehen auch an Ioan Schneider und Francois-Olivier Waffeu Tamo aus Le Havre sowie an Chris Greene aus Boulder für die, finde ich,

wirklich gute Zusammenarbeit zwischen Theorie und Experiment und den vielen damit verbundenen fruchtbaren Diskussionen. Die Experimente, welche ich im fünften Kapitel beschrieben habe, wären ohne die Vorarbeit und den Einsatz von Nathalie de Ruette, Xavier Urbain und Xavier Gillon aus Louvain-La-Neuve nicht möglich gewesen und gaben mir doch auf diese Weise viele neue Erfahrungen, merci!

Bei Manfred Grieser und Kurt Horn möchte ich mich ganz herzlich für ihren unermüdlichen Einsatz bedanken, den sie beim Einstellen des TSR zeigten, um den Molekülstrahl immer wieder schön auf die Mitte des Detektors zu lenken. Dazu gehören auch alle anderen, die dafür sorgen, daß durch ihren fachkundigen Einsatz Strahlzeiten rund um die Uhr möglich sind und dabei vor keinem Problem zu welcher Tages- oder Nachtzeit auch immer zurückschrecken, insbesondere seien hier Roland Repnow, Robert von Hahn und Manfred König aber auch die nicht namentlich genannten Operateure und Techniker erwähnt die zu dieser gut funktionierenden und eingespielten Mannschaft dazugehören.

Dank auch an die Werkstätten unter Leitung von Herrn Hahn und Herrn Mallinger, deren Mitarbeiter stets sehr hilfsbereit waren und selbst bei Sonderwünschen gewissenhaft und präzise die Arbeiten durchgeführt haben. Besonders sei hier auch Herr Hallatschek erwähnt, der immer für gutes Vakuum in BAMBI gesorgt hat. Danke auch an Oliver Koschorreck für seine Hilfe bei Problemen mit der Elektronik. Ein herzlicher Dank geht auch an Helga Krieger für ihre Unterstützung bei den verschiedensten organisatorischen Aufgaben die einem in den Jahren begegnen, sowie an Gernot Vogt für die Beschaffung so manch ausgefallener Publikation.

Zu guter Letzt gilt mein größter Dank meinen Eltern, meiner Schwester und meiner Freundin Sara. Sie waren für mich immer da, gaben mir den nötigen Rückhalt und waren für mich unersetzlich in den vergangenen Jahren. Besonders geschätzt habe ich auch die Hilfe meines Vaters auf dem Weg zum Erstellen dieser Arbeit, nicht zuletzt für das kritische Lesen in den Wochen vor der Abgabe.

Sara, paljon kiitoksia kaikkille! Minä en tiedä mikä minä teen ilman sinua. Sinä olit aina täällä vaikealla aikalla ja kun tarvitsen sinua. Sinä olen antanut minulle voimaa ja apua, ja en ole valittanut minulle kun minä olin koko yö töissä. Sinä olet minun kultapalani!

Vielen Dank an alle!